UNIVERSITÁ DEGLI STUDI DI UDINE

Corso di dottorato di ricerca in Scienze dell'Ingegneria Energetica e Ambientale.

XXX ciclo

Numerical simulation of thin liquid films over a solid non-wettable substrate assuming lubrication approximation.

Dottorando:
Nicola Suzzi

Supervisore:
Giulio Croce

Anno 2018

Abstract

When a continuous film flows over a non-wettable surface, it may break up with the consequent formation of a dry-patch. The actual shape of the resulting water layer is of great interest in several engineering applications, such as in-flight icing simulations, finned dehumidifier behavior modeling, coating process and chemical absorption/distillation through structured packing. A 2D numerical solver for the prediction of film flow is presented. The lubrication approximation is assumed, allowing for the description of liquid film flowing down an inclined plate, driven by both gravity and shear. The effects of contact line and surface wettability are introduced combining the precursor film model and the disjoining pressure terms. The capillary pressure, which is usually modeled through the small slope approximation, is here defined imposing the membranal equilibrium of the gas-liquid free-surface, in order to investigate higher values of the imposed equilibrium contact angle between liquid and solid substrate. The in-house solver is first validated with both experimental and numerical results, available in literature. Numerical simulations are then performed with the aim of studying the behavior of liquids in absorption/distillation process through structured packing. The lubrication theory is finally extended to the most general case of a 3D curved substrate, allowing to investigate problems involving complex geometries and configurations. Thus, a liquid film flowing down a packing layer, which is a wrinkled surface composing the packed column used in absorption process, is simulated. Such a problem has been investigated in literature by means of a fully 3D approach only, but the huge computational costs do not allow to investigate several configurations, resulting in a lack of knowledge of the hydrodynamics driving the liquid flowing through the packing layers.
The full modeling of the capillary pressure and the extension to general curved substrates clearly put a new effort to the well known lubrication theory and allow to simulate phenomena, that were not covered by such a theory.

Contents

1 Introduction **1**

2 Flowing films **5**
2.1 Phenomenological models 5
2.2 Lubrication approximation 10
2.2.1 Capillary pressure 10
2.2.2 Disjoining pressure 11
2.3 Governing equation 14
2.4 Analytical solutions 17
2.5 Numerical approach 22
2.6 Modelling of inertial effect 26
2.7 Diffuse interface theory of thin films 28
2.7.1 Chemical potential of a thin film 30
2.7.2 Evolution equation for thin film 31

3 Thin film breakup on hydrophilic surfaces **33**
3.1 Spatial discretization 34
3.2 Time discretization 36
3.3 Boundary and initial conditions 38
3.4 Validation of the FVM solver 39
3.4.1 Disjoining pressure validation 40
3.4.2 Validation for film breakup 42
3.5 Contact line dynamics 43
3.5.1 Theoretical model for the critical flow rate 43
3.5.2 Numerical results 46

4 Film flowing over 3D curved substrates **51**
4.1 Continuity equation 51
4.2 Momentum equation 53
4.3 Pressure field 56
4.4 Numerical method 60
4.5 Boundary and initial conditions 66
4.6 Validation 67
4.7 Film past an obstacle 71

5 Absorption and distillation processes **77**
5.1 Overview 77
5.2 Structured packing 79
5.3 Problem setup 81
5.4 Results and discussion 84
5.5 Film over a corrugated layer of packing 91
5.5.1 Parametric study 97

6 Conclusion **101**

List of Figures

1.1 Possible configuration of a thin liquid layer over a solid substrate: drops (a), finger instability phenomenon leading to an array of parallel rivulets (b), continuous film break-up (c). . . . 1
1.2 Packed column used for CO_2 chemical absorption. 2

2.1 Dry-patch formation in liquid layer flowing over a solid surface. 6
2.2 Critical flow rate as a function of plate inclination and equilibrium contact angle, according to Eqs. (2.2) and (2.7). Water: $\rho = 997\,\mathrm{kg/m^3}$, $\mu = 0.0010\,\mathrm{Pa\,s}$, $\sigma = 0.073\,\mathrm{N/m}$ (a). Silicone oil: $\rho = 950\,\mathrm{kg/m^3}$, $\mu = 0.019\,\mathrm{Pa\,s}$, $\sigma = 0.021\,\mathrm{N/m}$ (b). Comparison with literature experimental data of [1] (c). 7
2.3 Notation used in [2]: modeling of the mass conservation (a); section of the ridge surrounding the contact line (b). 8
2.4 Shape of a stable dry-patch, generated perturbing the undisturbed film flow over an inclined plate: empirical model vs experimental results of [2]. $\alpha = 15°$, $Q_\infty = 19.7 \times 10^{-3}\,\mathrm{cm^2/s}$, $\theta_e = 30°$. 9
2.5 Phase I and phase II delimited by the interface Γ. 10
2.6 Surface tension forces acting on a control element of free-surface Γ and definition of principal radii of curvature. 11
2.7 Dependence of disjoining pressure on film thickness, $\delta = 0.1\,h_\infty$, $\theta = 90°$ and $(n, m) = (3, 2)$ (a). Control volume of liquid between the apparent contact line h_0 and the precursor film δ (b). 12
2.8 Stable rivulet flowing over a vertical plate (a), film breakup over an inclined plate (b) 17
2.9 Possible rivulet configurations as a function of the external action of shear for fixed liquid flow rate, according to Eq. (2.62). . 18
2.10 Free-surface shape predicted by similarity solution, Eqs. (2.81) and (2.82) in the case of: $\lambda = 0$, (a); $\lambda = 2$, (b). $\rho = 981.3\,\mathrm{kg/m^3}$, $\mu = 0.03642\,\mathrm{Pa\,s}$, $\sigma = 0.0384\,\mathrm{N/m}$, $\alpha = 30°$, $Q = 10^{-6}\,\mathrm{m^3/s}$. 22
2.11 Numerical results of [3]: film thickness distribution on the cylindrical occlusion for $\epsilon = 0.2$ (a); separation angle as a function of ϵ for $\theta_e = 20°$ (b). Coordinate β defining the position along the obstacle perimeter (c). 26
2.12 Sketch of a confined elongated bubble flowing inside a circular duct. 27

2.13 Diffuse interface separating liquid phase and vapor phase of a given fluid (a). Density profile across liquid-vapor interface (b). 29

3.1 Self-similar free surface profile of a film flowing over an inclined plate for equilibrium contact angle $\theta_e = 20°$ and for a wettable surface, $\theta_e = 0°$ (a); zoom of the solution near the apparent contact line for $\theta_e = 0°$ (b). $\alpha = 30°$, $Q_{in} = 0.01\,\mathrm{cm}^2/\mathrm{s}$. 41
3.2 Dynamic contact angle for 1D film flow as a function of contact line velocity, $\Delta x = 0.1\,h_\infty$ (a); influence of discretization accuracy on regression coefficients $C_{1,2}$ of Eq. (3.46) (b), (c). . . 42
3.3 Computed stationary film height (a); dry-patch validation with Eqs. (2.14), (2.15) and (2.16) (b). $Q_{in} = 5.9 \times 10^{-3}\,\mathrm{cm}^2/\mathrm{s}$, $\alpha = 30°$. 43
3.4 Control volume of liquid at the apex of the dry-patch (a); section of the control volume within the capillary ridge (b). 44
3.5 Critical film flux as a function of the plate inclination: theoretical model, Eqs. (3.67) and (3.68), vs experimental evidences of Podgorski et al. [2]. Liquid properties listed in table 3.1, $\theta_e = 30°$. 47
3.6 Comparison between critical flow rate deriving from numerical computations and theoretical model, Eqs. (3.67) and (3.68). $\theta_e = 20°$. 47
3.7 Moving contact line at different times (a); dry-patch apex position as a function of time (b). $Q_{in} = 7.5 \times 10^{-3}\,\mathrm{cm}^2/\mathrm{s}$, $\alpha = 30°$. 48
3.8 Dynamic contact angle as a function of the position over the contact line for two different flow rates (a). Dependence of the contact angle on contact line velocity, for $Q_{in} = 0.75$, 1.5, 2.0, $3.0 \times 10^{-2}\,\mathrm{cm}^2/\mathrm{s}$, $\alpha = 30°$ (b). Definition of the coordinate β, identifying the position along the contact line (c). 49

4.1 Control element of the curved surface Γ (locally approximated with its tangent plane) and definition of the local, non-orthogonal coordinates χ and η, obtained sectioning the substrate with two planes at $x = \text{const}$ and $y = \text{const}$. 52
4.2 Definition of the local, orthogonal coordinates χ^* and η^* on the solid substrate, needed for free-surface curvature calculation. . . 56
4.3 Portion of free-surface obtained sectioning with $O\chi\zeta$ and $O\eta\zeta$ planes, AB, AC, CD and BD being the free boundaries of the surface element. 57
4.4 Error % between real curvature and Eq. (4.33) over the corresponding rivulet distribution on the inclined plate from analytical solution of [4]. $\rho = 981.31\,\mathrm{kg/m}^3$, $\mu = 0.03642\,\mathrm{Pa\,s}$, $\sigma = 0.0384\,\mathrm{N/m}, \alpha = 60°$. 59
4.5 Problem definition: inclined reference plane Oxy, substrate surface and local coordinates χ, η. 60
4.6 Structured computational grid: nodes n_k, $k = 1$, 2, 3, 4, defining the i, j-th control surface element. 62

4.7 Section $y = L_y/2$ of the stationary free-surface profile (a). Section $x = L_x/2$ of the free-surface profile vs Young-Laplace equation (b). $\theta_e = 45°$. 68

4.8 Sections $y = L_y/2$ (a) and $x = L_x/2$ (b) of free-surface profile (continuous line) and substrate surface (dashed line) at different times: $t = 0.08$, 0.27, 0.46, 0.65 s. $\theta_e = 45°$. 69

4.9 Section $x = L_x/2$ of the stationary liquid layer distributions, obtained imposing four different surface wettabilities, the equilibrium contact angle ranging in $\theta_e \in [0°, 60°]$; test case given by table 4.2. 70

4.10 Simulated 3D curved substrate: test case T1 (a); test cases T2 and T3 (b). The reference Oxy plane is inclined at an angle $\alpha = 60°$ to the horizontal. 72

4.11 Test case T1. Substrate morphology (black isolines referred to $z = 0.14$, 0.29, 0.43, 0.57, 0.71, 0.86 cm) and stationary contact line (red line) defining the dry-patch: $\theta_e = 30°$ (a), $\theta_e = 0°$ (c); stationary film distribution over the curved substrate: $\theta_e = 30°$ (b), $\theta_e = 0°$ (d). $Q_\infty = 0.5\,\mathrm{cm}^2/\mathrm{s}$. 73

4.12 Test case T1: section $y = 1$ cm (corresponding to symmetry line $y = L_y/2$) of the two stationary liquid layer distributions over the substrate for two different surface wettabilities: $\theta_e = 30°$ (a); $\theta_e = 0°$ (b). $Q_\infty = 0.5\,\mathrm{cm}^2/\mathrm{s}$. 74

4.13 Normalized wetted area A_{WET} of the stationary solution as a function of imposed film flow rate Q_∞ and equilibrium contact angle θ_e: test case T2 (a); test case T3 (b). 75

4.14 Test case T3: substrate morphology (black isolines referred to $z = 0.06$, 0.11, 0.17, 0.23, 0.29, 0.34 cm) and contact lines (red lines) at different times, $t = 0.20$, 0.26, 0.35, 0.52, 0.83, 1.3 s (a); stationary film distribution over the curved substrate (b); section $y = 1.5$ cm of the stationary liquid layer distribution (c). $Q_\infty = 0.5\,\mathrm{cm}^2/\mathrm{s}$, $\theta_e = 30°$. 76

5.1 Sieve plate (a). Random packing (b). Smooth, perforated packing (c). Embossed, unperforated packing (d). 78

5.2 Design diagrams for: absorption (a); stripping (b). Molar fluxes entering and exiting the absorption/stripping column through sections 1 and 2 (c). 79

5.3 Elementary geometry of the corrugated sheet of packing. 80

5.4 Geometrical layout leading to wall boundary condition: cutting the free-surface profile at $y = 0$ and $y = \Delta y_0$, two isolines (black, curved lines) with spacing ΔL are obtained. 82

5.5 Investigated setup: 1D film down an inclined plate (a); confined inlet section L_{in} at $x = 0$ (b); plate bounded by lateral walls (c) 83

5.6 1D gravity driven film: capillary ridge shape for different equilibrium contact angles θ_e, $Q_{in} = 1\,\mathrm{cm}^2/\mathrm{s}$ (a); dynamic contact angle θ vs undisturbed film velocity u_∞ and imposed equilibrium contact angle θ_e: numerical results (symbols) and Eq.(5.12) (lines) (b). 84

5.7 Stationary rivulet distribution over the inclined plate for: $\theta_e = 60°$ (a), $\theta_e = 40°$ (b), $\theta_e = 20°$ (c). $\alpha = 60°$, $\dot{V}_{in} = 2\,\mathrm{cm}^3/\mathrm{s}$. . . . 85

5.8 Normalized wetted area of the rivulet as a function of the equilibrium contact angle (a). Normalized interface area of the rivulet as a function of the equilibrium contact angle (b). $\alpha = 60°$, $\dot{V}_{in} = 2\,\mathrm{cm}^3/\mathrm{s}$. 86

5.9 Comparison between rivulet profiles from solution of Eq. (5.13) and numerical simulation of rivulet build up: $\theta_e = 60°$ (a); $\theta_e = 50°$ (b). $\alpha = 60°$, $\dot{V}_{in} = 2\,\mathrm{cm}^3/\mathrm{s}$. 87

5.10 Liquid layer distribution over the inclined plate at $t = 0.19\,\mathrm{s}$ (a) and stationary distribution, $t = 0.49\,\mathrm{s}$ (b). Normalized wetted area as a function of time (c). $\theta_e = 60°$, Ka = 49.7, We = 0.0736. 88

5.11 Normalized wetted area at the stationary liquid distribution as a function of Weber number, $\theta_e = 60°$ (a); as a function of equilibrium contact angle, We = 0.0736 (b). Fluids listed in table 5.1 are simulated, plate inclination is fixed to $\alpha = 60°$. . . 89

5.12 Wetted area as a function of time for different values of θ_e, We = 0.459, Ka = 14.7 (a). Time to reach $A_{WET} = L_x\,L_y$ as a function of We and θ_e, Ka = 14.7 (b). $6 \times 5\,\mathrm{cm}^2$ plate. 90

5.13 Liquid layer distribution over the inclined plate at different times: $t = 0.2\,\mathrm{sec}$ (a); $t = 0.3\,\mathrm{sec}$ (b); $t = 0.5\,\mathrm{sec}$ (c); $t = 1.7\,\mathrm{sec}$ (d). We = 0.46, Ka = 14.7, $\theta_e = 60°$, $6 \times 5\,\mathrm{cm}^2$ plate. 91

5.14 Portion of packing geometry (front view). 92

5.15 Simulated geometry of the packing layer: corrugation angle $\phi = 45°$; base width $W = 2.1\,\mathrm{cm}$ and corrugation height $H = 0.7\,\mathrm{cm}$, leading to $W/H = 3$ for test cases T1, T2 and T3. A joint radius equal to $r = 3\,\mathrm{mm}$ is imposed in order to smoothen the sharp geometry of the packing layer. 93

5.16 Predicted stationary film thickness distribution over the packing layer (a) vs snapshot of the solution from the fully 3D simulation of [5] (b). Test case T1. 94

5.17 Periodic computational domain (a). Stationary liquid layer distribution (b). Test case T2. 95

5.18 Geometry of the corrugated sheet of packing (a). Liquid layer distribution over the packing geometry at $t = 1\,\mathrm{sec}$ (b). Liquid layer distribution at $t = 2\,\mathrm{sec}$ (c). Stationary solution, $t = 7\,\mathrm{sec}$ (d). Test case T2. 96

5.19 Contact line over the packing layer at $t = 0.25$, 0.44, 0.62, 0.80 (sec) (a). Normalized wetted area of the computational domain as a function of time, colored markers identifying the plotted contact lines (b). Re = 1.35, $\theta_e = 30°$, packing geometry G2. 97
5.20 Time to reach stationary liquid layer distribution as a function of Reynolds number and substrate wettability: investigated geometry G1 (a); investigated geometry G2 (b). 99
5.21 Stationary normalized wetted area of the simulated packing layer versus imposed Reynolds number. Geometries G1 and G2 investigated, $\theta_e = 45°$. 99

List of Tables

3.1 Physical properties of the simulated silicone oil (poly-dimethyl-siloxane) and imposed parameters defining the disjoining pressure. 39

4.1 Properties of the simulated liquid, 1−methylepiperazine, at $T = 25°C$ and $p = 1\,\text{atm}$ and imposed parameters defining disjoining pressure model 67
4.2 Simulated test case: hole dimension, capillary length, liquid volume entering the domain. 68
4.3 Computational domain dimensions $L_x \times L_y$, inclination of the reference plane with respect to the horizontal α, shear applied by the external gas flow $\tau_g = |\boldsymbol{\tau_g}|$, obstacle size H and number of obstacles $k_{x,y}$ for the investigated test cases, T1, T2 and T3. . 72

5.1 Physical properties of 1−methylepiperazione at $T = 25°C$ and $p = 1\,\text{atm}$. 84
5.2 Simulation time corresponding to the setup of figure 5.8. 91
5.3 Definition of the simulated test cases and liquids properties. . . 94
5.4 Investigated packing geometries, G1 and G2, and simulated liquid, 1-methylepiperazione. 97

Nomenclature

α	plate inclination
α^*	angle between local coordinates χ, η.
$\alpha_{\chi,\eta}$	inclination of the substrate surface to the reference Oxy plane.
β	angle between normal to the contact line and plate downhill direction
$\hat{\boldsymbol{g}}$	versor of the gravity acceleration
$\hat{\boldsymbol{n}}_{\boldsymbol{I}}$	versor identifying free-surface outward normal direction
$\hat{\boldsymbol{n}}_{\boldsymbol{s}}$	versor identifying substrate outward normal direction
$\hat{\boldsymbol{n}}$	versor identifying outward normal direction
$\hat{\boldsymbol{t}}_{\boldsymbol{\chi},\boldsymbol{\eta}}$	substrate tangential directions identifying χ and η coordinates
$\hat{\boldsymbol{t}}$	versor identifying tangential direction
$\boldsymbol{\tau_g}$	shear stress applied by the external gas flow
$\boldsymbol{Q}$	$= (q,\, s)$, film flux
$\boldsymbol{u}$	$= (u,\, v,\, w)$, liquid velocity
χ, η, ζ	local coordinates
δ	precursor film thickness
ΔS	area of control element base surface
Δt	time step
ΔV	control element volume
Δx	spatial discretization step
$\dot{V}$	volumetric liquid flow rate
$\hat{G}$	chemical potential
κ_m	mean curvature of the free-surface

κ_s mean curvature of the solid substrate

Bo $= \rho\, g\, h_\infty^2/\sigma$, Bond number

Ca $= \mu\, u_\infty/\sigma$, capillary number

Ka $= \sigma\,(\mu^4\, g/\rho)^{-1/3}$, Kapitza number

Re $= \rho\, u_\infty\, h_\infty/\mu$, Reynolds number

We $= \rho\, {u_\infty}^2\, h_\infty/\sigma$, Weber number

μ dynamic viscosity

ϕ corrugation angle

Π disjoining pressure

ψ angle between tangent to the contact line and plate downhill direction

ρ $= N/V$, number density in section 2.7

ρ density

σ surface tension

θ dynamic contact angle

θ_e equilibrium contact angle

A_{INT} interface area

A_{SUB} substrate area

A_{WET} wetted area

g gravity acceleration

H height

h film thickness

h_∞ undisturbed film thickness

i, j computational grid element

l_c $= (\sigma/(\rho\, g))^{1/2}$ capillary length

l_v $= (\mu^2/(\rho^2\, g))^{1/3}$ viscosity length

$L_{x,y}$ inclined plate dimensions

p pressure

Q_∞ undisturbed film flux per unit length

r	radius of curvature
t	time
u_∞	undisturbed film average velocity
u_c	contact line velocity
W	width
x, y, z	Cartesian directions

Chapter 1

Introduction

The evolution of a thin layer of liquid over a non-wettable surface is a complex phenomenon, involving physical discontinuities induced by moving contact lines and transition between the different flow patterns:

- still or moving droplet, figure 1.1(a);
- rivulet, figure 1.1(b) showing finger instability occurred during wetting of an inclined plate;
- continuous film, figure 1.1(c) showing the break-up of a continuous film into two rivulets with dry-patch generation.

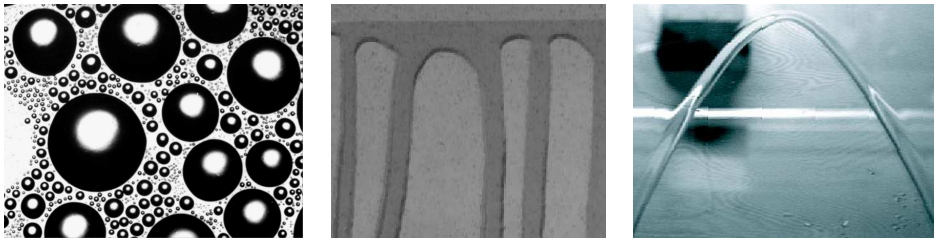

(a) (b) (c)

Figure 1.1: Possible configuration of a thin liquid layer over a solid substrate: drops (a), finger instability phenomenon leading to an array of parallel rivulets (b), continuous film break-up (c).

Moreover, a combination of the above mentioned configurations may appear during a wetting phenomenon, making the understanding of the thin film hydrodynamics even more difficult due to the large number of possible configurations.
On the other side, a number of engineering problems requires the knowledge of the liquid distribution over a solid substrate. Above all, coating process is mainly driven by the interaction between a liquid film slowly flowing and the surface to be covered. In-flight icing phenomenon on aircraft surface is also driven by the evolution of a water layer fed by super-cooled drops from the cloud. The liquid distribution, which depends on the cloud water content

and the fluid flow field and temperature, influences the location and shape of ice accretion areas, which in turn greatly affect the aircraft aerodynamics and, thus, the flight safety. Fogging and defogging of a car windshield or heat transfer on dehumidifier fin surfaces are also affected by condensation and evaporation phenomena with droplets growth, coalescence and motion over solid substrates. Again, windshield fogging has potentially safety consequences and is thus strictly regulated, while the different water layer regimes are one of the dominant effects in determining the performances of dehumidifier and condenser heat exchanger. Even in chemical engineering a lot of interest has been put in flowing films in the recent 30 years. In fact, absorption and distillation processes involve the evolution of a thin layer of liquid. In carbon dioxide capture through chemical absorption in structured packing, gas CO_2 flows up while a liquid solvent, which has to capture carbon, flows down through a packed column, composed by a collection of structured corrugated sheets, as shown in figure 1.2. The absorption process is more efficient when the packed layers are covered by a continuous film, rather than drops or rivulets. Both numerical and experimental literature are available, but it is clearly difficult to look inside the packed columns, making the numerical approach much more suitable.

Figure 1.2: Packed column used for CO_2 chemical absorption.

Several works concerning these topics are available in literature, with a great effort put by many authors. In [6], the performances of a vertical fin array belonging to a finned dehumidifier are numerically investigated. The problem being multiscale and multiphysics (air flow exchanging mass and heat with the liquid film at the fin surface due to condensation, heat conduction in the solid domain of the fins), the fluid flow convection problem and the conduction problem are solved separately and coupled using the film evolution (smaller length scale) to define the boundary condition that are exchanged between solid and fluid domain. A procedure was developed by the authors in order to evaluate the water layer thickness, choosing between continuous film and still droplet regime. In particular, knowing the condensating flow rate from an energy balance, it is possible to write the continuity equation for the film, eval-

uating the film velocity from the known shear stress applied by the fluid flow, which is supposed to be the driving forces together with gravity. Since the energy balance defining the condensation process strongly depends on the film flow pattern, the droplets growth and coalescence are also modeled through a Lagrangian approach and a trigger defining the transition from droplet regime to film regime is defined in terms of critical drop diameter. A similar approach is also used in [7] for investigating in-flight icing phenomenon.

A lot of literature works treat the evolution of a thin liquid film over a solid substrate or the droplet growth, motion and coalescence by means of numerical, analytical or experimental approaches. Apart the Nusselt theory, which is the precursor work involving the understanding of thin film behavior, Hartley et al. [8] (1964) and Wilson [9] (1974) proposed different theoretical studies for predicting the condition at which a continuous film may break-up in rivulets, while Bretherton [10] (1961) first applied lubrication theory for studying the shape of a confined gas bubble immersed in a liquid inside a small channel. The lubrication theory, which has the great advantage to reduce the physical problem to a 2D partial differential equation, is mostly used for investigating droplets behavior over a solid substrate and for applications involving coating process. The contact line dynamics modeling, which is required for simulating real test cases, has been recently introduced within the lubrication theory, thanks to Schwartz et al. [11], who used the disjoining pressure model together with the assumption of a precursor film always wetting the substrate. Only hydrophilic surfaces ($\theta_e \leq 90°$) can be investigated, due to the mathematical limit of the lubrication theory itself. However, the allowed equilibrium contact angle is even lower due to the approximate evaluation of the capillary pressure, which is strictly connected with the free-surface curvature; in fact, equilibrium contact angles up to 20° only are investigated in literature.

On the other side, a fully 3D approach is usually adopted for simulating absorption/distillation through structured packing. Since a packed column may have a diameter of 10 m, while the characteristic dimension of structured packing is of the order of 20 cm and the film height may be less than a millimeter [12], the problem is inherently multiscale. Thus, a full CFD approach is typically limited to the investigation of a single facet of the problem: most analysis, in fact, are focused on the hydrodynamic behavior of a liquid along plane surfaces. Coupling the film problem and the flow problem resolutions as done by [6] may be an important improvement in order to reduce the computational costs and gain useful information for packing geometry optimization.

The aim of this work is the 2D modeling of discontinuous thin film of liquid, driven by gravity and shear of an external gas flow over a non-wettable solid substrate, through lubrication theory. To do this, a new solver is developed in `FORTRAN` language. Thanks to the available numerical literature [11, 13, 14], efficient and accurate numerical methods can be implemented for the solution of the mathematical problem governing thin film evolution. The modeling of surface wettability is reached via disjoining pressure, according to [3, 11, 15]. Equilibrium contact angles up to 90° can be investigated through the full modeling of capillary pressure (thus the usual small slope approximation must be

abandoned). The general case of a liquid film flowing over a 3D curved substrate, as it happens in the most of real problems, can also be investigated extending the governing lubrication equations, which are originally defined for a film flowing over an inclined plate, with the advantage of keeping a 2D approach.
The possibility of investigating liquid film evolution over non-wettable 3D substrate obviously enlarges the range of engineering applications that can be analyzed via lubrication theory. In fact, the developed solver is applied to the case of CO_2 absorption through structured packing, where the knowledge of the hydrodynamics of the liquid solvent inside the packing geometry, which is composed of an ensemble of corrugated sheets, is crucial for a proper optimization. In fact, the higher the wetted area of the packing geometry, the higher the free-surface area, which is needed for capturing CO_2. Such an approach, also allows to strongly reduce the computational costs with respect to a full 3D approach, leading to an improved flexibility. In fact, the solution of the liquid film over the packing layers can be coupled with the solution of CO_2 gas flow through an exchange of boundary condition.

Chapter 2

Flowing films

2.1 Phenomenological models

The first theoretical work about flowing film belongs to Nusselt (1916) [16]. The so called Nusselt theory models the film condensation over a vertical plate: assuming laminar film flow pattern, fully developed thermal profile and latent heat driving the heat transfer process, the model is able to predict both the film thickness and the heat transfer coefficient over the plate.
A similar approach was also used by Hartley and Murgatroyd (1964) [8] for calculating the thickness of an undisturbed film flowing down a vertical plate or driven by shear of an external gas flow. In their work they also studied the separation of an uniform film, leading to dry-patch generation, proposing two different criteria for the calculation of a critical mass flow rate, at witch film separation may occur, generating a stable dry-patch:

- minimum power configuration for establishing if a given liquid flow rate will arrange in a single rivulet rather than split in more rivulets;
- force-balance at the upstream point of the dry-patch.

Knowing the fluid properties, the external actions of gravity and shear and assuming that the fluid is Newtonian and incompressible, the velocity profile for a laminar and uniform liquid film flowing over an inclined plate can be calculated,

$$u = \frac{\rho\, g}{\mu}\, \sin\alpha \left(h_\infty\, z - \frac{z^2}{2} \right) + \frac{\tau_g}{\mu}\, z \tag{2.1}$$

$z \in [0,\, h_\infty]$ being the normal outward plate direction, h_∞ the thickness of the undisturbed film, α the plate inclination with respect to the horizontal and τ_g the shear applied by the external gas flow. Note that Eq. (2.1) is valid in the restrictive case of τ_g acting along the plate downhill or uphill directions.
Integrating the velocity profile across the film thickness leads to the film flux:

$$Q_\infty = u_\infty\, h_\infty = \frac{\rho\, g}{3\,\mu}\, \sin\alpha\, {h_\infty}^3 + \frac{\tau_g}{2\,\mu}\, {h_\infty}^2 \tag{2.2}$$

Thus, specifying the undisturbed film flux Q_∞ the film thickness h_∞ can be calculated. It is important to point out that, when gravity and shear act in

opposite directions, Eq. (2.2) may have two different positive solutions for h_∞. Since both the solutions have physical meanings, the energetic approach of [8] can be followed in order to determine the most probable configuration of the film, that is defined by minimizing the total power. The film power per unit width is given by the contributions of potential, kinetic and surface energy variations:

$$P_p = \rho\, g\, \cos\alpha \int_0^{h_\infty} u\, z\, dz \tag{2.3}$$

$$P_k = \frac{1}{2}\,\rho \int_0^{h_\infty} u^3\, dz \tag{2.4}$$

$$P_\sigma = \sigma\ u|_{h_\infty} \tag{2.5}$$

Similar energetic approaches for choosing the more suitable liquid layer configurations can be found in [17, 18].
Applying the force-balance based method given in [8] allows to trace the critical flow rate at which the film may break in more rivulets as a function of the external actions of gravity and shear.

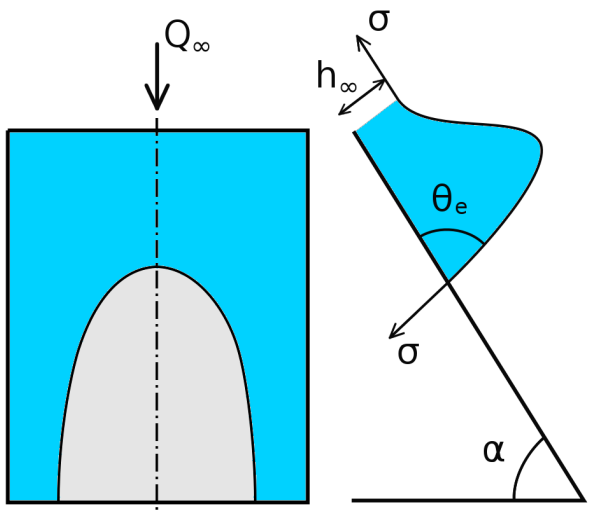

Figure 2.1: Dry-patch formation in liquid layer flowing over a solid surface.

Consider a film flowing down an inclined plate and imagine that the undisturbed flow breaks generating a dry-patch. Referring to the liquid section surrounding the stagnation point, see figure 2.1, the mechanical equilibrium between the surface tension and the liquid pressure acting on the liquid-gas interface leads to,

$$\sigma\ (1 - \cos\theta_e) = \frac{1}{2}\,\rho \int_0^{h_\infty} u^2\, dz + \rho\, g\, \cos\alpha \int_0^{h_\infty} z\, dz \tag{2.6}$$

θ_e being the equilibrium contact angle.
For the case of purely gravity driven film (i.e. $\tau_g = 0$) in Eq. (2.1), we can integrate Eq. (2.6) in order to get:

$$\sigma\ (1 - \cos\theta_e) = \frac{3}{5}\,\rho\, {u_\infty}^2\, h_\infty + \rho\, g\, \cos\alpha\, \frac{{h_\infty}^2}{2} \tag{2.7}$$

Eqs. (2.7) and (2.2) can be rewritten referring to the critical film flow rate:

$$Q_{CR} = u_{CR}\, h_{CR} = \frac{\rho\, g}{3\,\mu}\, \sin\alpha\, {h_{CR}}^3 \tag{2.8}$$

$$\sigma\ (1 - \cos\theta_e) = \frac{3}{5}\,\rho\, {u_{CR}}^2\, h_{CR} + \rho\, g\, \cos\alpha\, \frac{{h_{CR}}^2}{2} \tag{2.9}$$

Solving together Eqs. (2.8) and (2.9) allows to predict the critical flow rate Q_{CR} for given plate inclination and equilibrium contact angle. Below the critical value Q_{CR}, a stable dry-patch appears after the film breakup.

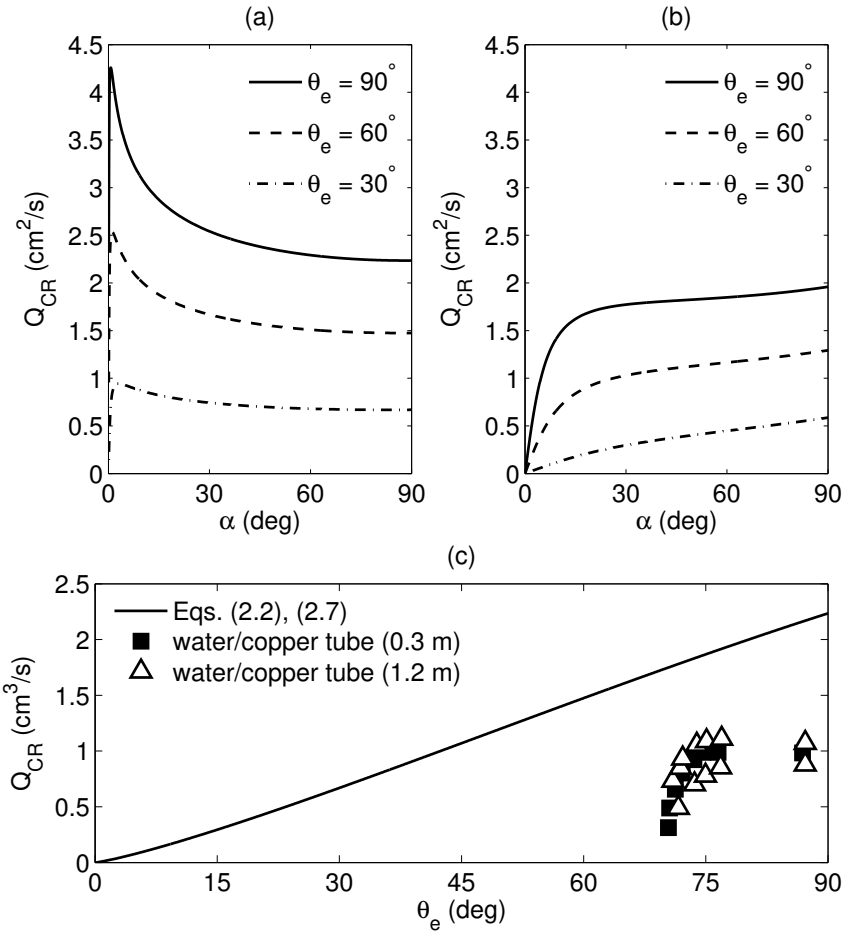

Figure 2.2: Critical flow rate as a function of plate inclination and equilibrium contact angle, according to Eqs. (2.2) and (2.7). Water: $\rho = 997\,\mathrm{kg/m^3}$, $\mu = 0.0010\,\mathrm{Pa\,s}$, $\sigma = 0.073\,\mathrm{N/m}$ (a). Silicone oil: $\rho = 950\,\mathrm{kg/m^3}$, $\mu = 0.019\,\mathrm{Pa\,s}$, $\sigma = 0.021\,\mathrm{N/m}$ (b). Comparison with literature experimental data of [1] (c).

Figures 2.2 (a) and 2.2 (b) shows the predicted behavior of the critical flow rate for two different liquids (water and silicone oil), which mainly differ from each other in the dynamic viscosity. In fact, when high viscosity liquids are considered, the force arising from liquid inertia becomes less and less significant, compared to surface tension and hydrostatic pressure. Results obtained from Eqs. (2.2) and (2.7) are not consistent with the available experimental results, as shown in figure 2.2 (c), since the weight of the stagnant liquid in

the capillary ridge appearing close to the contact line is not taken into account when imposing force balance, Eq. (2.6). However, the model proposed by Hartley and Murgatroyd, [8], represents a first step for a better understanding of the hydrodynamics of thin liquid layers.
More accurate models, even able to predict the dry-patch shape, are available in literature. Podgorski et al. [2] studied the case of a film flowing over an inclined plate. They investigated experimentally the dry-patch generation, perturbing the undisturbed flow, with the aim of tracing the critical flow rate and the eventual shape of the stable dry-patch. Then, they proposed an empirical model for describing the stable dry-patch shape, following the same approach of [9].

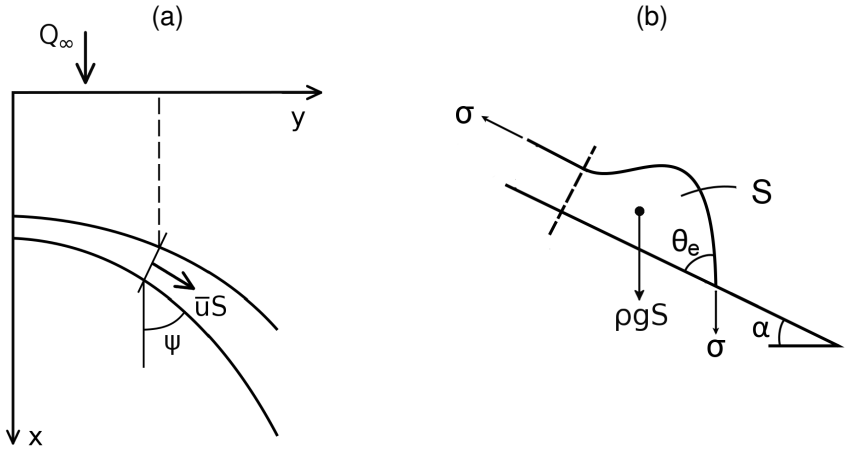

Figure 2.3: Notation used in [2]: modeling of the mass conservation (a); section of the ridge surrounding the contact line (b).

Assuming that a capillary ridge, where the liquid that would otherwise cover the dry spot is collected, surrounds the contact line, as shown in figure 2.3(b), they wrote the continuity equation and the mechanical equilibrium for a small element of ridge,

$$\bar{u}\, S = Q_\infty\, y \tag{2.10}$$

$$\sigma\ (1 - \cos\theta_e) = \rho\, g\, S\ \sin\alpha\ \sin\psi \tag{2.11}$$

$\bar{u}$ and S being the average liquid velocity and the area of the ridge cross section, ψ being the angle of the tangent to the contact line with the plate downhill direction.
Assuming that the liquid velocity inside the ridge is given by a Poiseuille-type profile, with the flow driven by gravity and viscous dissipation, and that the ridge shape is well approximated by a circular arc leads to:

$$\bar{u} = m\, f_1(\theta_e)\, \frac{\rho\, g\, S}{\mu}\ \sin\alpha\ \cos\psi \tag{2.12}$$

$$f_1 = \frac{(1 - \cos\theta_e)^2}{\theta_e - \cos\theta_e\ \sin\theta_e} \tag{2.13}$$

The estimation of the parameter m, which mainly depends on the ridge shape, comes from the analytical integration of the velocity profile over the ridge section under the above mentioned assumptions. However, the authors of [2,19] adjusted the calculated value of m in order to fit the experimental results, taking into account the discrepancy from the circular arc approximation of the ridge. Combining Eqs. (2.10), (2.11) and (2.12), the parametric curve of the contact line can be obtained:

$$x = \frac{r}{3}\left(1 - \frac{1 - 3\,\cos^2\psi}{\sin^3\psi}\right) \tag{2.14}$$

$$y = r\,\frac{\cos\psi}{\sin^2\psi} \tag{2.15}$$

with r being the contact line radius of curvature at the apex:

$$r = m\,f_2(\theta_e)\,\frac{\sigma^2}{\rho\,g\,\mu}\,\left(Q_\infty\,\sin\alpha\right)^{-1} \tag{2.16}$$

$$f_2 = \frac{(1 - \cos\theta_e)^4}{\theta_e - \cos\theta_e\,\sin\theta_e} \tag{2.17}$$

The results from the semi-empirical model, Eqs. (2.14), (2.15) and (2.16), and

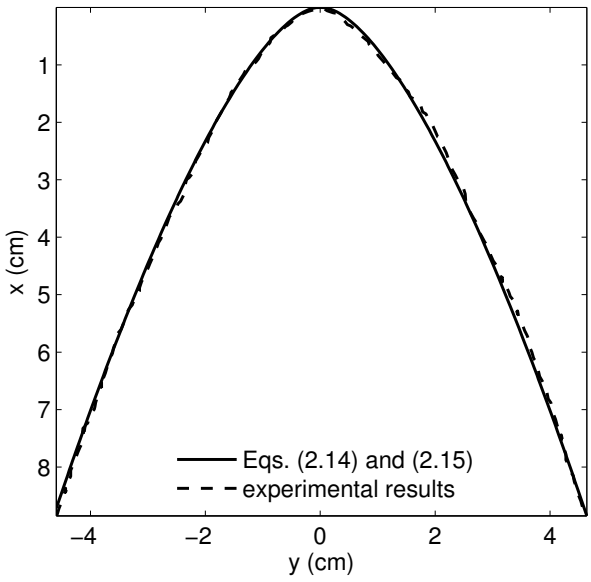

Figure 2.4: Shape of a stable dry-patch, generated perturbing the undisturbed film flow over an inclined plate: empirical model vs experimental results of [2]. $\alpha = 15°$, $Q_\infty = 19.7 \times 10^{-3}\,\mathrm{cm}^2/\mathrm{s}$, $\theta_e = 30°$.

experimental tests of [2] are compared in figure 2.4, showing a perfect agreement between predicted and observed dry-patch shape. Tests were run on an inclined glass plate, covered by a thin layer of silicone oil, PDMS Rhodorsil 47V20 ($\rho = 950\,\mathrm{kg/m}^3$, $\mu = 0.019\,\mathrm{Pa\,s}$, $\sigma = 0.021\,\mathrm{N/m}$), the measured equilibrium contact angle being equal to $\theta_e = 30°$. For such a case, the theoretical

value of the coefficient m is equal to $m = 0.23$, but it was adjusted to $m = 0.33$ in [2]. Thus, the value $m = 0.33$ is used to compare the empirical model with the experimental dry-patch contact line in figure 2.4.

2.2 Lubrication approximation

The mentioned studies just show simplified models, that are not able to predict the liquid layer distribution over the physical domain, but give information about the tendency of the liquid flow to arrange as a continuous film rather than an ensemble of rivulets. Even using such models for modeling the rivulet breakup and the transition between different flow patterns via a Lagrangian approach is not possible. In fact, they only provide information about the breakup threshold in terms of critical flow rate and the eventual dry-patch shape, but we still do not know where and when the breakups take place. Moreover, the validity of the empirical model proposed in [2], which is able to predict the eventual dry-patch shape, is limited to the experimental setup it is compared to. Thus, solving the 2D governing balance equations still represents the only way to fully understand the hydrodynamics of flowing films. Navier-Stokes equations can be simplified when thin liquid layers are involved, thanks to the well known lubrication theory, which allows for integration across the film thickness, leading to a 2D mathematical approach.

2.2.1 Capillary pressure

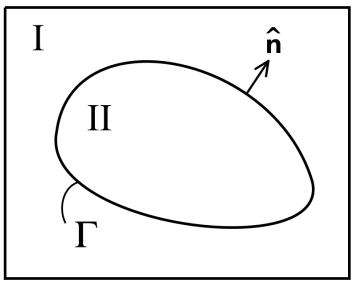

Figure 2.5: Phase I and phase II delimited by the interface Γ.

An interface exists when two immiscible fluids (let's call them I and II) are in contact with each other, as shown in figure 2.5. This interface (or free-surface) persists thanks to the surface tension, acting at the interface. Thus, there is a pressure differential between fluids I and II when the free-surface is curved [20]. This pressure differential is called capillary pressure and it is given by the Young-Laplace equation,

$$p_{II} - p_I = 2\,\sigma\,\kappa_m = \sigma\,\left(\frac{1}{r_1} + \frac{1}{r_2}\right) \tag{2.18}$$

κ_m being the so called mean curvature and $r_{1,2}$ being the principal radii of curvature. Referring to figure, $r_{1,2}$ may be defined as the two radii of curvature standing in two planes that are at the same time normal to each other and normal to the interface Γ.

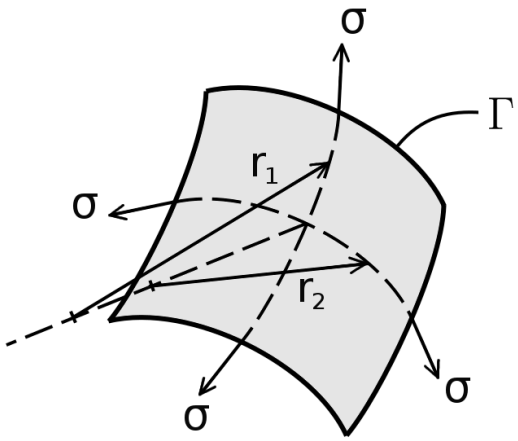

Figure 2.6: Surface tension forces acting on a control element of free-surface Γ and definition of principal radii of curvature.

According to [13, 21], the mean curvature of a 3D curved surface $h(x, y)$ is given by:

$$2\,\kappa_m = \frac{\frac{\partial^2 h}{\partial x^2}\left[1+\left(\frac{\partial h}{\partial y}\right)^2\right] + \frac{\partial^2 h}{\partial y^2}\left[1+\left(\frac{\partial h}{\partial x}\right)^2\right] - 2\,\frac{\partial h}{\partial x}\,\frac{\partial h}{\partial y}\,\frac{\partial^2 h}{\partial x \partial y}}{\left[1+\left(\frac{\partial h}{\partial x}\right)^2+\left(\frac{\partial h}{\partial y}\right)^2\right]^{3/2}} \tag{2.19}$$

When low values of the equilibrium contact angle are imposed, only small free-surface inclinations can be observed and the small slope approximation,

$$2\,\kappa_m \simeq \frac{\partial^2 h}{\partial x^2} + \frac{\partial^2 h}{\partial y^2} = \nabla^2 h \tag{2.20}$$

is used for reducing Eq. (2.19). It is worth to point out that contact angles higher than 20° have never been investigated in the available literature involving thin liquid layer 2D simulations under lubrication approximation [3, 11, 14, 15, 22], since results would not be consistent anymore if small slope approximation was assumed.

2.2.2 Disjoining pressure

The disjoining pressure is related to the intermolecular forces, that arise when two surfaces (solid substrate and liquid-air interface) are put in close contact. The authors of [11] introduced the disjoining pressure Π as,

$$\Pi = B\left[\left(\frac{\delta}{h}\right)^n - \left(\frac{\delta}{h}\right)^m\right] \tag{2.21}$$

where $1 < m < n$, $B > 0$, the reference height h_∞ is the undisturbed film thickness and $\delta << h_\infty$ is the precursor film thickness.
The first term of Eq. (2.21) represents liquid-solid repulsion, while the second is attractive, leading to a stable thickness δ: the repulsion component of the disjoining pressure dominates when the film thickness is lower than the precursor one, $h < \delta$, while the attractive component dominates when $h > \delta$, as shown in figure 2.7(a). Thus, the liquid layer is forced toward this precursor film thickness, allowing to solve the contact line singularity: if the precursor film was not assumed, the non-slip condition at the wall would not let the contact line move toward the solid surface. Moreover, using the disjoining pressure for modeling the wetting dynamics, the apparent contact line can be easily traced over the domain with *a posteriori* procedure. The positive exponents n, m and the precursor film thickness δ depend on the intermolecular forces acting between the surfaces close to each other. The coefficient B can be determined from the known equilibrium contact angle θ_e, which is used for describing the substrate wettability.

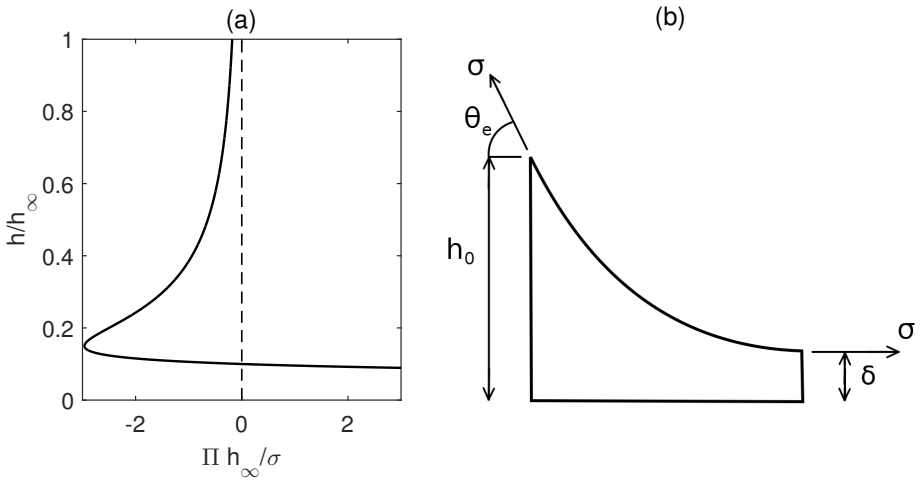

Figure 2.7: Dependence of disjoining pressure on film thickness, $\delta = 0.1\, h_\infty$, $\theta = 90°$ and $(n, m) = (3, 2)$ (a). Control volume of liquid between the apparent contact line h_0 and the precursor film δ (b).

Schwartz and Eley [11] imposed the equilibrium between disjoining and capillary pressure, acting on the macroscopic control volume of liquid close to the apparent contact line shown in figure 2.7(b),

$$-\int_\delta^{h_0} \frac{\sigma}{r}\, dh = \int_0^{h_0} \Pi\, dh - \int_0^{\delta} \Pi\, dh \tag{2.22}$$

where $\delta << h_0$, r is the free-surface curvature and Π is given by Eq. (2.21). Expressing the radius of curvature r as,

$$r = \frac{1}{\sin\varphi}\frac{dh}{d\varphi} \tag{2.23}$$

φ being the free-surface inclination, the LHS of Eq. (2.22) can be integrated,

$$\begin{aligned} -\int_{\delta}^{h_0} \frac{\sigma}{r}\, dh &= -\sigma \int_0^{\theta_e} \sin\varphi \, d\varphi \\ &= -\sigma \, (1 - \cos\theta_e) \end{aligned} \tag{2.24}$$

Assuming $\delta/h_0 \to 0$, integration of Eq. (2.22) RHS leads to:

$$\int_{\delta}^{h_0} B \left[\left(\frac{\delta}{h}\right)^n - \left(\frac{\delta}{h}\right)^m \right] dh \simeq -B\,\delta\, \frac{n-m}{(n-1)\,(m-1)} \tag{2.25}$$

Substituting Eqs. (2.24) and (2.25) to Eq. (2.22) allows to express B as:

$$B = \frac{(n-1)\,(m-1)}{n-m}\, \frac{\sigma}{\delta}\, (1 - \cos\theta_e) \tag{2.26}$$

The authors of [15] demonstrated that Eq. (2.26) is valid for an infinitesimally small precursor film, but leads to a deviation from the specified equilibrium contact angle when finite values of δ are imposed, as it usually happens in numerical computations. Moreover, the contribution of the capillary pressure in Eq. (2.22) must be corrected as the small slope approximation is assumed:

$$\begin{aligned} \int_{\delta}^{h_0} \frac{d^2h}{dx^2}\, dh &= \int_0^{\theta_e} \tan\varphi \, d\,(\tan\varphi) \\ &= \frac{1}{2}\, \tan^2\theta_e \neq 1 - \cos\theta_e \end{aligned} \tag{2.27}$$

The expression of B is thus corrected as follows,

$$B = f\, \frac{(n-1)\,(m-1)}{2\,(n-m)}\, \frac{\sigma}{\delta}\, \tan^2\theta_e \tag{2.28}$$

$$f = 1 + 6.069\,\tilde{\delta} + 161.7\,\tilde{\delta}^2 - 1547\,\tilde{\delta}^3 + 5890\,\tilde{\delta}^4 \tag{2.29}$$

where $\tilde{\delta} = \delta/h_\infty$ is the dimensionless precursor film thickness.
The correction coefficient f, obtained by means of a numerical procedure in [15], is consistent with the Tanner-Hoffman-Voinov formula for a 1D film flowing down an inclined plate,

$$\theta^3 = {\theta_e}^3 + C\, \frac{\mu\, u_c}{\sigma} \tag{2.30}$$

where θ is the dynamic contact angle, C is a constant and u_c is the contact line velocity:

$$u_c = u_\infty\, \frac{1 - (\delta/h_\infty)^3}{1 - \delta/h_\infty} \tag{2.31}$$

The dependence of the contact angle on the contact line velocity is largely reported in literature [15, 23, 24], as it will be better explained in section 2.4, and Eq. (2.30) has been compared with experimental results in [23], showing an excellent agreement.
Only disjoining pressure model is presented for substrate wettability modelling,

but an other approach can be used instead. In the context of 3D VOF simulations of a droplet moving on a solid surface, the authors of [24] imposed a slip boundary condition at the wall,

$$u_w = \lambda \left.\frac{\partial u}{\partial z}\right|_w \tag{2.32}$$

λ being the slip length. Even if both models have physical meanings, precursor film model is usually preferred in thin liquid layer simulations involving lubrication approximation, since it was demonstrated that it leads to lower computational cost [25].

2.3 Governing equation

Consider a thin liquid film of height h flowing over an inclined plate, driven by both gravity and shear. Let α be the plate inclination with respect to the horizontal, $\boldsymbol{\tau_g} = (\tau_x, \tau_y)$ the shear applied by an external gas flow, h_∞ and u_∞ the undisturbed film height and average velocity, calculated according to Nusselt theory.
Assuming that the liquid behaves as an incompressible fluid and u, v, w being the liquid velocities along the Cartesian coordinates, the continuity equation for an incompressible fluid gives:

$$\frac{\partial u}{\partial x} + \frac{\partial v}{\partial y} + \frac{\partial w}{\partial z} = 0 \tag{2.33}$$

Integrating the continuity equation across the film thickness h leads to:

$$\int_0^h \frac{\partial u}{\partial x}\, dz + \int_0^h \frac{\partial v}{\partial y}\, dz + \int_0^h \frac{\partial w}{\partial z}\, dz = 0 \tag{2.34}$$

Knowing that

$$\int_0^h \frac{\partial w}{\partial z}\, dz = [w]_0^h = w_h - w_0 \tag{2.35}$$

and applying Leibniz's formula,

$$\int_0^h \frac{\partial f}{\partial \xi}\, dz = \frac{\partial}{\partial \xi} \int_0^h f\, dz - f|_{\xi,h}\, \frac{\partial h}{\partial \xi} \tag{2.36}$$

Eq. (2.34) gives:

$$\frac{\partial}{\partial x} \int_0^h u\, dz - u_h \frac{\partial h}{\partial x} + \frac{\partial}{\partial y} \int_0^h v\, dz - v_h \frac{\partial h}{\partial y} + w_h - w_0 = 0 \tag{2.37}$$

Applying the non-slip condition at the solid substrate and the interface condition at the free-surface

$$w_0 = 0,\ w_h = \frac{\partial h}{\partial t} + u_h \frac{\partial h}{\partial x} + v_h \frac{\partial h}{\partial y} \tag{2.38}$$

and introducing the average liquid velocities across the film thickness,

$$\bar{u} = \frac{1}{h}\int_0^h u\,dz,\ \bar{v} = \frac{1}{h}\int_0^h v\,dz \tag{2.39}$$

Eq. (2.37) can be recasted, leading to:

$$\frac{\partial h}{\partial t} + \frac{\partial}{\partial x}\left(\bar{u}\,h\right) + \frac{\partial}{\partial y}\left(\bar{v}\,h\right) = 0 \tag{2.40}$$

Adopting the compact notation

$$\bar{\boldsymbol{u}} = \left(\bar{u},\,\bar{v}\right),\ \nabla = \left(\frac{\partial}{\partial x},\,\frac{\partial}{\partial y}\right) \tag{2.41}$$

and introducing the film flux $\boldsymbol{Q}$, continuity equation can be rewritten as:

$$\frac{\partial h}{\partial t} = -\nabla\cdot\left(\bar{\boldsymbol{u}}\,h\right) = -\nabla\cdot\boldsymbol{Q} \tag{2.42}$$

The average film velocities $\bar{u}$ and $\bar{v}$ can be expressed by means of the momentum equation. When thin liquid films are involved, the following assumptions can be done:

- incompressible fluid;
- Newtonian fluid;
- constant fluid properties through film;
- non-slip condition at the solid substrate;
- shear applied by the external gas flow at the free-surface.

Also assuming,

- negligible inertia forces, i.e. low Reynolds number:

$$\mathrm{Re} = \frac{\rho\,u_\infty\,h_\infty}{\mu} \leq 1 \tag{2.43}$$

allows to simplify the Navier-Stokes equations, reducing the 3D physical problem to a 2D mathematical problem. Under the above mentioned assumptions, momentum equations reduce to,

$$\frac{\partial p}{\partial x} = \mu\,\frac{\partial^2 u}{\partial z^2} \tag{2.44}$$

$$\frac{\partial p}{\partial y} = \mu\,\frac{\partial^2 v}{\partial z^2} \tag{2.45}$$

$$\frac{\partial p}{\partial z} = 0 \tag{2.46}$$

the pressure p being equal to the sum of the dynamic pressure and the hydrostatic pressure.
Solving Eqs. (2.44) and (2.45) with the non-slip boundary condition at the substrate and free-surface boundary condition at the liquid-gas interface

$$u_0 = 0,\ \mu \left.\frac{\partial u}{\partial z}\right|_h = \tau_x \tag{2.47}$$

$$v_0 = 0,\ \mu \left.\frac{\partial v}{\partial z}\right|_h = \tau_y \tag{2.48}$$

gives,

$$u = \frac{1}{\mu}\frac{\partial p}{\partial x}\left(\frac{z^2}{2} - z\,h\right) + \frac{\tau_x}{\mu}\,z \tag{2.49}$$

$$v = \frac{1}{\mu}\frac{\partial p}{\partial y}\left(\frac{z^2}{2} - z\,h\right) + \frac{\tau_y}{\mu}\,z \tag{2.50}$$

$\tau_{x,y}$ being the components of the shear $\boldsymbol{\tau_g}$, applied by the external gas flow, along the Cartesian directions x and y.
Eqs. (2.49) and (2.50) can be integrated across the film thickness h and the average velocities calculated according to Eq. (2.39). Using the compact notation of Eq. (2.41), the average velocities are equal to:

$$\bar{\boldsymbol{u}} = -\frac{\nabla p}{3\,\mu}\,h^2 + \frac{\boldsymbol{\tau_g}}{2\,\mu}\,h \tag{2.51}$$

Combining Eqs. (2.42) and (2.51) the governing lubrication equation can be obtained:

$$\frac{\partial h}{\partial t} = -\nabla\cdot\left(-\frac{\nabla p}{3\,\mu}\,h^3 + \frac{\boldsymbol{\tau_g}}{2\,\mu}\,h^2\right) \tag{2.52}$$

The pressure field is given by [11] as,

$$p = \rho\,g\,(h\,\cos\alpha - x\,\sin\alpha) - \sigma\,\nabla^2 h - \Pi \tag{2.53}$$

where:

- $\rho\,g\,(h\,\cos\alpha - x\,\sin\alpha)$ represents the contribution of hydrostatic pressure, x being the downhill direction of the plate.
- $\sigma\,\nabla^2 h$ is the capillary pressure, which is modeled by means of the small slope approximation according to Eq. (2.20).
- Π is the disjoining pressure, Eq. (2.21), which is related to the intermolecular forces between liquid and solid substrate.

Introducing the following non-dimensional quantities,

$$\begin{aligned}
&\tilde{h} = \frac{h}{h_\infty},\ \tilde{\boldsymbol{x}} = \frac{\boldsymbol{x}}{h_\infty},\ \tilde{t} = \frac{t}{(\mu\,h_\infty/\sigma)},\\
&\tilde{p} = \frac{p}{(\sigma/h_\infty)},\ \tilde{\Pi} = \frac{\Pi}{(\sigma/h_\infty)},\ \tilde{\boldsymbol{\tau}}_{\boldsymbol{g}} = \frac{\boldsymbol{\tau_g}}{(\mu\,u_\infty/h_\infty)}
\end{aligned} \tag{2.54}$$

defining the Bond number as the ratio between gravitational forces and surface tension forces,

$$\mathrm{Bo} = \frac{\rho\, g\, {h_\infty}^2}{\sigma} \tag{2.55}$$

and defining the capillary number as the ratio between viscous forces and surface tension forces,

$$\mathrm{Ca} = \frac{\mu\, u_\infty}{\sigma} \tag{2.56}$$

governing Eqs. (2.52) and (2.53) can be made dimensionless:

$$\frac{\partial \tilde{h}}{\partial \tilde{t}} = -\nabla \cdot \left(-\frac{\nabla \tilde{p}}{3}\, \tilde{h}^3 + \mathrm{Ca}\, \frac{\tilde{\boldsymbol{\tau}}_{\boldsymbol{g}}}{2}\, \tilde{h}^2 \right) \tag{2.57}$$

$$\tilde{p} = \mathrm{Bo}\, \left(\tilde{h}\, \cos\alpha - \tilde{x}\, \sin\alpha \right) - \nabla^2 \tilde{h} - \tilde{\Pi} \tag{2.58}$$

2.4 Analytical solutions

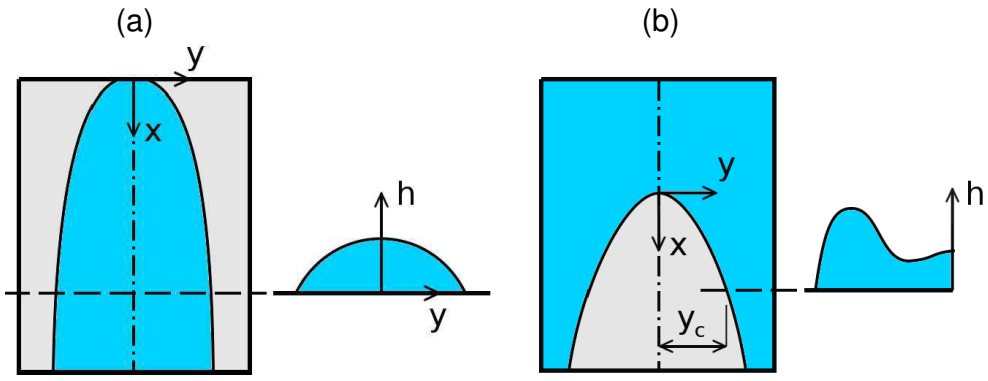

Figure 2.8: Stable rivulet flowing over a vertical plate (a), film breakup over an inclined plate (b)

A fully analytical solution of Eqs. (2.52) and (2.53) is not available, but in very simplified configurations.
The authors of [18] calculated the rivulet profile in the case of a stable rivulet flowing over a vertical plate, see figure 2.8(a), pushed by gravity and shear. Assuming that gravity and shear act along the same line, the physical problem is reduced to a 1D mathematical problem. Thus, the lubrication theory leads to the following set of equations,

$$p = -\sigma\, \frac{d^2 h}{dy^2} = \mathrm{const} \tag{2.59}$$

$$\dot{V} = \int_{-L_y}^{+L_y} \left(\frac{\rho\, g\, h^3}{3\, \mu} + \frac{\tau_g\, h^2}{2\, \mu} \right) dy \tag{2.60}$$

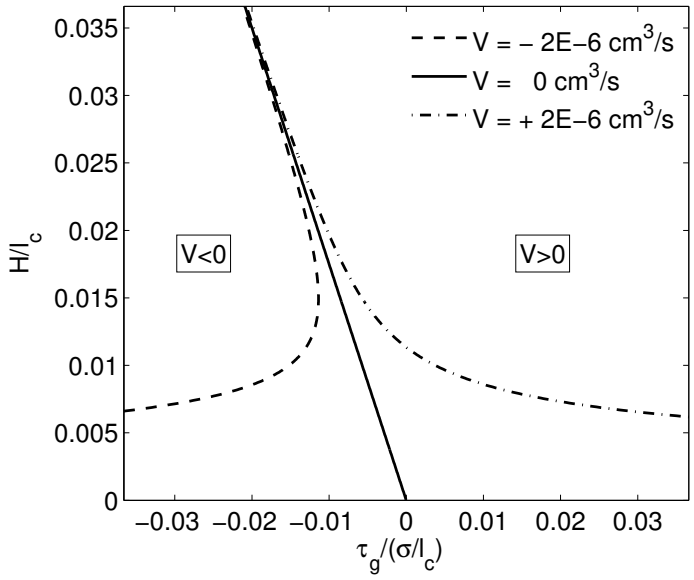

Figure 2.9: Possible rivulet configurations as a function of the external action of shear for fixed liquid flow rate, according to Eq. (2.62).

$\dot{V}$ being the volume flow rate flowing through the rivulet.
The following initial conditions are applied to $y = -L_y$,

$$h|_{-L_y} = 0, \left.\frac{dh}{dy}\right|_{-L_y} = \tan\theta_e \tag{2.61}$$

θ_e being the equilibrium contact angle.
Thus, the initial value problem defined by Eqs. (2.59) and (2.61) gives a parabolic profile of the free-surface. Eqs. (2.59), (2.60) and (2.62) can be solved by imposing the rivulet pressure p, resulting in a certain rivulet dimension, or the liquid flow rate $\dot{V}$. The resulting relation between liquid flow rate, rivulet dimension and shear stress states that,

$$\dot{V} = 4\,\tan\theta_e \left(\frac{16}{105}\,\frac{\rho\, g}{\mu}\,H^4 + \frac{4}{15}\,\frac{\tau_g}{\mu}\,H^3\right) \tag{2.62}$$

H being the maximum rivulet height.
Introducing the capillary length,

$$l_c = \sqrt{\frac{\sigma}{\rho\, g}} \tag{2.63}$$

the rivulet dimension H is made non-dimensional and plotted in figure 2.9 as a function of the external action of shear τ_g for fixed values of the liquid flow rate. It can be noticed that more rivulet configurations may be reached when shear and gravity act in opposite directions and the liquid flow is receding with respect to the plate downhill direction, i.e. $\tau_g < 0$ and $\dot{V} < 0$. Since only one of the two physical solutions is stable, the more probable configuration can be

determined by means of a stability analysis, [18].
An important result involving the dynamics of moving contact lines was obtained in [23] considering a 1D film flowing over an inclined plate. Such a problem is described by the following evolution equation,

$$\frac{\partial h}{\partial t} + \frac{\partial}{\partial x}\left(-\frac{\partial p}{\partial x}\frac{h^3}{3\,\mu}\right) = 0 \tag{2.64}$$

$$p = -\sigma\,\frac{\partial^2 h}{\partial x^2} - \rho\,g\,x \tag{2.65}$$

which can be obtained directly by Eqs. (2.52) and (2.53), neglecting the y partial derivatives and neglecting disjoining pressure contribution. Since surface wettability is not modeled, we are now considering the case of a superhydrophilic substrate (i.e. the imposed equilibrium contact angle is zero).
Assuming a precursor film in order to remove the moving contact line discontinuity, an *apparent* contact line, which is defined by the location of the interface maximum curvature, moves with a constant velocity u_c, defined by Eq. (2.31). Thus, considering a coordinate system that moves together with the contact line,

$$\hat{x} = x - u_c\,t \tag{2.66}$$

allows to solve the stationary shape of the moving interface.
Thanks to this change of variable, Eqs. (2.64) and (2.65) reduce to a single Ordinary Differential Equation,

$$-u_c\,\frac{dh}{d\hat{x}} + \frac{d}{d\hat{x}}\left(\frac{\sigma}{3\,\mu}\,\frac{d^3h}{d\hat{x}^3}\,h^3 + \frac{\rho\,g}{3\,\mu}\,h^3\right) = 0 \tag{2.67}$$

that can be integrated with the condition of flat film of thickness h_∞ at $\hat{x} = 0$, giving:

$$\left(\frac{\sigma}{3\,\mu}\,\frac{d^3h}{d\hat{x}^3} + \frac{\rho\,g}{3\,\mu}\right)\,h^2 = u_c\,\left(1 - \frac{h_\infty}{h}\right) \tag{2.68}$$

Defining the capillary number with respect to the undisturbed film velocity,

$$\mathrm{Ca} = \frac{\mu\,u_\infty}{\sigma} \tag{2.69}$$

the following dimensionless quantities,

$$\tilde{x} = \frac{\hat{x}}{h_\infty}\,\mathrm{Ca}^{\frac{1}{3}},\ \tilde{h} = \frac{h}{h_\infty},\ \tilde{\delta} = \frac{\delta}{h_\infty} \tag{2.70}$$

allows to reduce Eq. (2.68) to its general form:

$$\left(\frac{1}{3}\,\frac{d^3\tilde{h}}{d\tilde{x}^3} + 1\right)\,\tilde{h}^2 = \frac{1-\tilde{\delta}^3}{1-\tilde{\delta}}\,\left(1 - \frac{1}{\tilde{h}}\right) \tag{2.71}$$

It is important to point out that Eq. (2.68) with $\tilde{\delta} = 0$ (i.e. contact line singularity not removed) was first obtained in [10], which author studied the behavior of a bubble inside a capillary tube.

Solving numerically Eq. (2.71) with the proper boundary conditions allows to find the free-surface shape, revealing the existence of a capillary ridge surrounding the contact line, which is self-similar in time, accordingly to long scale evolution film problem. Since we are interested in contact line dynamics, an asymptotic approach can be adopted, looking for the local solution of h where the film thickness approaches the precursor film. In the region where $h \to \delta$, several terms of Eq. (2.71) that are small in the limit of small δ, can be neglected, leading to:

$$\tilde{h}^2 \frac{d^3\tilde{h}}{d\tilde{x}^3} = 3\left(1 - \frac{\tilde{\delta}}{\tilde{h}}\right) \tag{2.72}$$

Solution of Eq. (2.72) has the following asymptotic behavior,

$$\tilde{h}(\tilde{x}) \sim (\tilde{x}_0 - \tilde{x})\left[\log\left(\frac{\tilde{x}_0 - \tilde{x}}{\tilde{\delta}}\right)\right]^{1/3} \text{ at } \frac{\tilde{x}_0 - \tilde{x}}{\tilde{\delta}} \to +\infty \tag{2.73}$$

$\tilde{x}_0$ being an arbitrary point in the apparent contact line region. Thus, the free-surface slope is known in the apparent contact line region, allowing to calculate the so-called dynamic (or apparent) contact angle θ, which is defined by the absolute value of the interface slope angle at a distance l so that $\delta < l < h_\infty \, \mathrm{Ca}^{1/3}$, as:

$$\theta = \mathrm{Ca}^{1/3}\left[3\log\left(\frac{l\,\mathrm{Ca}^{1/3}}{h_\infty\,\tilde{\delta}}\right)\right]^{1/3} \tag{2.74}$$

Since the influence of the factor $\mathrm{Ca}^{1/3}$ in the logarithmic term is not so important and using the definitions of capillary number and contact line velocity, Eq. (2.74) can be reduced to:

$$\theta^3 \propto \frac{\mu\, u_c}{\sigma} \tag{2.75}$$

Eq. (2.75) predicts the dynamic contact angle, which can be observed close to the apparent contact line, when a liquid front is flowing over a perfectly wettable solid substrate. A more general equation, i.e. the Tanner-Hoffman-Voinov formula, Eq. (2.30), can be used to predict the effective contact angle along the apparent contact line when a non-wettable surface is involved (i.e. non-zero equilibrium contact angle is imposed, $\theta_e > 0$).
In [26] the authors solved the 2D lubrication equation for a film flowing down an inclined plate with a semi-analytical approach, looking for the evolution of a possible dry-patch. The investigated problem is described by figure 2.8(b). Considering steady state condition, assuming that capillary forces drive the wetting process and applying the following simplifications to the lubrication theory,

- free-surface curvature along plate downhill direction x negligible, leading to $2\,\kappa_m \simeq \frac{\partial^2 h}{\partial y^2}$, and mainly varying with y, i.e. $\frac{\partial}{\partial x}\left(\frac{\partial^2 h}{\partial y^2}\right) \simeq 0$;
- surface wettability not modeled (i.e. disjoining pressure is neglected);

- hydrostatic pressure $\rho\, g\, h\, \cos\alpha$ neglected;

Eqs. (2.52) and (2.53) were approximated by:

$$\frac{\partial}{\partial y}\left[\frac{\partial}{\partial y}\left(-\sigma\,\frac{\partial^2 h}{\partial y^2}\right)\,h^3\right]-\rho\, g\,\sin\alpha\,\frac{\partial}{\partial x}\left(h^3\right)=0 \tag{2.76}$$

Assuming that a stable dry-patch exists over the plate, the authors seek a similarity solution in the form:

$$h=f(x)\,G(\eta),\;\eta=y/y_c(x) \tag{2.77}$$

y_c being the contact line of the dry-patch.
Choosing the following solutions family,

$$f=b\;(c\,x)^m\,,\;y_c=(c\,x)^n \tag{2.78}$$

substituting to Eq. (2.76), the following differential equation was obtained in [26]:

$$\frac{d}{d\eta}\left[\left(\frac{d^3G}{d\eta^3}-\eta\right)\,G^3\right]+\left(13-\frac{3}{n}\right)\,G^3=0 \tag{2.79}$$

Since an analytical solution of Eq. (2.79) is not available, the authors adopted a numerical approach and, applying proper boundary conditions, they obtained the free-surface profile over the domain. According to experimental evidences, a ridge surrounding the contact line was observed, while a quartic profile ($n=1/4$) was obtained for the contact line imposing a constant liquid flux around the dry-patch:

$$Q(x)=\frac{\rho\, g\,\sin\alpha}{3\,\mu}\lim_{y\to\infty}\frac{1}{y}\int_{y_c(x)}^{y}h^3\,dy^*=\text{const} \tag{2.80}$$

It is important to remark that no contact angle was imposed by the authors, thus they did not take into account of the surface wettability.
Following the same approach, Duffy and Moffatt [4] solved Eq. (2.76) in the case of a steady rivulet over a nearly vertical plate, test case of figure 2.8(a), with the aim of understanding the liquid behavior in the hydrodynamic entrance region. In fact, the liquid enters the domain through a narrow inlet section at the top of the plate and spreads over the domain, approaching the shape of a stable rivulet. Seeking for a similarity solution of the same form as Eq. (2.77), it was found that,

$$f=b\;(c\,x)^{-\frac{1}{13}}\,,\;y_c=(c\,x)^{\frac{3}{13}} \tag{2.81}$$

$$G=\left(\eta^4-1\right)-\lambda\,\left(\eta^2-1\right) \tag{2.82}$$

with,

$$b=c\,\frac{\rho\, g\,\sin\alpha}{104\,\sigma} \tag{2.83}$$

$$c^3\,P(\lambda)=\frac{3690960\,\sigma^3\,\mu}{\left(\rho\, g\,\sin\alpha\right)^4}\,\dot{V} \tag{2.84}$$

$$P(\lambda)=\lambda^3-\frac{10}{3}\lambda^2+\frac{124}{33}\lambda-\frac{56}{39} \tag{2.85}$$

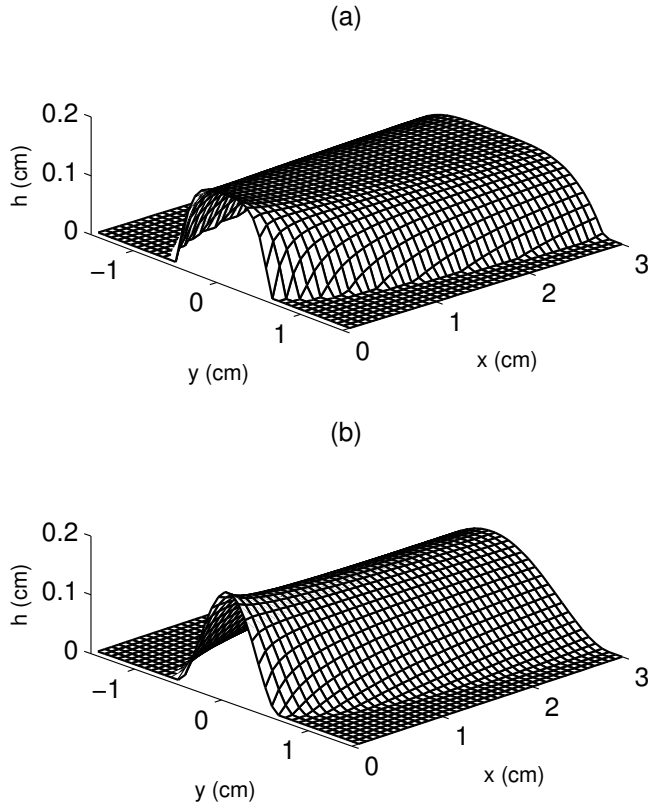

Figure 2.10: Free-surface shape predicted by similarity solution, Eqs. (2.81) and (2.82) in the case of: $\lambda = 0$, (a); $\lambda = 2$, (b). $\rho = 981.3\,\mathrm{kg/m^3}$, $\mu = 0.03642\,\mathrm{Pa\,s}$, $\sigma = 0.0384\,\mathrm{N/m}$, $\alpha = 30°$, $Q = 10^{-6}\,\mathrm{m^3/s}$.

$\dot{V}$ being the liquid volume flux imposed through the rivulet.
Figures 2.10(a) and 2.10(b) show the stationary liquid layer distribution over the inclined plate for two different values of the parameter λ, according to Eqs. (2.81) and (2.82), with the liquid properties belonging to an high viscosity liquid used as a solvent in the context of CO_2 absorption (1-methylepiperazine $0.31x$MPZ). It is important to notice that the imposed free parameter λ strongly influences the solution. Physical interpretations of the possible rivulet shapes are given in [4].
Again, the contact angle was not imposed, its value varying along the contact line. Thus, the surface wettability is not accounted in the model of [4], making its application not useful for real problems.

2.5 Numerical approach

A number of literature works deals with the numerical solution of the fourth-order nonlinear partial differential equation describing the evolution of a thin film, given by Eqs. (2.52) and (2.53), with a particular attention paid on the numerical scheme to be used. Such an interest is justified by the very

restrictive stability constraint on the time-step for explicit methods. This can be understood considering the linearized 1D governing lubrication equation in its non-dimensional form:

$$\frac{\partial \tilde{h}}{\partial \tilde{t}} = -\frac{1}{3}\frac{\partial^4 \tilde{h}}{\partial \tilde{x}^4} \tag{2.86}$$

In the context of finite difference method, discretizing the fourth-order spatial derivative by means of a second order centered scheme and marching in time with explicit Euler, the Von Neumann stability analysis leads to the following constraint in order to ensure convergence of the solution:

$$\Delta\tilde{t} \leq \frac{1}{3}\Delta\tilde{x}^4 \tag{2.87}$$

The dimensional time step deriving from the stability condition can be easily obtained substituting in Eq. (2.87) the definitions of Eq. (2.54):

$$\Delta t = \frac{\mu}{\sigma\, {h_\infty}^3}\Delta x^4 \tag{2.88}$$

It clearly comes that an explicit integration is not computationally feasible when high resolution (i.e. low spatial discretization step, $\Delta\tilde{x} < 1$) is required. In fact, an implicit approach is always adopted in the available literature work, allowing for a strong reduction of computational cost thanks to the high integration time-step that can be imposed ensuring convergence. A straightforward implementation of an implicit scheme would lead to a sparse system of nonlinear algebraic equations to be solved at each time step, which can be still expensive. However, the computational time can be greatly reduced following an alternate direction implicit (ADI) scheme if the domain (the inclined plate) is discretized with a structured grid. A great effort was put by [13], who proposed an efficient ADI method for solving the following equations family:

$$\frac{\partial \Phi}{\partial t} + \nabla \cdot \left(f(\Phi)\, \nabla\nabla^2\Phi \right) = 0 \tag{2.89}$$

Φ, f being the unknown field variable and a nonlinear function of Φ.
Before showing the procedure proposed in [13], it is worth to define the linear operators $\boldsymbol{L}_{x,y}$ and the differential operators $\boldsymbol{D}_{x,y}$,

$$\boldsymbol{L}_x = \boldsymbol{I} + \Theta\,\Delta t\,\boldsymbol{D}_x,\ \boldsymbol{L}_y = \boldsymbol{I} + \Theta\,\Delta t\,\boldsymbol{D}_y \tag{2.90}$$

$$\boldsymbol{D}_x = \partial_x\left[f\left(\tilde{\Phi}^{n+1}\right)\partial_{xxx}\right],\ \boldsymbol{D}_y = \partial_y\left[f\left(\tilde{\Phi}^{n+1}\right)\partial_{yyy}\right] \tag{2.91}$$

$\boldsymbol{I}$ being the identity operator, Θ being the coefficient of the one-step generalized trapezoid rule and $\tilde{\Phi}^{n+1}$ being the guessed value of the unknown variable at the unknown time step $n+1$.
The following pseudo-linear factorization was proposed in [13],

$$\boldsymbol{L}_x\boldsymbol{L}_y\,\Delta\Phi = -\left(\tilde{\Phi}^{n+1} - \Phi^n\right) - \Delta t\,\nabla\cdot\left(f\left(\tilde{\Phi}^{n+1}\right)\nabla\nabla^2\tilde{\Phi}^{n+1}\right) \tag{2.92}$$

with $\Delta\Phi \sim \Phi^{n+1} - \tilde{\Phi}^{n+1}$.
The ADI split equations for this backward Euler scheme are then:

$$\boldsymbol{L}_x \Delta\Phi^* = -\left(\tilde{\Phi}^{n+1} - \Phi^n\right) - \Delta t\, \nabla \cdot \left(f\left(\tilde{\Phi}^{n+1}\right) \nabla\nabla^2 \tilde{\Phi}^{n+1}\right) \tag{2.93}$$

$$\boldsymbol{L}_y \Delta\Phi = \Delta\Phi^* \tag{2.94}$$

$$\Phi^{n+1} \sim \tilde{\Phi}^{n+1} + \Delta\Phi \tag{2.95}$$

Eq. (2.92) reveals that, apart the adopted ADI approximate factorization, an iterative method is applied by authors of [13], that named this numerical scheme as *iterative factorized method*. In fact the solution of the two split algebraic systems, Eqs. (2.93) and (2.94), is iterated at each time-step until $\tilde{\Phi}^{n+1}$ converges to Φ^{n+1}. However, the goal of such a method is that the mixed derivatives of Φ,

$$\frac{\partial}{\partial x}\left(f(\Phi)\,\frac{\partial^3\Phi}{\partial x \partial y^2}\right),\ \frac{\partial}{\partial y}\left(f(\Phi)\,\frac{\partial^3\Phi}{\partial y \partial x^2}\right) \tag{2.96}$$

are treated explicitly as well as the nonlinear prefactor $f(\Phi)$, allowing to decompose the sparse matrix into two linear, pentadiagonal matrices, Eqs. (2.93) and (2.94), that are computationally cheaper to solve.
The authors also demonstrated that this iterative method allows to reach second order accuracy in time, that would be otherwise impossible with one-step ADI methods involving mixed derivatives, while its efficiency is guaranteed by integration time-steps up to 10^8 the explicit one.
A similar approach was also adopted in [11, 27], which authors solved numerically the governing lubrication equation, also revealing a gain on Δt of about 10^8 the explicit one, during periods of slow shape evolution, when a fine mesh is used.
In the context of finite difference method, the authors of [13] discretized the domain with an uniform grid and adopted a centered scheme for space discretization. Thus, for the i, j-th node of the computational grid it comes that:

- The term $\nabla^2\Phi$ of Eq. (2.89) is discretized via a second order accurate centered difference:

$$\left.\frac{\partial^2\Phi}{\partial x^2}\right|_{i,j} \simeq \frac{\Phi_{i+1,j} - 2\,\Phi_{i,j} + \Phi_{i-1,j}}{\Delta x^2} \tag{2.97}$$

- Calling $\boldsymbol{Q} = (q,\, s)^T = f(\Phi)\,\nabla\nabla^2\Phi$, the term $\nabla\boldsymbol{Q}$ of Eq. (2.89) is also treated by means of a second order centered scheme,

$$\left.\frac{\partial q}{\partial x}\right|_{i,j} \simeq \frac{q_{i+\frac{1}{2},j} - q_{i-\frac{1}{2},j}}{\Delta x} \tag{2.98}$$

  the nonlinear prefactor being computed through a trapezoidal average:

$$f_{i+\frac{1}{2},j} = f\left(\frac{\Phi_{i,j} + \Phi_{i+1,j}}{2}\right) \tag{2.99}$$

In [14], the following nonlinear 4-th order PDE is numerically solved,

$$\frac{\partial \Phi}{\partial t} = -\nabla \cdot \left[C\,\Phi^3\,\nabla\nabla^2\Phi - G\,\Phi^3\nabla\Phi + F\,\Phi^3 \right] \tag{2.100}$$

C, G, F being constant coefficients.
Note that Eq. (2.100) is analogous to Eqs. (2.52) and (2.53), when zero shear and zero equilibrium contact angle are imposed. Again, a second order centered scheme is used in [14] for discretizing in space Eq. (2.100). Thus, Eqs. (2.97) and (2.98) are still applied, $\boldsymbol{Q}$ being defined as,

$$\boldsymbol{Q} = C\,f_C\,\nabla\nabla^2\Phi - G\,f_G\,\nabla\Phi + F\,f_F\,\Phi \tag{2.101}$$

with $f_{C,G} = \Phi^3$, $f_F = \Phi^2$.
The nonlinear prefactors are discretized as:

$$f_{C\,i+\frac{1}{2},j} = 2\,\frac{{\Phi_{i,j}}^2 \Phi_{i+1,j}{}^2}{\Phi_{i,j} + \Phi_{i+1,j}} \tag{2.102}$$

$$f_{G\,i+\frac{1}{2},j} = \frac{{\Phi_{i,j}}^3 + \Phi_{i+1,j}{}^3}{2} \tag{2.103}$$

$$f_{F\,i+\frac{1}{2},j} = \frac{{\Phi_{i,j}}^2 + \Phi_{i+1,j}{}^2}{2} \tag{2.104}$$

It can be noticed that the nonlinear prefactor f_C, that multiplies the higher order derivative of h, is treated as a diffusivity term, while different schemes are used for $f_{G,F}$, revealing a more accurate spatial discretization than the one proposed in [13]. Moreover, the governing equation is solved on a structured, but non uniform computational grid.
The numerical investigations concerning 2D thin liquid layer spreading over a plate mainly involve the simulation of:

- drop spreading over an hydrophilic surface with both constant non-zero contact angle or variable contact angle accordingly to a textured grid, [11];
- drop coalescence [14, 28], wetting and de-wetting dynamics, [13];
- finger instabilities occurring when a film flows over an inclined plate: in [15] the instability is induced by means of a texture including strips of different contact angle;
- dry-patch generation due to solid occlusion perturbing the undisturbed flow [3];
- particle-laden thin film flows [22].

Other numerical studies on evolution of thin layer of liquid are available in literature. It is worth to point out that in one recent paper [3] a commercial software using a Finite Element solver was used for numerically solving the governing lubrication equation in case of a film flowing over a vertical plate.

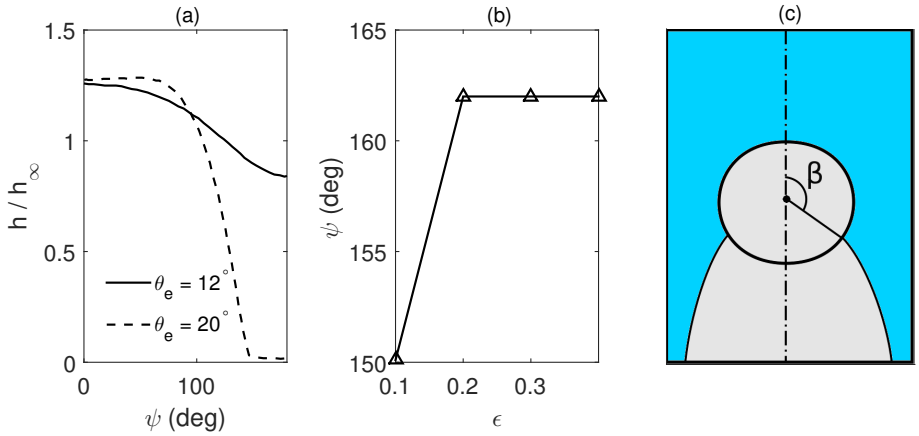

Figure 2.11: Numerical results of [3]: film thickness distribution on the cylindrical occlusion for $\epsilon = 0.2$ (a); separation angle as a function of ϵ for $\theta_e = 20°$ (b). Coordinate β defining the position along the obstacle perimeter (c).

But the authors mainly focused on the liquid behavior of a thin film around a solid occlusion, with the aim of investigating the effect of the obstacle shape and wettability.
In figure 2.11(a), the liquid distribution along the contour of the cylindrical occlusion, which is identified by the angle β, is plotted for two different values of the equilibrium contact angle between liquid and solid substrate, while the contact angle on the occlusion was fixed to the constant value of 90° by the author of [3]. Figure 2.11(b) focuses on the position along the occlusion contour at which film separation occurs. The parameter ϵ,

$$\epsilon = \left(\frac{\rho\, g\, {h_\infty}^2}{\sigma} \right)^{1/3} \tag{2.105}$$

is used in [3] in order to define the undisturbed flow characteristics.

2.6 Modelling of inertial effect

As mentioned, the proposed governing equation, Eq. (2.52), is valid for low values of the Reynolds number, $\mathrm{Re} = \rho\, u_\infty\, h_\infty / \mu \leq 1$. Thus, its application is limited to the case of negligible inertial effects, that mainly occurs when high viscosity liquids are considered. However, the lubrication theory is still valid for higher values of the Reynolds number. Even if such a case is not investigated in this work, a theoretical model, which is an extension of the classical Bretherton theory [10], is presented, since it finds application in some engineering problems [29,30]. However, the full 2D governing equations in case of non-negligible liquid inertia, $\mathrm{Re} >> 1$, are not derived.
The authors of [30] adopted a model accounting for liquid inertia, with the aim of understanding the undulation appearing on the free-surface of long bubbles in confined liquid-gas flow. Assuming that the problem is assialsymmetric and that the bubble shape and velocity keep constant in time and choosing

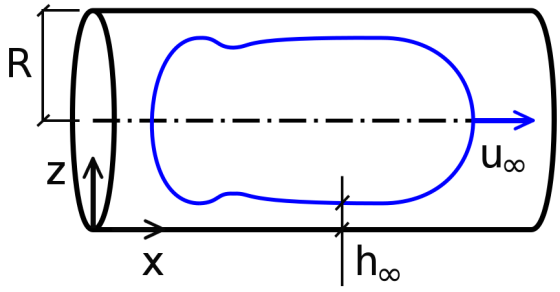

Figure 2.12: Sketch of a confined elongated bubble flowing inside a circular duct.

a Cartesian coordinate system moving within the bubble, see figure 2.12, the momentum equation along the main flow direction can be written as,

$$\rho \left(u \frac{\partial u}{\partial x} + w \frac{\partial u}{\partial z} \right) + \frac{\partial p}{\partial x} = \mu \frac{\partial^2 u}{\partial z^2} \tag{2.106}$$

the pressure being equal to the capillary contribute, $p = -\sigma \kappa_m$, x and z being the flow direction and the solid substrate outward direction respectively.
Applying the lubrication theory, Eq. (2.106) can be integrated across the film thickness:

$$\rho \left(\int_0^h u \frac{\partial u}{\partial x} dz + \int_0^h w \frac{\partial u}{\partial z} dz \right) = \int_0^h \sigma \frac{\partial \kappa_m}{\partial x} dz + \int_0^h \mu \frac{\partial^2 u}{\partial z^2} dz \tag{2.107}$$

Assuming that the velocity profile remains parabolic (as it happens when liquid inertia is neglected) allows to write u as,

$$u = 3 F(x) \left[-\frac{z}{h} + \frac{1}{2} \left(\frac{z}{h} \right)^2 \right] - u_\infty \tag{2.108}$$

where $F(x)$ can be derived imposing the film flux,

$$F(x) = u_\infty \left(\frac{h_\infty}{h} - 1 \right) \tag{2.109}$$

u_∞ and h_∞ being the bubble velocity and the undisturbed liquid thickness respectively.
Substituting the velocity profile in the integrated momentum equation and applying some algebraic manipulations, the following governing ordinary differential equation can be obtained:

$$\sigma \frac{d^3 h}{dx^3} = 3 \mu u_\infty \frac{h - h_\infty}{h^3} + \frac{1}{5} \rho {u_\infty}^2 \frac{h^2 - 6 {h_\infty}^2}{h^3} \frac{dh}{dx} \tag{2.110}$$

Eq. (2.110) can be made dimensionless,

$$\frac{d^3 \tilde{h}}{d\tilde{x}^3} = 3 \frac{\tilde{h} - 1}{\tilde{h}^3} + \frac{1}{5} \mathrm{Re}\, \mathrm{Ca}^{\frac{1}{3}} \frac{\tilde{h}^2 - 6}{\tilde{h}^3} \frac{d\tilde{h}}{d\tilde{x}} \tag{2.111}$$

with:

$$\tilde{x} = \frac{x}{h_\infty}\,\mathrm{Ca}^{1/3},\ \tilde{h} = \frac{h}{h_\infty},\ \mathrm{Ca} = \frac{\mu\, u_\infty}{\sigma},\ \mathrm{Re} = \frac{\rho\, u_\infty\, h_\infty}{\mu} \tag{2.112}$$

Eq. (2.111) can be compared with the the governing equation obtained by Bretherton [10] for the same test case but neglecting liquid inertia,

$$\frac{d^3\tilde{h}}{d\tilde{x}^3} = 3\,\frac{\tilde{h}-1}{\tilde{h}^3} \tag{2.113}$$

revealing that an additional term modeling the liquid inertia is added to the classical lubrication equation.
A similar approach was adopted in [29], which authors studied the thin film flow inside a stationary circular cylinder driven by an imposed shear stress. For a better modeling of inertia effect, both a parabolic and a cubic velocity profiles, the choice depending on the magnitude of Reynolds number, were adopted by the authors.

2.7 Diffuse interface theory of thin films

The existence of a sharp interface separating liquid and gas phases was assumed for the derivation of the governing lubrication equations, Eqs. (2.52) and (2.53). However, any interphase boundary is essentially a mesoscopic structure, with the properties of the involved fluids varying steeply along interface normal direction, approaching a molecular scale, as stated in [31]. The contradictions between the necessity of describing thin film dynamics by a macroscopic point of view and the effective mesoscale governing interface phenomena leads to the singularity of three-phase moving contact lines, as mentioned when introducing disjoining pressure. The assumption of a precursor film rather than the imposition of a proper wall slip condition in order to solve such a singularity was introduced in section 2.2.2. Even if the disjoining pressure model, Eq. (2.21), represents a rational formulation of the sharp interface model, it does not provide the real physics behind moving contact lines, since the singularity is solved adding a small scale attractive force between liquid and solid substrate to the canonical disjoining term (liquid-solid repulsion), leading to a stable wetting layer, the above mentioned precursor film. On the other side, abandoning continuum approach in favor of molecular dynamics simulations is not feasible in terms of computational cost. A great effort was put by the author of [31], who started from van der Waals theory to compute the density profile across a diffuse interface separating liquid phase and gas phase of a given fluid, to be used in the continuum theory of thin liquid films, i.e. Navier-Stokes equations, and verified that the governing lubrication equation, Eq. (2.52), derived under sharp interface assumption, represents the asymptotic limit of diffuse interface theory.
Consider a one-component van der Waals fluid. Let T and $\rho = N/V$ be its temperature and number density, N being the number of particles inside

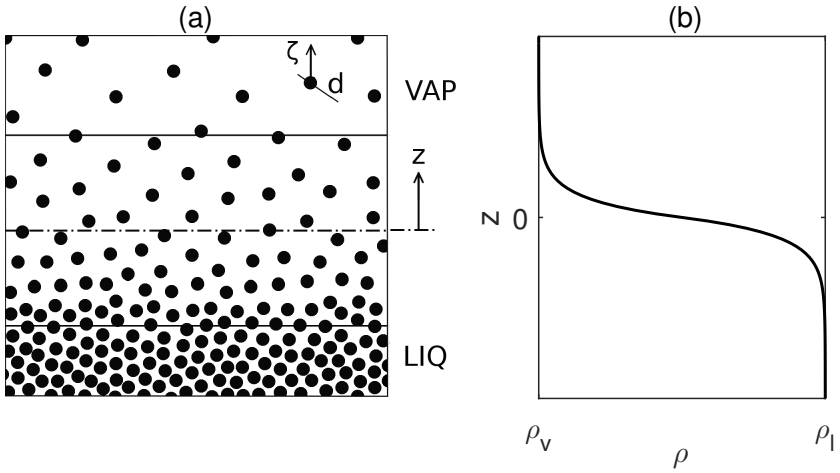

Figure 2.13: Diffuse interface separating liquid phase and vapor phase of a given fluid (a). Density profile across liquid-vapor interface (b).

volume V. Further on, consider an isothermal process, thus $T = \text{const}$, while let ρ vary in space. Referring to a flat diffuse interface separating liquid-gas phases, as shown in figure 2.13(a), with the fluid properties varying along interface normal direction, we can reconduce to a 1D problem. Coordinate z identifying the position of each particle of fluid and ζ being the relative distance across interface normal from the particle centroid at z, the local Helmotz free energy per molecule is given by,

$$f(z) = \bar{f}\left(\rho(z)\right) + \frac{1}{2}\int_{|\zeta|>d} U(\zeta)\ \left[\rho(z+\zeta) - \rho(z)\right]\ d\zeta \tag{2.114}$$

where:

- d is the nominal hard-core molecule diameter;
- $\bar{f}(\rho)$ is the free energy of a homogeneous state [31],

$$\bar{f}(\rho) = T\ \log\left(\frac{\rho}{1 - \frac{2}{3}\pi d^3\,\rho}\right) - \frac{2\,\pi\,A_l}{3\,d^3}\,\rho \tag{2.115}$$

  with A_l being a constant;

- $U(\zeta)$, which is needed to compute the distortion energy due to change of density in space, is the interaction kernel [31]:

$$U(\zeta) = -\frac{1}{2}\,\pi\,A_l\,\zeta^{-4} \text{ at } |\zeta| > d \tag{2.116}$$

The total free energy per unit area (obtained by integration of local free energy per unit molecule in the 1D space) must be minimized, looking for the most suitable energetic configuration, under the constraint of fixed number of

particles (i.e. mass conservation),

$$\begin{aligned}\mathcal{F} &= \int_{-\infty}^{+\infty} \rho(z)\, f(z)\, dz - G \\ &= \int_{-\infty}^{+\infty} \rho(z) \left[\bar{f}\,(\rho(z)) - \hat{G}\right]\, dz \\ &+ \frac{1}{2}\int_{-\infty}^{+\infty} \rho(z)\, dz \int_{|\zeta|>d} U(\zeta)\left[\rho(z+\zeta) - \rho(z)\right]\, d\zeta\end{aligned} \tag{2.117}$$

where G is the Gibbs free energy and $\hat{G} = G/N$ is the corresponding chemical potential, which forces mass conservation acting as a Lagrangian multiplier. Minimizing the integral $\mathcal{F}$ gives the unknown density profile $\rho(z)$ and the chemical potential $\hat{G}$. Thus, RHS of Eq. (2.117) can be derived in ρ and equalized to zero as shown in [31], leading to the corresponding 1D Euler-Lagrange equation,

$$\frac{2\,\pi\, A_l}{3\, d}\,\frac{d^2\rho}{dz^2} - \lambda(\rho) + \hat{G} = 0 \tag{2.118}$$

$$\lambda(\rho) = \frac{d}{d\rho}\left[\rho\, \bar{f}(\rho)\right] \tag{2.119}$$

which solution gives the unknown density profile $\rho(z)$.
As shown in figure 2.13(b), fluid density varies between ρ_l and ρ_v, which are the corresponding liquid and vapor densities. Once the density profile and the chemical potential are computed, the surface tension σ, which is a free energy per unit area, can be calculated through Eq. (2.117) as the corresponding value of the optimized quantity $\mathcal{F}$.

2.7.1 Chemical potential of a thin film

When a thin film flows over a flat solid substrate, the total chemical potential can be defined as [31],

$$\hat{G} = \hat{G}_s - \frac{1}{\rho_l - \rho_v}\,\sigma\,\nabla^2 h \tag{2.120}$$

$\hat{G}_s$ being the disjoining potential, h being the thickness of a reference iso-density line ($\rho = \text{const}$) and $\nabla^2 h$ defining the interface curvature under small slope approximation.
The disjoining potential, which arises in the proximity of a solid surface, is connected with the interaction between the fluid and the solid substrate. The following expression of $\hat{G}_s$ is given in [31],

$$\hat{G}_s = -C_H\,\rho_l\,\frac{\pi\, A_l}{6\, h^3} - \frac{\rho_l}{2\,\lambda'(\rho_l)}\left(\frac{\pi\, A_l}{6\, h^3}\right)^2 \tag{2.121}$$

with C_H being the dimensionless Hamaker constant, which depends on liquid and solid properties, and λ' being equal to:

$$\lambda'(\rho_l) = \frac{d}{dh}\left[\lambda(\rho_l)\right] \tag{2.122}$$

When a sharp interface is assumed, it can be demonstrated that $\lambda'(\rho_l) \to -\infty$, thus the second term in RHS of Eq. (2.121) vanishes, and the disjoining potential reduces to:

$$\hat{G}_s^{s.i.} = -C_H \, \rho_l \, \frac{\pi \, A_l}{6 \, h^3} \tag{2.123}$$

The film thickness h_0 leading to $\hat{G}_s = 0$ corresponds to the reference interface position on a dry surface in equilibrium with the bulk liquid [31]. Note that such an equilibrium configuration can not be reached when a sharp interface is assumed, unless a liquid-solid attractive term is added leading to a stable precursor film, as done in [11] when introducing disjoining pressure.

2.7.2 Evolution equation for thin film

The governing equations describing the evolution of a thin liquid layer over a flat substrate are still derived in [31] from Navier-Stokes equations, assuming lubrication approximation. However, a non-uniform fluid density across substrate normal direction is assumed due to diffuse interface: the density profile $\rho(z-h)$, obtained via the solution of Eqs. (2.118) and (2.119), must be considered. Thus, the momentum equation leads to,

$$\rho(z-h) \, \nabla \hat{G} = \frac{d}{dz} \left(\mu \, \frac{d\boldsymbol{u}}{dz} \right) \tag{2.124}$$

$\hat{G}$ being the driving potential, defined by Eq. (2.121), and the dynamic viscosity μ depending on the coordinate z as well as the density.
Imposing no-slip condition at the solid substrate and no-stress at infinity, leads to the general solution given in [31]:

$$\boldsymbol{u} = \nabla \hat{G} \int_0^z \frac{d\zeta}{\mu(\zeta)} \int_\zeta^\infty \rho(\xi - h) \, d\xi = \Psi(z,h) \, \nabla \hat{G} \tag{2.125}$$

Writing the integral mass balance across the fluid layer within the mean density and the mean velocity deriving from the known density and velocity profiles, the following evolution equation can be obtained,

$$\frac{\partial h}{\partial t} = \nabla \cdot \left[K(h) \, \nabla \hat{G} \right] \tag{2.126}$$

h being the reference film thickness and $K(h)$ being the mobility factor [31]:

$$K(h) = \int_0^\infty \rho(z-h) \, \Psi(z,h) \, dz \tag{2.127}$$

As a final remark, it is important to notice that Eq. (2.126) has the structure of a standard equation of motion of thin liquid films. In fact, imposing the asymptotic case of a sharp interface (i.e. constant density $\rho \equiv \rho_l$ across the film thickness) the mobility factor becomes,

$$K(h) = \frac{\rho_l \, h^3}{3 \, \mu_l} \tag{2.128}$$

allowing to reduce velocity profile, Eq. (2.125), to the well known Poiseuille flow. Thus, the thin film evolution equation, Eq. (2.126), which models the liquid-vapor interface as a diffuse interface, becomes,

$$\frac{\partial h}{\partial t} + \nabla \cdot \left[C_\sigma \, h^3 \, \nabla \nabla^2 h + C_s \, h^3 \, \nabla \left(\frac{1}{h^3} \right) \right] = 0 \tag{2.129}$$

$$C_\sigma = \frac{\sigma}{3\,\mu_l} \frac{\rho_l}{\rho_l - \rho_v} \simeq \frac{\sigma}{3\,\mu_l} \tag{2.130}$$

$$C_s = \frac{C_H \, \rho_l^2}{3\,\mu_l} \frac{\pi \, A_l}{6} \tag{2.131}$$

which can be directly reconduced to Eqs. (2.52) and (2.53) if hydrostatic pressure and shear applied by the vapor phase at the interface are neglected. It can be stated that the classical lubrication equation modeling the thin liquid layer evolution (derived under the implicit assumption of sharp interface) simply represents the asymptotic limit of the diffuse interface theory of thin films, that has the merit of modeling the whole physics behind moving contact lines.

Chapter 3

Thin film breakup on hydrophilic surfaces

The dimensionless equations governing the evolution of a thin layer of liquid over an inclined plate pushed by gravity and shear of an external gas flow assuming lubrication approximation, Eqs. (2.52) and (2.53), derived in chapter 2, are again proposed,

$$\frac{\partial \tilde{h}}{\partial \tilde{t}} = -\nabla \cdot \tilde{\boldsymbol{Q}} = -\nabla \cdot \left(-\frac{\nabla \tilde{p}}{3}\, \tilde{h}^3 + \mathrm{Ca}\, \frac{\tilde{\boldsymbol{\tau}}_{\boldsymbol{g}}}{2}\, \tilde{h}^2 \right) \tag{3.1}$$

$$\tilde{p} = \mathrm{Bo} \left(\tilde{h}\, \cos\alpha - \tilde{x}\, \sin\alpha \right) - \nabla^2 \tilde{h} - \tilde{\Pi} \tag{3.2}$$

$$\tilde{\Pi} = B \left[\left(\frac{\tilde{\delta}}{\tilde{h}} \right)^n - \left(\frac{\tilde{\delta}}{\tilde{h}} \right)^m \right] \tag{3.3}$$

$$B = f\, \frac{(n-1)\,(m-1)}{2\,(n-m)}\, \frac{\tan^2 \theta_e}{\tilde{\delta}} \tag{3.4}$$

$$f = 1 + 6.069\, \tilde{\delta} + 161.7\, \tilde{\delta}^2 - 1547\, \tilde{\delta}^3 + 5890\, \tilde{\delta}^4 \tag{3.5}$$

with:

$$\tilde{h} = \frac{h}{h_\infty},\ \tilde{\boldsymbol{x}} = \frac{\boldsymbol{x}}{h_\infty},\ \tilde{t} = \frac{t}{(\mu\, h_\infty/\sigma)},\ \tilde{\boldsymbol{Q}} = \frac{\boldsymbol{Q}}{(\sigma\, h_\infty)\,/\mu} \tag{3.6}$$

$$\tilde{p} = \frac{p}{(\sigma/h_\infty)},\ \tilde{\Pi} = \frac{\Pi}{(\sigma/h_\infty)},\ \tilde{\boldsymbol{\tau}}_{\boldsymbol{g}} = \frac{\boldsymbol{\tau}_{\boldsymbol{g}}}{\mu\, u_\infty/h_\infty} \tag{3.7}$$

$$\mathrm{Bo} = \frac{\rho\, g\, {h_\infty}^2}{\sigma},\ \mathrm{Ca} = \frac{\mu\, u_\infty}{\sigma} \tag{3.8}$$

Eqs. (3.1) and (3.2) are solved numerically by means of an in-house Finite Volume Method (FVM) solver, which was developed using `FORTRAN` programming language.

After a proper validation of the code, the critical flow condition of a gravity driven film leading to film breakup is investigated and the dynamic contact angle is computed over the contact line of the generated dry-patch. Triggering the flow rate that leads to the generation of a stable dry-patch, i.e. the dry-patch will not shed away, is an interesting issue, involved in several engineering applications. In fact, a large literature [2, 8, 9, 17, 19] trying to understand the wetting dynamics of a liquid film over an inclined plate is available.

3.1 Spatial discretization

The 2D spatial domain $L_x \times L_y$ is discretized using a structured, orthogonal grid composed by $n_{el} = n_i \times n_j$ elements of variable dimensions.
Eq. (3.1) is usually discretized in the available literature [11,13,14,22,27] using a centered scheme, as explained in chapter 2.5. This is obviously possible thanks to the capillary pressure gradient, which generates an high diffusive term. However, the lubrication equation comes from a mass balance and it is similar to a 2D continuity equation,

$$\frac{\partial h}{\partial t} + \nabla \cdot (\bar{\boldsymbol{u}}\, h) = 0 \tag{3.9}$$

with the film thickness acting as a non-uniform density. Thus, Eq. (3.1) can also be solved by means of an upwind scheme, keeping a touch with the physics behind the mathematical model. Since Eq. (3.1) may reduce to a first order hyperbolic partial differential equation in case of weak surface tension, upwinding also guarantees the convergence of the solution in a wider range of cases. Such an example where accounting for surface tension is not needed is given in [7], which authors created a numerical procedure for predicting the ice accretion over an aircraft surface due to in-flight icing phenomena: the process is first driven by droplets growth and coalescence, the contact angle and the surface tension playing a crucial role in droplets accretion and motion, and the history of every droplet is traced by means of a Lagrangian approach; after a trigger value of the mean bubble radius is reached, continuous film or rivulet flow pattern takes place and the the liquid layer evolution, which is modeled via an Eulerian approach involving the solution of continuity and energy equations, is driven by water deposition, ice accretion, evaporation process and shear of the external air flow.
In the present study, the convective term $\nabla \cdot \tilde{\boldsymbol{Q}}$ of Eq. (3.1) is discretized via a first order upwind scheme. Hence, the flux

$$\tilde{\boldsymbol{Q}} = \tilde{\boldsymbol{u}}\, \tilde{h} = \begin{Bmatrix} \tilde{q} \\ \tilde{s} \end{Bmatrix} \tag{3.10}$$

is decomposed into two contributions. Referring to x direction only, $\tilde{q}^{+} = \tilde{u}^{+}\, \tilde{h}$ refers to the the wave propagation with positive velocity, while $\tilde{q}^{-} = \tilde{u}^{-}\, \tilde{h}$ refers to the wave propagation with negative velocity.
Using finite volume notation and referring to non-dimensional quantities, the volume integral of the divergence for the i,j-th element can be expressed as a face integral,

$$\frac{1}{V_{i,j}} \int_{V_{i,j}} \nabla \cdot \tilde{\boldsymbol{Q}}\, dV = \frac{1}{V_{i,j}} \int_{\Omega_{i,j}} \tilde{\boldsymbol{Q}} \cdot \hat{\boldsymbol{n}}\, d\Omega = \frac{\tilde{q}_{i+\frac{1}{2},j} - \tilde{q}_{i-\frac{1}{2},j}}{\Delta \tilde{x}_i} + \frac{\tilde{s}_{i,j+\frac{1}{2}} - \tilde{s}_{i,j-\frac{1}{2}}}{\Delta \tilde{y}_j} \tag{3.11}$$

$\Delta \tilde{x}_i$, $\Delta \tilde{y}_j$ being the dimensions i,j-th element faces.
The fluxes that cross the faces of the i,j-th element along x direction can be

calculated as,

$$\tilde{q}_{i-\frac{1}{2},j} \simeq \frac{1}{2}\left(\tilde{q}^{+}_{i-1,j} + \left|\tilde{q}^{+}_{i-1,j}\right|\right) + \frac{1}{2}\left(\tilde{q}^{-}_{i,j} - \left|\tilde{q}^{-}_{i,j}\right|\right) \tag{3.12}$$

$$\tilde{q}_{i+\frac{1}{2},j} \simeq \frac{1}{2}\left(\tilde{q}^{+}_{i,j} + \left|\tilde{q}^{+}_{i,j}\right|\right) + \frac{1}{2}\left(\tilde{q}^{-}_{i+1,j} - \left|\tilde{q}^{-}_{i+1,j}\right|\right) \tag{3.13}$$

where the positive flux $\tilde{q}^{+}$ and the negative flux $\tilde{q}^{-}$ are given by,

$$\tilde{q}^{+}_{i,j} = -\frac{1}{3}\frac{\tilde{p}_{i+1,j} - \tilde{p}_{i,j}}{\tilde{x}_{i+1} - \tilde{x}_{i}}\,\tilde{h}^{3}_{i,j} + \mathrm{Ca}\,\frac{\tilde{\tau}_x}{2}\,\tilde{h}^{2}_{i,j} \tag{3.14}$$

$$\tilde{q}^{-}_{i,j} = -\frac{1}{3}\frac{\tilde{p}_{i,j} - \tilde{p}_{i-1,j}}{\tilde{x}_{i} - \tilde{x}_{i-1}}\,\tilde{h}^{3}_{i,j} + \mathrm{Ca}\,\frac{\tilde{\tau}_x}{2}\,\tilde{h}^{2}_{i,j} \tag{3.15}$$

$\tilde{x}_i$ referring to the center-element downhill coordinate.
The expressions of the fluxes $\tilde{q}^{+}_{i,j}$ and $\tilde{q}^{-}_{i,j}$ ensure that the pressure gradient on each face is always computed with a second order accurate centered difference:

$$\left.\frac{\partial\tilde{p}}{\partial\tilde{x}}\right|_{i\pm\frac{1}{2},j} \simeq \frac{\tilde{p}_{\left(i\pm\frac{1}{2}\right)+\frac{1}{2},j} - \tilde{p}_{\left(i\pm\frac{1}{2}\right)-\frac{1}{2},j}}{\tilde{x}_{\left(i\pm\frac{1}{2}\right)+\frac{1}{2}} - \tilde{x}_{\left(i\pm\frac{1}{2}\right)-\frac{1}{2}}} \tag{3.16}$$

The pressure field, Eq. (3.2), is calculated from the values of the film distribution $\tilde{h}$ over the computational domain and substituted in Eqs. (3.14) and (3.15). The capillary pressure $\nabla^2\tilde{h}$, the only contribution depending on the spatial derivatives of $\tilde{h}$, is implemented via a second order centered scheme, leading to,

$$\left.\frac{\partial^2\tilde{h}}{\partial\tilde{x}^2}\right|_{i,j} \simeq a_{i,1}\,\tilde{h}_{i-1,j} + a_{i,2}\,\tilde{h}_{i,j} + a_{i,3}\,\tilde{h}_{i+1,j} \tag{3.17}$$

the coefficients $a_{i,\,1-3}$ being equal to:

$$a_{i,1} = 2\,\left[(\tilde{x}_i - \tilde{x}_{i-1})\,(\tilde{x}_{i+1} - \tilde{x}_{i-1})\right]^{-1} \tag{3.18}$$

$$a_{i,2} = -2\,\left[(\tilde{x}_{i+1} - \tilde{x}_i)\,(\tilde{x}_i - \tilde{x}_{i-1})\right]^{-1} \tag{3.19}$$

$$a_{i,3} = 2\,\left[(\tilde{x}_{i+1} - \tilde{x}_i)\,(\tilde{x}_{i+1} - \tilde{x}_{i-1})\right]^{-1} \tag{3.20}$$

Combining centered scheme to calculate the capillary pressure, Eqs. (3.17), (3.18), (3.19) and (3.20), and upwinding to calculate the fluxes through the element faces, Eqs. (3.14) and (3.15), it is easy to demonstrate that the higher order derivatives of $\tilde{h}$ are treated with a second order centered scheme. The implemented spatial discretization mainly differs from [13, 14] in the computation of the nonlinear prefactor $\tilde{h}^3$, that multiplies the pressure gradient, see Eq. (3.1). In fact, the prefactor $\tilde{h}^3$ multiplying $\nabla\nabla^2\tilde{h}$ is treated as a diffusivity and the contribution of gravity driving action, here given by $\frac{1}{3}\,\mathrm{Bo}\,\sin\alpha\,\tilde{h}^3$, is discretized with a centered scheme in [14], see chapter 2.5 for the detailed explanation of the literature numerical scheme, while they are both implemented through upwinding in the current discretization.

3.2 Time discretization

Since discretizing Eq. (3.1) in the time space with an explicit method would lead to unacceptable computational costs due to the restrictive stability constraint on the time step, $\Delta\tilde{t} \propto \Delta\tilde{x}^4$, the backward Euler scheme is adopted for marching in time. An ADI factorization is also implemented in the Finite Volume Method solver, in order to gain an additional reduction of computational costs. Following the approach of Witelski and Bowen [13], the film flux is decomposed into two components isolating the mixed derivatives of $\tilde{h}$, which derives from the capillary pressure gradient $\nabla\nabla^2\tilde{h}$, in the expression of $\tilde{\boldsymbol{Q}}$:

$$\tilde{\boldsymbol{Q}} = \tilde{\boldsymbol{F}} + \frac{\tilde{h}^3}{3}\begin{Bmatrix} \dfrac{\partial}{\partial\tilde{x}}\left(\dfrac{\partial^2\tilde{h}}{\partial\tilde{y}^2}\right) \\ \dfrac{\partial}{\partial\tilde{y}}\left(\dfrac{\partial^2\tilde{h}}{\partial\tilde{x}^2}\right) \end{Bmatrix} \tag{3.21}$$

The ADI factorization allows to treat explicitly the mixed derivatives of $\tilde{h}$, thus only the contribution given by $\tilde{\boldsymbol{F}}$ is treated implicitly. It derives that two pentadiagonal nonlinear matrices have to be solved at each time step. Linearizing $\tilde{\boldsymbol{F}}$ by means of the Jacobian matrix, the algebraic systems become linear and can be easily solved with Gauss method.
In the present study, the prefactor $\tilde{h}^3$ multiplying the pressure gradient, see Eq. (3.1), is treated implicitly, while in the discretization of [11, 13] is evaluated with a predictor-corrector method and the solution of the two algebraic systems is iterated more times at each time step, leading to the *iterative factorized method*, which is here abandoned in favor of a *non-iterative* method. Only the backward Euler scheme rather than Crank-Nicolson is implemented in the present FVM solver since it is not possible to gain second order accuracy in time with one-step ADI methods involving mixed derivatives, unless the *iterative factorized method* is applied [13].
Introducing $\tilde{\boldsymbol{F}}$ according to Eq. (3.21),

$$\tilde{\boldsymbol{F}} = \begin{Bmatrix} \tilde{f} \\ \tilde{g} \end{Bmatrix} \tag{3.22}$$

and computing the Jacobian matrices $\boldsymbol{Ax}$ and $\boldsymbol{Ay}$ as,

$$\boldsymbol{Ax} = \frac{\partial}{\partial\tilde{h}}\left(\frac{\partial\tilde{f}}{\partial\tilde{x}}\right),\ \boldsymbol{Ay} = \frac{\partial}{\partial\tilde{h}}\left(\frac{\partial\tilde{g}}{\partial\tilde{y}}\right) \tag{3.23}$$

the implemented ADI factorization takes the form,

$$\left[\boldsymbol{I} + \Delta\tilde{t}\,\boldsymbol{Ax}^n\right]\left[\boldsymbol{I} + \Delta\tilde{t}\,\boldsymbol{Ay}^n\right]\Delta\tilde{h}^n = -\Delta\tilde{t}\,\nabla\cdot\tilde{\boldsymbol{Q}}^n \tag{3.24}$$

leading to the following split equations,

$$\left[\boldsymbol{I} + \Delta\tilde{t}\,\boldsymbol{Ax}^n\right]\Delta\tilde{h}^* = -\Delta\tilde{t}\,\nabla\cdot\tilde{\boldsymbol{Q}}^n \tag{3.25}$$

$$\left[\boldsymbol{I} + \Delta\tilde{t}\,\boldsymbol{Ay}^n\right]\Delta\tilde{h}^n = \Delta\tilde{h}^* \tag{3.26}$$

$$\tilde{h}^{n+1} = \tilde{h}^n + \Delta\tilde{h}^n \tag{3.27}$$

with $\boldsymbol{Ax}$ and $\boldsymbol{Ay}$ evaluated at the n-th time step.
The time step $\Delta\tilde{t}$ is dynamically adjusted after each time step,

$$\Delta\tilde{t} = \frac{\xi}{\max\left\{\frac{\left|\tilde{h}_{i,j}^{n+1}-\tilde{h}_{i,j}^{n}\right|}{\tilde{h}_{i,j}^{n+1}}\right\}}\Delta\tilde{t} \tag{3.28}$$

ξ being the tolerance for the allowed $\Delta h/h$.
The main issue of applying such an ADI method consists in the analytical derivation of the Jacobian matrices $\boldsymbol{Ax}$, $\boldsymbol{Ay}$ and their implementation in the corresponding routine of the FVM solver. Since the flux $\tilde{\boldsymbol{Q}}$ is decomposed into the positive and negative contributions according to upwind scheme, the Jacobian matrices are also given by the contributions of the positive and the negative liquid propagation. Referring to x Cartesian direction only, this means that,

$$\boldsymbol{Ax} = \frac{\partial}{\partial\tilde{h}}\left(\frac{\partial\tilde{f}^{+}}{\partial\tilde{x}}\right) + \frac{\partial}{\partial\tilde{h}}\left(\frac{\partial\tilde{f}^{-}}{\partial\tilde{x}}\right) \tag{3.29}$$

with:

$$\tilde{f} = \tilde{f}^{+} + \tilde{f}^{-} \tag{3.30}$$

According to Eq. (3.21) and to the spatial discretization given by Eqs. (3.14) and (3.15), $\tilde{f}^{\pm}$ are given, for the i,j-th element of the computational grid, by the following expressions:

$$\tilde{f}_{i,j}^{+} = \frac{1}{2}\frac{\tilde{q}_{i,j}^{+} + \left|\tilde{q}_{i,j}^{+}\right|}{\tilde{q}_{i,j}^{+}}\left(\tilde{q}_{i,j}^{+} - \frac{\tilde{h}_{i,j}^{3}}{3}\frac{\left.\frac{\partial^2\tilde{h}}{\partial\tilde{y}^2}\right|_{i+1,j} - \left.\frac{\partial^2\tilde{h}}{\partial\tilde{y}^2}\right|_{i,j}}{\tilde{x}_{i+1}-\tilde{x}_{i}}\right) \tag{3.31}$$

$$\tilde{f}_{i,j}^{-} = \frac{1}{2}\frac{\tilde{q}_{i,j}^{-} - \left|\tilde{q}_{i,j}^{-}\right|}{\tilde{q}_{i,j}^{-}}\left(\tilde{q}_{i,j}^{-} - \frac{\tilde{h}_{i,j}^{3}}{3}\frac{\left.\frac{\partial^2\tilde{h}}{\partial\tilde{y}^2}\right|_{i,j} - \left.\frac{\partial^2\tilde{h}}{\partial\tilde{y}^2}\right|_{i-1,j}}{\tilde{x}_{i}-\tilde{x}_{i-1}}\right) \tag{3.32}$$

Eqs. (3.31) and (3.32) are derived in $\tilde{h}$ in order to fill the pentadiagonal Jacobian matrix $\boldsymbol{Ax}$, which non-zero elements are computed, according to Eq. (3.29), as

$$\begin{aligned} Ax_{\,k,k+m} &= \frac{1}{\tilde{x}_{i}-\tilde{x}_{i-1}}\left(\frac{\partial\tilde{f}_{i,j}^{+}}{\partial\tilde{h}_{i+m,j}} - \frac{\partial\tilde{f}_{i-1,j}^{+}}{\partial\tilde{h}_{i+m,j}}\right) \\ &+ \frac{1}{\tilde{x}_{i+1}-\tilde{x}_{i}}\left(\frac{\partial\tilde{f}_{i+1,j}^{-}}{\partial\tilde{h}_{i+m,j}} - \frac{\partial\tilde{f}_{i,j}^{-}}{\partial\tilde{h}_{i+m,j}}\right) \end{aligned} \tag{3.33}$$

with $k = i + (j-1)\,n_i$ and m being an integer so that $m \in [-2,+2]$.
Note that the terms

$$\frac{1}{2}\frac{\tilde{q}_{i,j}^{+} + \left|\tilde{q}_{i,j}^{+}\right|}{\tilde{q}_{i,j}^{+}},\ \frac{1}{2}\frac{\tilde{q}_{i,j}^{-} - \left|\tilde{q}_{i,j}^{-}\right|}{\tilde{q}_{i,j}^{-}} \tag{3.34}$$

can only assume values 0 and 1, serving to establish if the film flux is propagating through the i,j-th element in positive/negative direction or not. These terms are treated as constant factors when deriving Eqs. (3.31) and (3.32). Such an imposition did not show any problem involving convergence of the

solution.
Comparing the performances of the implicit solver with another in-house explicit solver reveals a huge gain on Δt (about 10^8 times when $\Delta x \simeq \delta$) and a corresponding strong reduction in terms of simulation time. Time step of about 10^6 the Neumann limit, Eq. (2.87), which is less restrictive than the stability constraint given by the explicit solver, are reached running the implicit solver with spatial discretization step of about δ.

3.3 Boundary and initial conditions

At the inlet boundary (corresponding to the top of the plate, $x = 0$), the undisturbed film flow per unit length $Q_{in} = u_\infty h_\infty$ is supposed to enter the domain. This condition implies that the inlet pressure equals the one of the undisturbed film. Thus the following boundary conditions are implemented at the top of the plate:

$$\tilde{\boldsymbol{Q}}_{\boldsymbol{in}} \cdot \hat{\boldsymbol{n}} = \frac{\mathrm{Bo}}{3} \sin\alpha + \frac{\mathrm{Ca}}{2} \tilde{\tau}_x \tag{3.35}$$

$$\tilde{p}_0 = \mathrm{Bo} \cos\alpha + \tilde{\Pi}_\infty \tag{3.36}$$

$$\tilde{h}_0 = 1 \tag{3.37}$$

At the outlet boundary ($x = L_x$), zero flux entering the domain, zero pressure gradient and mirroring condition on the film thickness, leading to fully developed flow going out, are imposed:

$$\tilde{\boldsymbol{Q}}_{\boldsymbol{in}} \cdot \hat{\boldsymbol{n}} = 0 \tag{3.38}$$

$$\nabla\tilde{p} \cdot \hat{\boldsymbol{n}} = 0 \tag{3.39}$$

$$\nabla\tilde{h} \cdot \hat{\boldsymbol{n}} = 0 \tag{3.40}$$

At the lateral boundaries ($y = 0$, L_y), symmetry conditions are imposed, as in an array of stable dry-patches:

$$\tilde{\boldsymbol{Q}} \cdot \hat{\boldsymbol{n}} = 0 \tag{3.41}$$

$$\nabla\tilde{h} \cdot \hat{\boldsymbol{n}} = 0 \tag{3.42}$$

The onset of the dry-patch is induced by a discontinuity in the initial wetting properties of the substrate, rather than introducing a physical obstacle as in [3]. In particular, the film flow is initialized with a non-wettable small square patch, imposing:

- zero flux through the non-wettable patch boundaries, $\tilde{\boldsymbol{Q}} \cdot \hat{\boldsymbol{n}} = 0$;
- zero film height, $\tilde{h}_{i,j} = 0$, inside the non-wettable patch, where the governing equations are not solved.

Such a situation occurs in the experiments of Podgorski et al. [2] and Rio et al. [19], where dry-patches were induced using an air-jet in order to create a little hole in the uniform wetting layer, with the diameter of such an air-jet being of the order of the capillary length of the liquid.
Two sets of different initial conditions can be chosen:

- dry condition:

$$\tilde{h}_{i,j} = \begin{cases} 1 \text{ if } x_i < 0.1\, L_x \\ \tilde{\delta} \text{ if } x_i > 0.1\, L_x \end{cases} \tag{3.43}$$

- wet condition:

$$\tilde{h}_{i,j} = 1 \, \forall x_i \in [0, L_x],\, y_j \in [0, L_y] \tag{3.44}$$

The wet condition is used in order to simulate the flow of a film, initially undisturbed, perturbed by means of the non-wettable patch, which may eventually induce a larger dry-patch. The dry condition allows to study the contact line motion and possibly the phenomena related to finger instability; note that a small portion of plate close to the top is thought to be wet in order to facilitate convergence of the solution.

3.4 Validation of the FVM solver

The in-house code is first validated in two different test cases:

- 1D simulation of a gravity driven film flowing over an inclined plate: an initially dry plate progressively wetted by an advancing thin liquid front is investigated with the aim of validating the disjoining pressure model, which is used for modelling the surface wettability, following the same approach of [15].

- 2D simulation of the breakup of a continuous film covering the inclined plate, due to a small non-wettable patch imposed inside the computational domain: the experiment of [2, 19] are numerically replicated and the resulting dry-patch shape is compared with the semi-empirical model given in [2].

$\rho\,(\mathrm{kg/m^3})$	$\mu\,(\mathrm{Pa\,s})$	$\sigma\,(\mathrm{N/m})$	(n, m)	δ/h_∞	$\theta_e\,(\mathrm{deg})$
950	0.019	0.021	$(3, 2)$	0.05	20

Table 3.1: Physical properties of the simulated silicone oil (poly-dimethyl-siloxane) and imposed parameters defining the disjoining pressure.

Silicone oil (poly-dimethyl-siloxane), which properties are listed in table 3.1, is simulated. This high viscosity liquid was chosen since it was used in [2, 19], which experiments are here numerically replicated. Also, its properties are suitable for lubrication approximation, because the high viscosity makes the inertial forces a secondary effect when dewetting phenomena occur. The other main parameters that are imposed for the following simulations are the precursor film thickness δ and the exponents n, m of interaction potential in the disjoining pressure, see Eq. (3.3). It is important to point out that imposing the physical value of the precursor film (of the order of nm) would lead to

unacceptable computational costs, for this reason higher values of δ are usually imposed, as specified in [3, 11, 15]. As explained in chapter 2.2.2, Zhao and Marshall [15] extended the definition of the disjoining pressure introducing the correction factor f, Eq. (3.5), in order to correctly model the surface wettability when non-physical values of the precursor film thickness are imposed. However, the effect of the precursor film on the results of the numerical computations was investigated even in [11], analyzing the drop shape near the apparent contact line for different values of δ, revealing a weak dependence of the solution on the imposed δ. For this reason, the value of $\delta = 0.05\, h_\infty$, also used in [11, 15], is chosen for the presented computations. The exponents (n, m) are fixed to the $(3, 2)$, according to most previous computational studies [15]. Different values may be imposed, but the good numerical stability properties of $(n, m) = (3, 2)$ make this choice more convenient.
The equilibrium contact angle is fixed to $\theta_e = 20°$, which seems to be the actual limit of small slope approximation, since it is the highest value simulated in lubrication theory framework. In fact, Sellier [3] investigated θ_e ranging in $[0, 20°]$, while Zhao et al. [15] simulated an inclined plate with textured equilibrium contact angle, which ranges around the mean value of 11°, reaching the maximum value of 22°. Schwartz et al. [11] simulated the spreading of glycerin drops on a textured surface (composed by stripes of glass and Teflon), but they could not compare the numerical results with experimental evidences, since it was not possible to impose equilibrium contact angles ranging between 38° and 114° as in the real test-case, both values overcoming the small slope approximation validity.
Each computation is identified by the plate inclination α to the horizontal, the shear $\boldsymbol{\tau_g}$ applied by the external gas flow and the undisturbed flow per unit length $Q_{in} = u_\infty\, h_\infty$ entering the domain through the inlet section. Here only gravity driven film flow are investigated, thus the shear applied at the free surface is equal to zero:

$$\boldsymbol{\tau_g} = \begin{Bmatrix} \tau_x \\ \tau_y \end{Bmatrix} = \begin{Bmatrix} 0 \\ 0 \end{Bmatrix} \tag{3.45}$$

Finally, it is important to point out that the spatial discretization step is kept constant for these simulations, since the investigated test cases do not need to vary the discretization step over the domain. Grid independence analysis suggested the use of a non-dimensional spatial discretization step $\Delta x < h_\infty$.

3.4.1 Disjoining pressure validation

The consistence of the disjoining pressure model for describing the dynamics near the apparent contact line is analyzed. The value of the equilibrium contact angle θ_e, in fact, is used to define the disjoining pressure through Eq. (3.4). However, the actual θ is calculated from the maximum slope of the film thickness distribution near the apparent contact line, i.e. from the local modulus of the gradient of h. Zhao and Marshall [15] validated Eqs. (3.3) and (3.4) in case of one dimensional film flow advancing along an inclined plate, concluding that the calculated dynamic contact angle respects the modified

Tanner-Hoffman-Voinov formula,

$$\theta^3 = \theta_e^3 \left(C_1 + C_2 \frac{\mu\, u_c}{\sigma} \right) \tag{3.46}$$

where θ is the dynamic angle, the contact line velocity u_c is given by Eq. (2.31) and C_1, C_2 are constants (C_1 depending on the spatial discretization accuracy, which influences the calculated value of θ). Both C_1 and C_2 are computed in [15] in order to fit the computed dynamic contact angle.
Simulations are run in the present study considering the 1D problem (a film flowing over an inclined plate initially dry) with $\theta_e = 20°$ and $\alpha = 30°$.

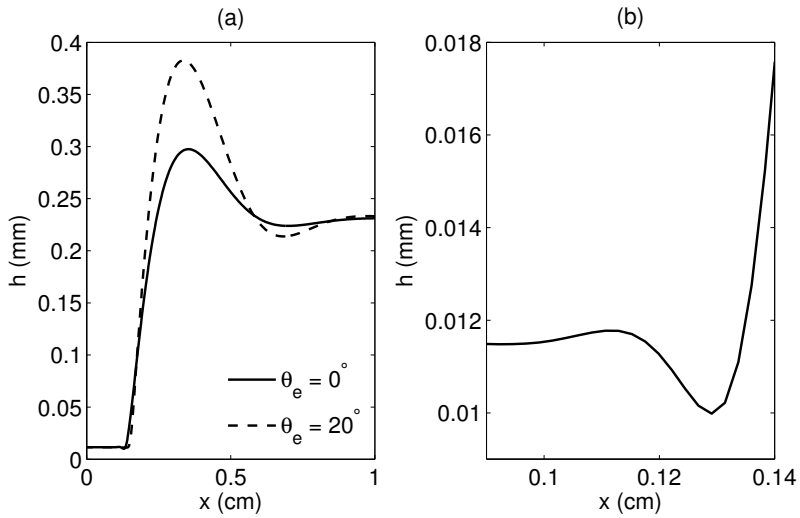

Figure 3.1: Self-similar free surface profile of a film flowing over an inclined plate for equilibrium contact angle $\theta_e = 20°$ and for a wettable surface, $\theta_e = 0°$ (a); zoom of the solution near the apparent contact line for $\theta_e = 0°$ (b). $\alpha = 30°$, $Q_{in} = 0.01\,\mathrm{cm}^2/\mathrm{s}$.

Figure 3.1(a) shows the self-similar capillary ridge shape surrounding the contact line for two different values of the imposed equilibrium contact angles, confirming that disjoining pressure is able to model the wettability of the solid substrate. Such a trend of the free surface (i.e. ridge appearance) can be found in a number of literature works [15, 18, 28] studying film flow under lubrication theory.
Figure 3.2(a) shows the computed dynamic contact angle as a function of the contact line velocity: the 1D numerical results (circles) are compared with Eq. (3.46); in order to guarantee a good resolution near the contact line, it was chosen a spatial discretization step equal to $\Delta x = 0.1\, h_\infty$. The effect of a change in the spatial discretization accuracy on the evaluation of θ is shown in figure 3.2(b): it can be noticed that the regression coefficient C_1 of Eq. (3.46) reduces to 1 (i.e. the condition $\theta = \theta_e$ if $u_c = 0$ is respected) for high discretization accuracy ($\Delta x \to 0$).
It can be stated that the disjoining pressure model is a useful instrument for modeling surface wettability, since it correctly describes the contact line

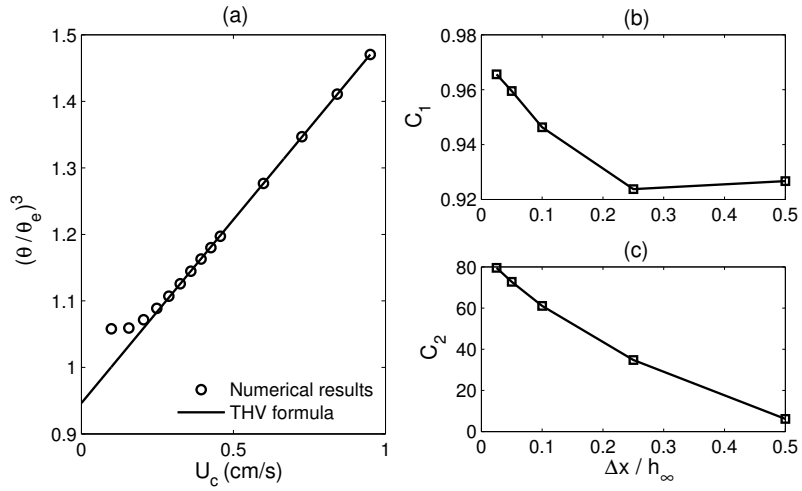

Figure 3.2: Dynamic contact angle for 1D film flow as a function of contact line velocity, $\Delta x = 0.1\, h_\infty$ (a); influence of discretization accuracy on regression coefficients $C_{1,2}$ of Eq. (3.46) (b), (c).

dynamics and it is easy to implement, without particular limitations on numerical stability occurring; only applying higher values of the equilibrium contact angle, the numerical instability grows and lower time steps are needed for ensuring convergence of the solution, but this is probably due to the small slope approximation, that overestimates the capillary forces leading to non-physical results, rather than the disjoining pressure itself.

3.4.2 Validation for film breakup

We validate the code simulating the experimental configurations of [2, 19] and comparing the dry-patch shape with the prediction of the empirical model of Podgorski et al. [2], which validity is confirmed by its perfect agreement with several experimental data [2, 19], see for example figure 2.4. Eqs. (2.14) and (2.15) are the parametric equations describing the dry-patch shape, which depends on the radius of curvature at the dry-patch apex, given by Eq. (2.16). Starting from an undisturbed film flow covering the inclined plate, we apply the non-wettable small patch, as previously explained, in order to perturb the flow and eventually generate a dry-patch. The choice of the obstacle size L_{obst} follows Sellier [3]:

$$\frac{L_{obst}}{h_\infty} = (\mathrm{Bo}\, \sin\alpha)^{-\frac{1}{3}} \tag{3.47}$$

The numerical results of figure 3.3(a) shows the stationary distribution $h(x, y)$ of the film height. Confirming both experimental and analytical evidences [2, 9, 19], a capillary ridge with higher film thickness and flow rate appears near the contact line of the resulting dry-patch. Moreover, some residual drops, that are slowly draining, can be observed. Figure 3.3(b) compares numerical contact line of the dry-patch, obtained directly from the stationary film distribution, with Eqs. (2.14), (2.15) and (2.16). The apparent contact

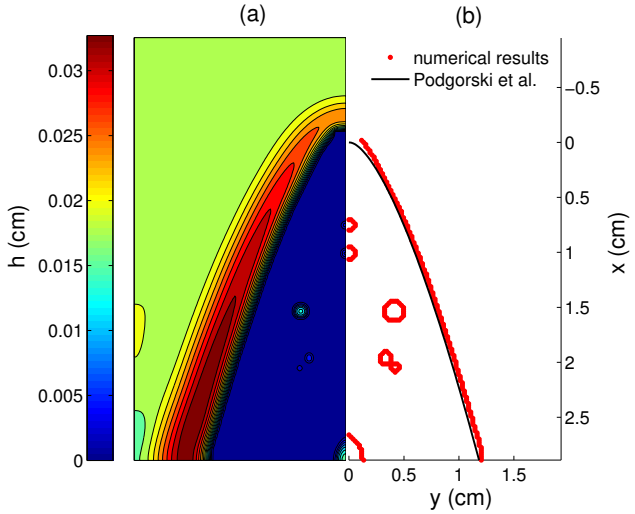

Figure 3.3: Computed stationary film height (a); dry-patch validation with Eqs. (2.14), (2.15) and (2.16) (b). $Q_{in} = 5.9 \times 10^{-3}\,\mathrm{cm}^2/\mathrm{s}$, $\alpha = 30°$.

line is here located where the precursor film is triggered. More refined method can be used: for example, the apparent contact line may be defined from the maximum curvature of the free surface. It can be noticed that the numerical dry-patch fits exactly the empirical model of [2], which in turn fits perfectly the experimental data.
Thus, we may be confident with the model accuracy, since, after the 1D validation with the Tanner-Hoffmann-Voinov formula, Eq. (3.46), the in-house code is properly validated with both qualitative (capillary ridge occurrence) and quantitative observations (dry-patch matching) in the 2D case.

3.5 Contact line dynamics

The definition of the critical liquid flow rate leading to film breakup with generation of a stable dry-patch and the analysis of the behavior of moving contact lines are crucial for a number of engineering applications: in particular, knowing the threshold between continuous film and rivulet flow pattern can improve the coating processes; also in in-flight icing phenomenon the knowledge of the flow pattern transitions influences the predicted surface roughness due to ice accretion. Such an analysis is carried out running several simulations, with the aim of tracing the critical flow rate in different test cases. The numerical results are compared with a novel theoretical model, which was first validated with literature experimental evidences.

3.5.1 Theoretical model for the critical flow rate

A simplified model was developed in order to predict the stability of a dry-patch appearing when a laminar film flows over an inclined plate driven by gravity, imposing the mass, momentum and energy balances on a macroscopic

control volume of liquid at the apex of the dry-patch, containing a section of capillary ridge, where the undisturbed flow is deviated. The occurrence of such a ridge surrounding the contact line is confirmed both by figure 3.3, analytical and experimental evidences, as previously underlined. Also inertia effect is taken into account in order to enhance the model flexibility.
Consider a dry-patch, formed after a thin film breaks up into two rivulets: if the dry-patch is stable (i.e. its contact line does not move), the stationary mass, momentum and energy balances must be respected. Thus, a stable dry-patch, neither advancing or receding, is expected for a given value of the undisturbed film flux per unit length Q_{CR}: above the critical value, the dry-patch will shed away; below the critical value, the dry-patch will grow up.

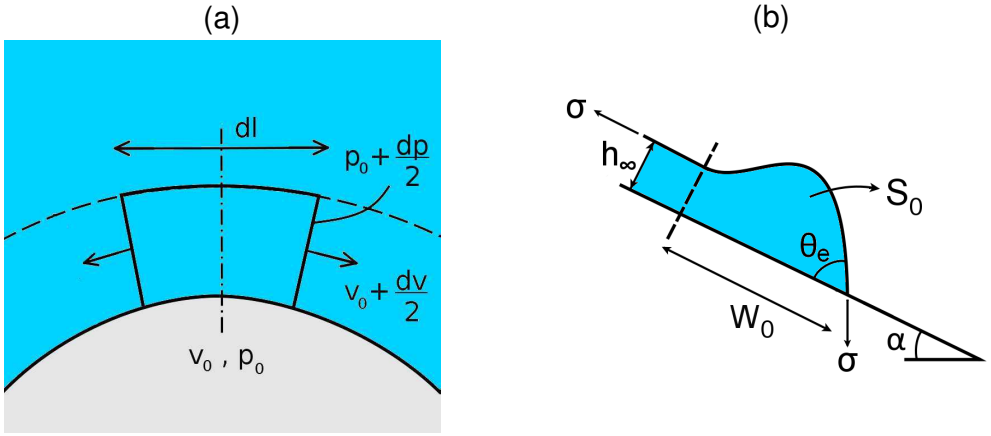

Figure 3.4: Control volume of liquid at the apex of the dry-patch (a); section of the control volume within the capillary ridge (b).

Let's now consider a control volume of length dl within the capillary ridge at the vertex of the contact line delimiting the dry-patch, see figure 3.4(a), and assume that the undisturbed liquid flow deviates instantly once it enters the control volume. Thus, from mass balance on such a control volume,

$$\dot{m}_{in} = \dot{m}_{out} \tag{3.48}$$

derives that the exiting mass flow,

$$\dot{m}_{out} = 2\,\rho \left(v_0 + \frac{dv}{2}\right)\left(S_0 + \frac{dS}{2}\right) \tag{3.49}$$

must be equal to the incoming flow, given by the undisturbed film flux,

$$\dot{m}_{in} = \rho\, u_\infty\, h_\infty\, dl \tag{3.50}$$

with S and v being the area of the capillary ridge section shown in figure 3.4(b) and the liquid velocity along contact line direction (the pedix "0" simply refers to the apex section).
Dividing both sides of Eq. (3.48) for $\rho\, dl$, knowing from symmetry condition that $v_0 = 0$ and neglecting the high order terms leads to:

$$u_\infty\, h_\infty = \left.\frac{dv}{dl}\right|_0 S_0 \tag{3.51}$$

The momentum balance along the undisturbed flow direction correlates the entering momentum flux with the external forces acting on the capillary ridge control volume, given by surface tension and ridge weight,

$$\sigma\,(1-\cos\theta_e)\;dl = \rho\,g\,S_0\,dl\,\sin\alpha + (\dot{m}_{in}\,u_\infty + p_\infty\,h_\infty\,dl) \tag{3.52}$$

where the pressure of the undisturbed film is equal to:

$$p_\infty = \rho\,g\,h_\infty\,\cos\alpha \tag{3.53}$$

Dividing both sides of Eq. (3.52) for dl gives:

$$\sigma\,(1-\cos\theta_e) = \rho\,{u_\infty}^2\,h_\infty + \rho\,g\left({h_\infty}^2\,\cos\alpha + S_0\,\sin\alpha\right) \tag{3.54}$$

Finally, the energy balance can be written as,

$$\dot{m}_{in}\,e_{in} + \sigma\,u_\infty\,dl = \dot{m}_{out}\,e_{out} + 2\,\sigma\,\left(v_0 + \frac{dv}{2}\right)\left(\Gamma_0 + \frac{d\Gamma}{2}\right) \tag{3.55}$$

Γ_0 being the ridge perimeter. $\sigma\,u_\infty\,dl$ and $2\,\sigma(v_o + dv/2)(\Gamma_0 + d\Gamma/2)$ define the incoming and outgoing surface energy respectively, while e_{in} and e_{out}, i.e. the specific energy entering and exiting the control volume due to convective transport, can be expressed as,

$$e_{in} = \frac{1}{2}\,{u_\infty}^2 + \frac{p_\infty}{\rho} + g\,\frac{W_0}{2}\,\sin\alpha \tag{3.56}$$

$$e_{out} = \frac{1}{2}\left(v_0 + \frac{dv}{2}\right)^2 + \frac{p_0 + \frac{dp}{2}}{\rho} \tag{3.57}$$

$g\,W_0/2\,\sin\alpha$ being the potential energy calculated with respect of the ridge centroid, W_0 being the ridge width at the dry-patch apex.
Substituting the specific energies in Eq. (3.55) and neglecting high order terms allows to write the energy balance as:

$$\rho\,u_\infty\,h_\infty\left[\frac{1}{2}\,{u_\infty}^2 + g\left(h_\infty\,\cos\alpha + \frac{W_0}{2}\,\sin\alpha\right) - \frac{p_0}{\rho}\right] + \sigma\left(u_\infty - \left.\frac{dv}{dl}\right|_0\,\Gamma_0\right) = 0 \tag{3.58}$$

Introducing the following non-dimensional quantities

$$\tilde{l} = \frac{l}{h_\infty},\;\tilde{p} = \frac{p}{(\sigma/h_\infty)},\;\tilde{v} = \frac{v}{u_\infty},\;\tilde{S} = \frac{S}{{h_\infty}^2},\;\tilde{W} = \frac{W}{h_\infty},\;\tilde{\Gamma} = \frac{\Gamma}{h_\infty} \tag{3.59}$$

and defining Bond number and Weber number,

$$\mathrm{Bo} = \frac{\rho\,g\,{h_\infty}^2}{\sigma},\;\mathrm{We} = \frac{\rho\,{u_\infty}^2\,h_\infty}{\sigma} \tag{3.60}$$

We being the ratio between liquid inertia and surface tension forces, Eqs. (3.51), (3.54) and (3.58) can be rewritten as:

$$1 - \left.\frac{d\tilde{v}}{d\tilde{l}}\right|_0\,\tilde{S}_0 = 0 \tag{3.61}$$

$$1 - \cos\theta_e = \mathrm{We} + \mathrm{Bo}\left(\cos\alpha + \tilde{S}_0\,\sin\alpha\right) \tag{3.62}$$

$$1 - \left.\frac{d\tilde{v}}{d\tilde{l}}\right|_0\,\tilde{\Gamma}_0 = \tilde{p}_0 - \left[\frac{\mathrm{We}}{2} + \mathrm{Bo}\left(\cos\alpha + \frac{\tilde{W}_0}{2}\,\sin\alpha\right)\right] \tag{3.63}$$

Both Weber number and Bond number depends univocally on the unknown film flux per unit length $Q_\infty = u_\infty h_\infty$ and the liquid properties, while $\tilde{p}_0$ and the ridge geometry, i.e. $\tilde{S}_0$, $\tilde{W}_0$ and $\tilde{\Gamma}_0$, are unknown. Since only three equations are available, some assumptions must be done. The pressure inside the ridge being given by the capillary pressure, it can be expressed as:

$$p_0 = \frac{1}{\Gamma_0}\int_0^{\Gamma_0}\frac{\sigma}{r}\,d\chi = -\frac{\sigma}{\Gamma_0}\int_0^{x(\Gamma_0)}\frac{\frac{d^2h}{dx^2}}{1+\left(\frac{dh}{dx}\right)^2}\,dx = \frac{\sigma}{\Gamma_0}\,\theta_e \tag{3.64}$$

Thus the non-dimensional liquid pressure is equal to:

$$\tilde{p}_0 = \frac{\theta_e}{\tilde{\Gamma}_0} \tag{3.65}$$

In order to simplify the model, the contribution of surface energy is neglected in the energy balance, Eq. (3.63), and the ridge perimeter Γ_0 is approximated with the ridge width W_0. Assuming that the capillary ridge always assumes a prescribed shape allows to define the geometric ratio:

$$\gamma = \frac{h_\infty W_0}{S_0} = \frac{\tilde{W}_0}{\tilde{S}_0} \tag{3.66}$$

Thus, Eqs. (3.61), (3.62) and (3.63) can be finally rewritten as:

$$1-\cos\theta_e = \mathrm{We} + \mathrm{Bo}\,\left(\cos\alpha + \tilde{S}_0\,\sin\alpha\right) \tag{3.67}$$

$$\frac{\theta_e}{\gamma\,\tilde{S}_0} = \frac{\mathrm{We}}{2} + \mathrm{Bo}\left(\cos\alpha + \frac{\gamma\,\tilde{S}_0}{2}\,\sin\alpha\right) \tag{3.68}$$

Solving Eqs. (3.67) and (3.68) in the unknown film flux Q_{CR} allows to trace Q_{CR} as a function of both the equilibrium contact angle and the plate inclination. The model is validated with experimental results of Podgorski et al. [2], the free parameter γ being computed in order to fit the data points. The geometric ratio γ is expected to be mainly a function of the equilibrium contact angle, which obviously influences the ridge shape. However, it was not possible to identify such a dependence because of the lack in literature results. Figure 3.5 shows a good agreement between the model and the experimental results of [2], confirming that Eqs. (3.67) and (3.68) are able to catch the main physics beyond a complex phenomenon as dry-patch occurrence. It was found that $\gamma = 0.67$ best fits the experimental points.

3.5.2 Numerical results

The implicit code was applied to the the dry-patch stability analysis, estimating the maximum critical mass flow allowing for its persistence. Following the procedure of experimental tests in [2], the undisturbed flow is first perturbed in order to generate a dry-patch, as done for the dry-patch validation. Once the stationary condition is reached, the obstacle is removed: if the dry-patch is

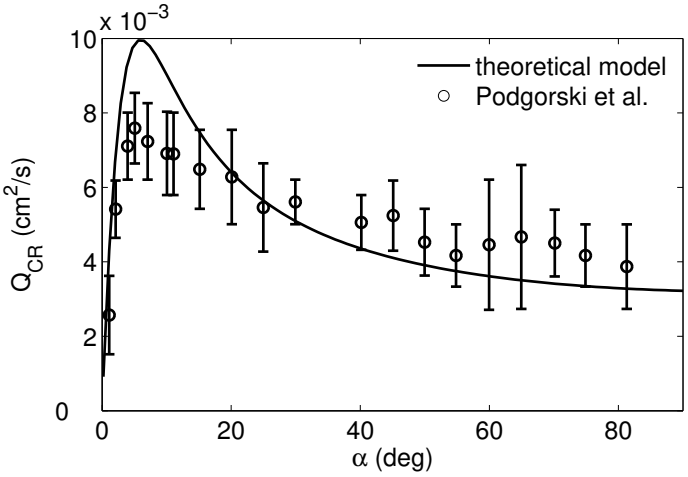

Figure 3.5: Critical film flux as a function of the plate inclination: theoretical model, Eqs. (3.67) and (3.68), vs experimental evidences of Podgorski et al. [2]. Liquid properties listed in table 3.1, $\theta_e = 30°$.

stable, the contact line doesn't move and a new stationary condition is immediately reached and the imposed flow rate Q_{in} is lower then the critical one; if the contact line starts advancing or the dry-patch closes up, Q_{in} is higher than Q_{CR}. The simulated liquid and the imposed parameters are listed in table 3.1; the spatial discretization step ranges between $0.25\,h_\infty$ and $0.75\,h_\infty$.
Running the code for increasing value of the film flow rate until the critical condition is reached, a set of points describing the critical flow rate dependence on the inclination of the plate was obtained. This allowed to compare the numerical results with a theoretical model, which simplifies the determination of the critical flow rate. This model is explained in detail in section 3.5.1. Calculating Weber number and Bond number with respect to the inlet film flow rate per unit length $Q_{in} = u_\infty\, h_\infty$, the critical flow rate Q_{CR} can be estimated solving Eqs. (3.67) and (3.68).

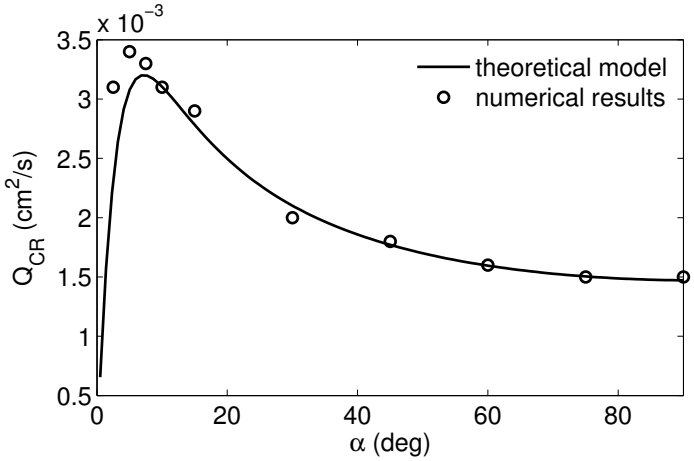

Figure 3.6: Comparison between critical flow rate deriving from numerical computations and theoretical model, Eqs. (3.67) and (3.68). $\theta_e = 20°$.

Figure 3.6 shows the critical flow rate as a function of the plate inclination for $\theta_e = 20°$ deriving from numerical simulations (circles), fitted by the theoretical model (continuous line). A good agreement was obtained, since both the position and the magnitude of the maximum of the critical flow rate, which establishes when the hydrostatic pressure overcomes the driving action of gravity as the main opponent to the capillary force, are well predicted.

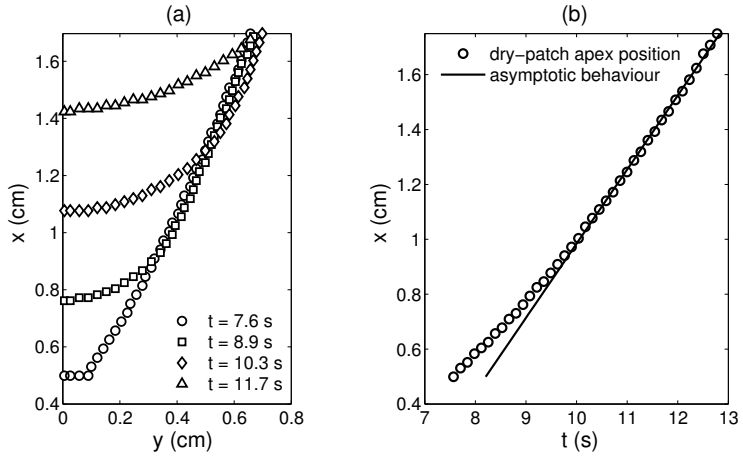

Figure 3.7: Moving contact line at different times (a); dry-patch apex position as a function of time (b). $Q_{in} = 7.5 \times 10^{-3}\,\mathrm{cm}^2/\mathrm{s}$, $\alpha = 30°$.

The dynamics of dry-patch re-wetting was also studied: if the imposed flow rate exceeds the critical value, the dry-patch is unstable and will be someway shed away once the non-wettable patch is removed. Figure 3.7(a) shows the dry-patch contact line at different times for a high value of the film flow rate, $Q_{in} >> Q_{CR}$. The dry-patch first adjusts its shape after the obstacle removal and then advances with a constant velocity, due to gravity force, rather than closing up. In figure 3.7(b) the position of dry-patch apex is traced as a function of time, confirming that a characteristic draining velocity, lower then the undisturbed film velocity u_∞, is reached. Since both the contact line shape and the contact line velocity tend to become constant in time, the thin layer evolves asymptotically, assuming a self-similar solution; this similarity is lost once the contact line apex approaches the outlet boundary due to the imposed boundary condition. It is important to point out that similarity solutions are also assumed in some analytical solutions, [4, 26], of a simplified form of the lubrication equations, as explained in chapter 2.4. From other simulations, it was observed that, when the flow rate is close to the critical value, $Q_{in} \simeq Q_{CR}$, and the plate inclination is sufficiently low, a characteristic draining velocity is still reached, confirming the dry-patch motion along the inclined plane, but the dry-patch also tends to close up with a lower velocity, perpendicular to the contact line itself, due to capillary effect.
Finally, the dynamic contact angle along a 2D moving contact line is computed tracing the maximum value of the free surface slope, which is calculated as the norm of the film height gradient ∇h, near the apparent contact line. The influence of the imposed flow rate Q_{in} and the position over the contact line,

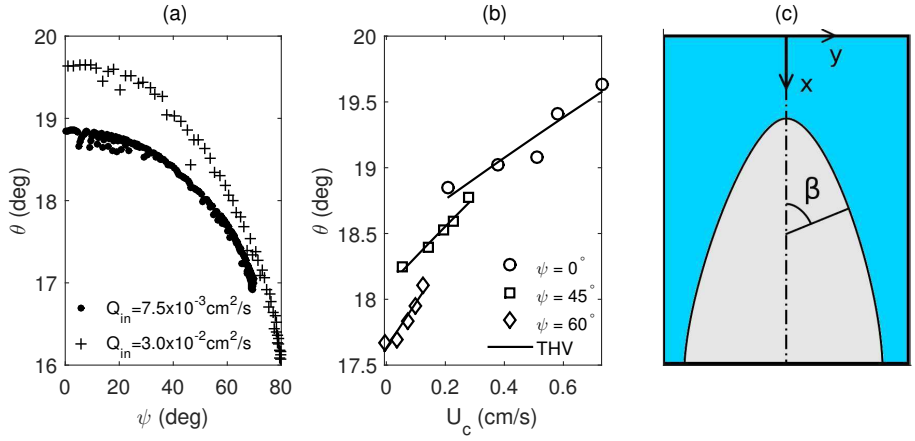

Figure 3.8: Dynamic contact angle as a function of the position over the contact line for two different flow rates (a). Dependence of the contact angle on contact line velocity, for $Q_{in} = 0.75,\ 1.5,\ 2.0,\ 3.0 \times 10^{-2}\,\mathrm{cm}^2/\mathrm{s}$, $\alpha = 30°$ (b). Definition of the coordinate β, identifying the position along the contact line (c).

.

which is identified by the angle β between the normal to the contact line and the x direction, see figure 3.8(c), are investigated. Figure 3.8(a) demonstrates that the dynamic contact angle varies along the contact line: in particular, the contact angle θ decreases for increasing value of β. This trend is confirmed by the relation $\tan\theta \propto x^{-\frac{3}{4}}$, obtained via post-processing of the results of [26]. Two different shapes of θ as a function of β, see figure 3.8(a), were obtained for two different flow rates: the discrepancy between the two curves is due to the additional dependence of θ on the contact line velocity. In figure 3.8(b) three values of β are chosen and the dynamic contact angle is plotted, for each β, against the contact line velocity, showing that the Tanner-Hoffman-Voinov formula, Eq. (3.46), is still valid. The contact line velocity is calculated numerically, tracing shape and position of the contact line when marching in time, under the assumption that it always moves along its normal direction.

Chapter 4

Film flowing over 3D curved substrates

As mentioned, lubrication theory is used for optimizing a number of engineering problems, justifying such an interest from research world. However, the application of Eqs. (2.52) and (2.53) is still limited by some issues:

- Low liquid inertia, $\mathrm{Re} \leq 1$, must be assumed.
- Low equilibrium contact angles only can be investigated due to the small slope approximation.
- The formulation is limited to a thin layer of liquid flowing over a 2D substrate.

It is possible to extend lubrication theory for including inertia, as shown in chapter 2.6, but the formulation of the governing equations, which are again integrated across the film thickness, becomes much more complex as well as their solution. In fact, for a film flowing over a 2D plate the solution of momentum equations must be coupled with the solution of continuity equation, since the velocity components of the liquid are unknown as well as the film thickness. Since the used numerical method can not be adapted to such an analysis, we will focus here on extending the lubrication theory to the cases of equilibrium contact angle close to 90° and liquid flowing over a general 3D curved substrate. As it will be shown, this allows to investigate configurations, such as CO_2 absorption through structure packing, that have never been simulated using lubrication theory.

4.1 Continuity equation

Consider a reference Cartesian coordinate system $Oxyz$ containing the curved surface Γ and let α be the reference Oxy plane inclination with respect to the horizontal, as shown in figure 4.1. We can define a new 2D curvilinear coordinate system $O'\chi\eta$ by considering the traces, on the substrate surface Γ, of the planes $x = \text{const}$ and $y = \text{const}$. Let the angles α_χ and α_η define the

inclinations of the local coordinates χ and η to the Cartesian directions x and y. Let α^* be the angle in-between χ and η, the local coordinates $O'\chi\eta$ system being not orthogonal. Thus α^* is given by:

$$\alpha^* = \arccos\left(\sqrt{1 - \sin^2\alpha_\chi \, \sin^2\alpha_\eta}\right) \tag{4.1}$$

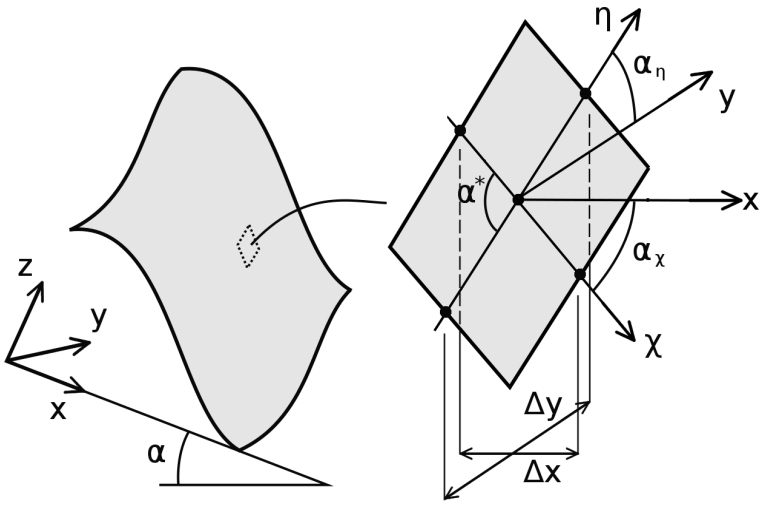

Figure 4.1: Control element of the curved surface Γ (locally approximated with its tangent plane) and definition of the local, non-orthogonal coordinates χ and η, obtained sectioning the substrate with two planes at $x = \text{const}$ and $y = \text{const}$.

Now consider a control volume of liquid $\Delta\chi \, \Delta\eta \, h$ standing on the curved substrate, as shown in figure 4.1. Assuming that the liquid flux $\boldsymbol{Q}$ is always tangent to the solid substrate (i.e. applying lubrication approximation), the film fluxes q and s along χ and η can be defined as,

$$q = \boldsymbol{Q} \cdot \hat{\boldsymbol{t}}_{\boldsymbol{\chi}}, \; s = \boldsymbol{Q} \cdot \hat{\boldsymbol{t}}_{\boldsymbol{\eta}} \tag{4.2}$$

$\hat{\boldsymbol{t}}_{\boldsymbol{\chi}}$ and $\hat{\boldsymbol{t}}_{\boldsymbol{\eta}}$ being the substrate tangential versors identifying χ and η direction respectively, which are defined in the reference $Oxyz$ Cartesian system as:

$$\hat{\boldsymbol{t}}_{\boldsymbol{\chi}} = (\cos\alpha_\chi, 0, \sin\alpha_\chi) \, , \; \hat{\boldsymbol{t}}_{\boldsymbol{\eta}} = (0, \cos\alpha_\eta, \sin\alpha_\eta) \tag{4.3}$$

Thus, the continuity equation offers:

$$\begin{aligned} \frac{\partial h}{\partial t} \Delta S = &- \left[\left(q \, \Delta\eta \, \sin\alpha^*\right)_{\chi + \frac{\Delta\chi}{2}} - \left(q \, \Delta\eta \, \sin\alpha^*\right)_{\chi - \frac{\Delta\chi}{2}} \right] \\ &- \left[\left(s \, \Delta\chi \, \sin\alpha^*\right)_{\eta + \frac{\Delta\eta}{2}} - \left(s \, \Delta\chi \, \sin\alpha^*\right)_{\eta - \frac{\Delta\eta}{2}} \right] \end{aligned} \tag{4.4}$$

with ΔS being the base element area:

$$\Delta S = \Delta\chi \, \Delta\eta \, \sin\alpha^* \tag{4.5}$$

The element dimensions $\Delta\chi$ and $\Delta\eta$ can be expressed as a function of the corresponding Cartesian coordinates x and y,

$$\Delta\chi = \frac{\Delta x}{\cos\alpha_\chi},\ \Delta\eta = \frac{\Delta y}{\cos\alpha_\eta} \tag{4.6}$$

that in fact still represents the independent variables, which the final governing equations are solved in.
Dividing both sides of Eq. (4.4) for ΔS and using Eq. (4.6) leads to:

$$\begin{aligned}\frac{\partial h}{\partial t} = &-\left[\left(q\frac{\sin\alpha^*}{\cos\alpha_\eta}\right)_{\chi+\frac{\Delta\chi}{2}} - \left(q\frac{\sin\alpha^*}{\cos\alpha_\eta}\right)_{\chi-\frac{\Delta\chi}{2}}\right]\frac{\Delta y}{\Delta S}\\ &-\left[\left(s\frac{\sin\alpha^*}{\cos\alpha_\chi}\right)_{\eta+\frac{\Delta\eta}{2}} - \left(s\frac{\sin\alpha^*}{\cos\alpha_\chi}\right)_{\eta-\frac{\Delta\eta}{2}}\right]\frac{\Delta x}{\Delta S}\end{aligned} \tag{4.7}$$

Introducing the following notation,

$$\frac{\partial f}{\partial\xi} \simeq \frac{f|_{\xi+\frac{\Delta\xi}{2}} - f|_{\xi-\frac{\Delta\xi}{2}}}{\Delta\xi} \tag{4.8}$$

the continuity equation, Eq. (4.7), can be easily rewritten as:

$$\frac{\partial h}{\partial t} + \frac{\cos\alpha_\eta}{\sin\alpha^*}\frac{\partial}{\partial\chi}\left(q\frac{\sin\alpha^*}{\cos\alpha_\eta}\right) + \frac{\cos\alpha_\chi}{\sin\alpha^*}\frac{\partial}{\partial\eta}\left(s\frac{\sin\alpha^*}{\cos\alpha_\chi}\right) = 0 \tag{4.9}$$

Eq. (4.9) represents the governing lubrication equation in case of a general bumped surface. The film fluxes q and s along χ and η direction respectively are needed. Note that the partial derivatives of the unknown film fluxes q, s should be expressed in terms of ∂_x and ∂_y through,

$$\frac{\partial}{\partial\chi} = \cos\alpha_\chi\frac{\partial}{\partial x} \tag{4.10}$$

$$\frac{\partial}{\partial\eta} = \cos\alpha_\eta\frac{\partial}{\partial y} \tag{4.11}$$

since x and y are the independent variables. However, it will be shown that the current notation is more suitable for describing the numerical implementation of equations such as Eq. (4.9).
Weidner et al. [27] also refers to the curvilinear coordinate standing on the curved substrate when studying the simpler case of a film flowing over a 2D curved surface. It can be verified that the proposed model reduces to the equation solved in [27] if the solid substrate where the thin layer of liquid evolves has a cylindrical geometry.

4.2 Momentum equation

The expression of the film fluxes to be used in Eq. (4.9) can be obtained from the solution of the momentum equation. Thus, consider a control volume of

liquid standing on the solid substrate, χ and η being the curvilinear coordinates and ζ defining the coordinate along the normal outward direction of the substrate. Assuming lubrication approximation,

$$\frac{\partial p}{\partial \zeta} = \rho\, g\, \hat{\boldsymbol{g}} \cdot \hat{\boldsymbol{n}}_{\boldsymbol{s}} \tag{4.12}$$

neglecting liquid inertia and imposing the balance of forces acting on the control volume of liquid along χ direction leads to,

$$\begin{aligned}
&\Big[p\,\Delta\eta\,\Delta\zeta\,\sin\alpha^*\Big]_{\chi+\frac{\Delta\chi}{2}} \cos\Big(\alpha_\chi|_{\chi+\frac{\Delta\chi}{2}} - \alpha_\chi|_{\chi}\Big) \\
-&\Big[p\,\Delta\eta\,\Delta\zeta\,\sin\alpha^*\Big]_{\chi-\frac{\Delta\chi}{2}} \cos\Big(\alpha_\chi|_{\chi} - \alpha_\chi|_{\chi-\frac{\Delta\chi}{2}}\Big) \\
+&\Big[p\,\Delta\chi\,\Delta\zeta\Big]_{\eta+\frac{\Delta\eta}{2}} \sin\Big(\alpha^*|_{\eta+\frac{\Delta\eta}{2}} - \alpha^*|_{\eta}\Big) \\
+&\Big[p\,\Delta\chi\,\Delta\zeta\Big]_{\eta-\frac{\Delta\eta}{2}} \sin\Big(\alpha^*|_{\eta} - \alpha^*|_{\eta-\frac{\Delta\eta}{2}}\Big) \\
=&\Big(\tau_{\chi\zeta}|_{\zeta+\Delta\zeta} - \tau_{\chi\zeta}|_{\zeta}\Big)\,\Delta S + \rho\, g\, \hat{\boldsymbol{g}} \cdot \hat{\boldsymbol{t}}_{\boldsymbol{\chi}}\,\Delta V
\end{aligned} \tag{4.13}$$

with:

- ΔS and ΔV defining the base surface and the inner volume of the control element of liquid:

$$\Delta V = \Delta\zeta\,\Delta S = \Delta\zeta\,\Delta\chi\,\Delta\eta\,\sin\alpha^* \tag{4.14}$$

- $\tau_{\chi\zeta}$, $\tau_{\eta\zeta}$ being the components of the shear stress matrix defined as:

$$\tau_{\chi\zeta} = \mu\,\frac{\partial u}{\partial \zeta},\; u = \boldsymbol{u} \cdot \hat{\boldsymbol{t}}_{\boldsymbol{\chi}} \tag{4.15}$$

$$\tau_{\eta\zeta} = \mu\,\frac{\partial v}{\partial \zeta},\; v = \boldsymbol{u} \cdot \hat{\boldsymbol{t}}_{\boldsymbol{\eta}} \tag{4.16}$$

- $\hat{\boldsymbol{g}}$ identifying the direction along which the gravitational acceleration acts;
- $\hat{\boldsymbol{t}}_{\boldsymbol{\chi},\boldsymbol{\eta}}$ being substrate tangential versors;
- $\hat{\boldsymbol{n}}_{\boldsymbol{s}}$ being the outward normal direction to the solid substrate.

The fist two terms of Eq. (4.13) represent the forces along χ given by the liquid pressure acting on the control element faces $\chi \pm \Delta\chi/2$. The third and the fourth terms of Eq. (4.13), which are also pressure forces, derive from the substrate curvature: since χ and η directions are defined locally, they may change from an element to the neighbour one, giving different value of α^* at the corresponding element faces. The terms at the RHS of Eq. (4.13) are the shear stress, due to liquid viscosity, and the gravity force. Note that the

driving gravity volume force $\rho\, g\, \hat{\boldsymbol{g}} \cdot \hat{\boldsymbol{t}}_{\boldsymbol{\chi}}$ is no more included in the liquid pressure p, as done in chapter 2 in order to ensure a more compact notation.
Introducing the following notation,

$$f(\xi)|_{\xi \pm \Delta\xi} \simeq f(\xi) \pm \frac{\partial f}{\partial \xi} \Delta\xi \tag{4.17}$$

knowing that for a sufficiently small ξ,

$$\cos\xi \xrightarrow{\xi \simeq 0} 1,\ \sin\xi \xrightarrow{\xi \simeq 0} \xi \tag{4.18}$$

and $\Delta\zeta$ being an independent variable, Eq. (4.13) can be rewritten as:

$$\begin{aligned} &\frac{\partial}{\partial \chi}\Big(p\, \Delta\eta\, \sin\alpha^*\Big)\, \Delta\chi\, \Delta\zeta + \Big(p\, \Delta\chi\Big) \left(\frac{\partial \alpha^*}{\partial \eta} \Delta\eta\right) \Delta\zeta \\ &= \left(\frac{\partial \tau_{\chi\zeta}}{\partial \zeta}\, \Delta\zeta\right) \Delta\chi\, \Delta\eta\, \sin\alpha^* + \rho\, g\, \hat{\boldsymbol{g}} \cdot \hat{\boldsymbol{t}}_{\boldsymbol{\chi}}\, \Delta\zeta\, \Delta\chi\, \Delta\eta\, \sin\alpha^* \end{aligned} \tag{4.19}$$

Dividing both sides of Eq. (4.19) for ΔV and expressing $\tau_{\chi\zeta}$ according to Eq. (4.15), the momentum equation finally gives:

$$\frac{\cos\alpha_\eta}{\sin\alpha^*} \frac{\partial}{\partial \chi} \left(p\, \frac{\sin\alpha^*}{\cos\alpha_\eta}\right) + \frac{p}{\sin\alpha^*} \frac{\partial \alpha^*}{\partial \eta} = \rho\, g\, \boldsymbol{g} \cdot \hat{\boldsymbol{t}}_{\boldsymbol{\chi}} + \mu\, \frac{\partial^2 u}{\partial \zeta^2} \tag{4.20}$$

Eq. (4.20) can be integrated, looking for the velocity profile $u(\zeta)$ across the film thickness. Applying non-slip condition at the substrate, introducing the shear applied by the external gas flow,

$$\boldsymbol{\tau_g} = \left\{ \begin{matrix} \boldsymbol{\tau_g} \cdot \hat{\boldsymbol{t}}_{\boldsymbol{\chi}} \\ \boldsymbol{\tau_g} \cdot \hat{\boldsymbol{t}}_{\boldsymbol{\eta}} \end{matrix} \right\} = \left\{ \begin{matrix} \tau_\chi \\ \tau_\eta \end{matrix} \right\} \tag{4.21}$$

and and imposing $\boldsymbol{\tau_g}$ at the free-surface,

$$u|_0 = 0,\ \left.\frac{\partial u}{\partial \zeta}\right|_h = \tau_\chi \tag{4.22}$$

the following parabolic profile can be obtained:

$$\begin{aligned} u = &\frac{\rho\, g}{\mu}\, \hat{\boldsymbol{g}} \cdot \hat{\boldsymbol{t}}_{\boldsymbol{\chi}} \left(h\, \zeta - \frac{\zeta^2}{2}\right) + \frac{\tau_\chi}{\mu}\, \zeta \\ &- \frac{1}{\mu} \left[\frac{\cos\alpha_\eta}{\sin\alpha^*} \frac{\partial}{\partial \chi} \left(p\, \frac{\sin\alpha^*}{\cos\alpha_\eta}\right) + \frac{p}{\sin\alpha^*} \frac{\partial \alpha^*}{\partial \eta}\right] \left(h\, \zeta - \frac{\zeta^2}{2}\right) \end{aligned} \tag{4.23}$$

Integrating the velocity profile $u(\zeta)$ across the film thickness h finally gives the film flux q along χ direction:

$$q = \frac{\rho\, g\, h^3}{3\, \mu}\, \hat{\boldsymbol{g}} \cdot \hat{\boldsymbol{t}}_{\boldsymbol{\chi}} + \frac{\tau_\chi\, h^2}{2\, \mu} - \left[\frac{\cos\alpha_\eta}{\sin\alpha^*} \frac{\partial}{\partial \chi} \left(p\, \frac{\sin\alpha^*}{\cos\alpha_\eta}\right) + \frac{p}{\sin\alpha^*} \frac{\partial \alpha^*}{\partial \eta}\right] \frac{h^3}{3\, \mu} \tag{4.24}$$

The same procedure can be applied for calculating the film flux s along η direction, leading to:

$$s = \frac{\rho\, g\, h^3}{3\, \mu}\, \hat{\boldsymbol{g}} \cdot \hat{\boldsymbol{t}}_{\boldsymbol{\eta}} + \frac{\tau_\eta\, h^2}{2\, \mu} - \left[\frac{\cos\alpha_\chi}{\sin\alpha^*} \frac{\partial}{\partial \eta} \left(p\, \frac{\sin\alpha^*}{\cos\alpha_\chi}\right) + \frac{p}{\sin\alpha^*} \frac{\partial \alpha^*}{\partial \chi}\right] \frac{h^3}{3\, \mu} \tag{4.25}$$

4.3 Pressure field

The pressure field is given by hydrostatic, capillary and disjoining contributes,

$$p = -\rho\, g\, h\, \hat{\boldsymbol{n}}_{\boldsymbol{s}} \cdot \hat{\boldsymbol{g}} - 2\,\sigma\,(\kappa_m + \kappa_s) - \Pi \tag{4.26}$$

$\hat{\boldsymbol{n}}_{\boldsymbol{s}}$ being the substrate outward normal direction, κ_m and κ_s being the relative free-surface curvature (calculated with respect to the local coordinates χ, η) and the substrate curvature respectively.
It is important to point out that the contribute given by the substrate curvature κ_s must be taken into account when calculating the capillary pressure. The disjoining pressure Π is still given by Eq. (2.21).
Since we want to investigate the general case of a film flowing over a solid curved substrate with equilibrium contact angle close to 90°, small slope approximation must be abandoned in favor of a more realistic model, in order to correctly estimate the free-surface curvature κ_m.

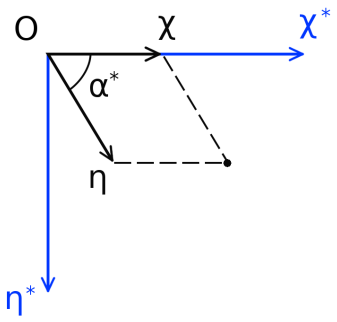

Figure 4.2: Definition of the local, orthogonal coordinates χ^* and η^* on the solid substrate, needed for free-surface curvature calculation.

The straight implementation of Eq. (2.19), which expresses the mean curvature of a curved surface $h(x, y)$ in a given orthogonal coordinate system, is quite trivial for some reasons:

- The term of Eq. (2.19) arising from the mist derivatives of h, given by $\frac{\partial^2 h}{\partial x \partial y}$, can not be treated implicitly using the ADI factorization of Witelski et al. [13]. Moreover, both the numerical stability of the computed solution and its accuracy in time may decrease if you simply treat it explicitly.

- Eq. (2.19) is valid when the coordinate system is orthogonal, but the local coordinate χ and η standing on the solid substrate are not orthogonal, making the calculation of the curvature even more difficult to implement. Referring to the local, orthogonal 2D coordinate system $O\chi^*\eta^*$, shown in figure 4.2, the relative curvature of the free-surface can be still calculated through Eq. (2.19):

$$2\,\kappa_m = \frac{\frac{\partial^2 h}{\partial \chi^{*2}}\left[1 + \left(\frac{\partial h}{\partial \eta^*}\right)^2\right] + \frac{\partial^2 h}{\partial \eta^{*2}}\left[1 + \left(\frac{\partial h}{\partial \chi^*}\right)^2\right] - 2\,\frac{\partial h}{\partial \chi^*}\frac{\partial h}{\partial \eta^*}\frac{\partial^2 h}{\partial \chi^* \partial \eta^*}}{\left[1 + \left(\frac{\partial h}{\partial \chi^*}\right)^2 + \left(\frac{\partial h}{\partial \eta^*}\right)^2\right]^{3/2}} \tag{4.27}$$

Assuming that α^* keeps locally uniform over the solid substrate (meaning that the substrate is locally approximated with its tangent plane), χ^* and η^* coordinates are given by,

$$\begin{cases} \chi^* = \chi + \eta \cos\alpha^* \\ \eta^* = \eta \sin\alpha^* \end{cases} \tag{4.28}$$

allowing for a sensible simplification in the free-surface curvature computation. In fact, substituting

$$\begin{cases} \dfrac{\partial}{\partial\chi^*} = \dfrac{\partial}{\partial\chi} \\ \dfrac{\partial}{\partial\eta^*} = \dfrac{1}{\tan\alpha^*}\dfrac{\partial}{\partial\chi} + \dfrac{1}{\sin\alpha^*}\dfrac{\partial}{\partial\eta} \end{cases} \tag{4.29}$$

in Eq. (4.27), the free-surface curvature can be calculated as:

$$2\,\kappa_m = \sin\alpha^* \frac{\frac{\partial^2 h}{\partial\chi^2}\left[1+\left(\frac{\partial h}{\partial\eta}\right)^2\right] + \frac{\partial^2 h}{\partial\eta^2}\left[1+\left(\frac{\partial h}{\partial\chi}\right)^2\right] - 2\frac{\partial^2 h}{\partial\chi\partial\eta}\left(\frac{\partial h}{\partial\chi}\frac{\partial h}{\partial\eta} - \cos\alpha^*\right)}{\left[\sin^2\alpha^* + \left(\frac{\partial h}{\partial\chi}\right)^2 + \left(\frac{\partial h}{\partial\eta}\right)^2 + 2\cos\alpha^*\frac{\partial h}{\partial\chi}\frac{\partial h}{\partial\eta}\right]^{3/2}} \tag{4.30}$$

As mentioned before, the mist derivative $\frac{\partial^2 h}{\partial\chi\partial\eta}$ arising in Eq. (4.30) can not be treated implicitly using the current ADI factorization. Thus, an approximate procedure was implemented for estimating free-surface curvature.

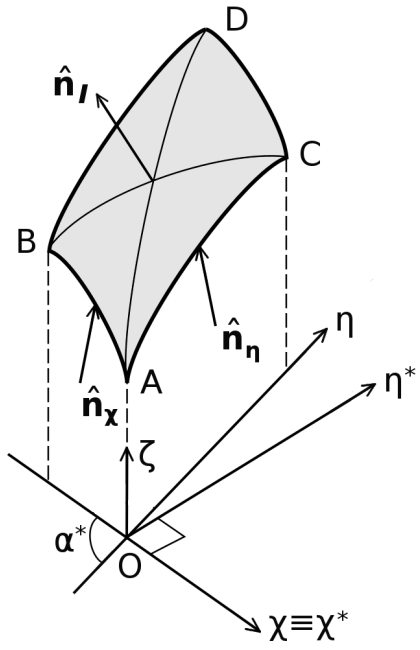

Figure 4.3: Portion of free-surface obtained sectioning with $O\chi\zeta$ and $O\eta\zeta$ planes, AB, AC, CD and BD being the free boundaries of the surface element.

Cutting the free-surface by means of two planes Γ_χ and Γ_η, normal to the solid substrate and passing through $\chi = \text{const}$ and $\eta = \text{const}$ ($\Gamma_{\chi,\eta}$ are identified

by $O\chi\zeta$ and $O\eta\zeta$ in figure 4.3), the following curvatures can be calculated according to Young-Laplace equation:

$$\frac{1}{r_\chi} = \frac{\frac{\partial^2 h}{\partial \chi^2}}{\left[1 + \left(\frac{\partial h}{\partial \chi}\right)^2\right]^{3/2}} \tag{4.31}$$

$$\frac{1}{r_\eta} = \frac{\frac{\partial^2 h}{\partial \eta^2}}{\left[1 + \left(\frac{\partial h}{\partial \eta}\right)^2\right]^{3/2}} \tag{4.32}$$

Applying Meusnier theorem, the calculated curvatures $1/r_\chi$ and $1/r_\eta$ can be reconduced to the corresponding curvatures along free-surface normal direction. These curvatures are used for estimating the mean free-surface curvature,

$$2\,\kappa_m \simeq \frac{1}{r_\chi}\,\hat{\boldsymbol{n}}_{\boldsymbol{\chi}} \cdot \hat{\boldsymbol{n}}_{\boldsymbol{I}} + \frac{1}{r_\eta}\,\hat{\boldsymbol{n}}_{\boldsymbol{\eta}} \cdot \hat{\boldsymbol{n}}_{\boldsymbol{I}} \tag{4.33}$$

$\hat{\boldsymbol{n}}_{\boldsymbol{\chi},\boldsymbol{\eta}}$ being the normal outward directions to the free boundaries AB and AC, $\hat{\boldsymbol{n}}_{\boldsymbol{I}}$ being the free-surface outward normal direction.
According to figure 4.3, the versors $\hat{\boldsymbol{n}}_{\boldsymbol{\chi},\boldsymbol{\eta}}$ and $\hat{\boldsymbol{n}}_{\boldsymbol{I}}$ can be computed in the local orthogonal coordinate system $O\chi^*\eta^*\zeta$ with the following procedure:

$$\begin{cases} \hat{\boldsymbol{n}}_{\boldsymbol{I}} \cdot \overrightarrow{AB} = 0 \\ \hat{\boldsymbol{n}}_{\boldsymbol{I}} \cdot \overrightarrow{AC} = 0 \\ |\hat{\boldsymbol{n}}_{\boldsymbol{I}}| = 1 \end{cases} ; \begin{cases} \hat{\boldsymbol{n}}_{\boldsymbol{\chi}} = (a, 0, b) \\ \hat{\boldsymbol{n}}_{\boldsymbol{\chi}} \cdot \overrightarrow{AB} = 0 \\ |\hat{\boldsymbol{n}}_{\boldsymbol{\chi}}| = 1 \end{cases} ; \begin{cases} \hat{\boldsymbol{n}}_{\boldsymbol{\eta}} = (a\,\cos\alpha^*, a\,\sin\alpha^*, b) \\ \hat{\boldsymbol{n}}_{\boldsymbol{\eta}} \cdot \overrightarrow{AC} = 0 \\ |\hat{\boldsymbol{n}}_{\boldsymbol{\eta}}| = 1 \end{cases} \tag{4.34}$$

The procedure can be adapted to any orthogonal system tangent to the solid substrate in O, the current system $O\chi^*\eta^*\zeta$, see figure 4.3, just being the most suitable for the algebraic solution of Eq. (4.34).
Note that Eq. (4.33) does not provide the exact calculation of the mean curvature, since the curvatures we reconduce to can be obtained cutting the free-surface using two planes that are orthogonal to the free-surface but not to each other. Referring to figure 4.3, Eq. (4.33) reduces to the real value of the mean curvature,

$$2\,\kappa_m = \frac{1}{r_1} + \frac{1}{r_2} \tag{4.35}$$

when $\overrightarrow{AB}$ and $\overrightarrow{AC}$ are almost orthogonal, i.e. the element of free-surface is not *stretched*.
Before its implementation in the solver code, Eq. (4.33) was tested for two different surfaces standing on a flat substrate, chosen as representative cases of thin liquid layer evolution:

- Stationary drop on a horizontal surface;
- Analytical solution of Duffy et al. [4], which is obtained solving the evolution of a liquid rivulet, as described in chapter 2.4.

Since a tiny drop standing on a flat surface tends to arrange in a spherical shape (if the hydrostatic pressure is negligible with respect to capillary pressure), the curvature of a portion of sphere was computed using both Eqs. (4.33) and (2.19), resulting in a perfect matching. Thanks to the symmetry properties of a sphere, every normal sectioning plane always gives the same value of the radius of curvature, thus no error occurs computing the curvature with Eq. (4.33).
Using an analytical approach, the authors of [4] were able to give a closed solution, Eqs. (2.77), (2.81) and (2.82), in case of a liquid flux entering through a small inlet section and arranging as a stable rivulet over an inclined plate driven by gravity. A typical test case occurring in the literature work of Singh et al. [12], that involves absorption/distillation process through structured packing, is considered. It is important to point out that the analytical solution of [4] does not fit satisfactory the numerical results of [12], which model is validated with several experimental evidences, but it serves to describe the qualitative behavior of the liquid. This is enough to verify the consistence of Eq. (4.33).

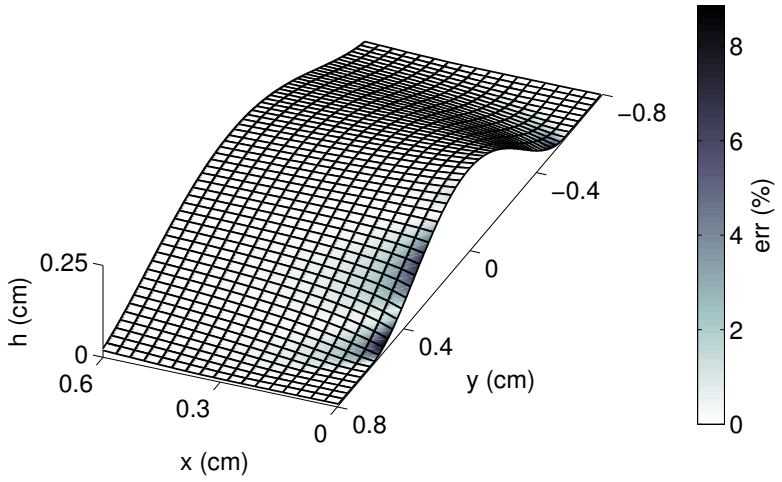

Figure 4.4: Error % between real curvature and Eq. (4.33) over the corresponding rivulet distribution on the inclined plate from analytical solution of [4]. $\rho = 981.31\,\mathrm{kg/m^3}$, $\mu = 0.03642\,\mathrm{Pa\,s}$, $\sigma = 0.0384\,\mathrm{N/m}, \alpha = 60°$.

The liquid distribution predicted through the analytical solution of [4] in the developing region of the rivulet, where the liquid flow is still 2D, is shown in figure 4.4 (continuous black lines). The case of $\lambda = 2$ is considered, λ being the free parameter that defines the rivulet shape, as described in chapter 2.4. Due to the singularity arising at the top of the plate, where the inlet section reduces to a point according to the analytical solution of [4], the plotted solution starts from $x_0 = 1\,\mathrm{mm}$ in order to guarantee a finite inlet section as it happens in real problems.
Since the solid substrate is an inclined plate for such a setup, the local co-

ordinates χ, η always overlap the Cartesian coordinates x, y and Eq. (4.33) reduces to:

$$2\,\kappa_m \simeq \frac{1}{r_x}\,\hat{\boldsymbol{n}}_{\boldsymbol{x}} \cdot \hat{\boldsymbol{n}}_{\boldsymbol{I}} + \frac{1}{r_y}\,\hat{\boldsymbol{n}}_{\boldsymbol{y}} \cdot \hat{\boldsymbol{n}}_{\boldsymbol{I}} \tag{4.36}$$

The discrepancy between the real curvature $\kappa_{m,real}$, Eq. (2.19), and the approximated curvature $\kappa_{m,appr}$, Eq. (4.36), is computed as,

$$err = 100 \left| \frac{\kappa_{m,appr} - \kappa_{m,real}}{l_c} \right| \tag{4.37}$$

l_c being the capillary length,

$$l_c = \sqrt{\frac{\sigma}{\rho\, g}} \tag{4.38}$$

which is used as the reference radius of curvature. For such a setup, the maximum rivulet height, that may also be chosen as reference length, and the capillary length assume similar values.
Figure 4.4, in which the error is plotted over the inclined plate, shows that Eq. (4.36) is able to model the free-surface curvature within a maximum error of 9.16% close to the inlet section. Figure 4.4 also allows to understand the regions of the free-surface where the higher discrepancy occurs, since both the liquid distribution and the error of the computed curvature are plotted. The error is also computed estimating the free-surface curvature by means of the small slope approximation, Eq. (2.20). A similar trend is obtained, but the maximum error is about 5.02 times the one obtained modelling the curvature with Eq. (4.37). Thus, the new model is much more precise compared to small slope approximation.

4.4 Numerical method

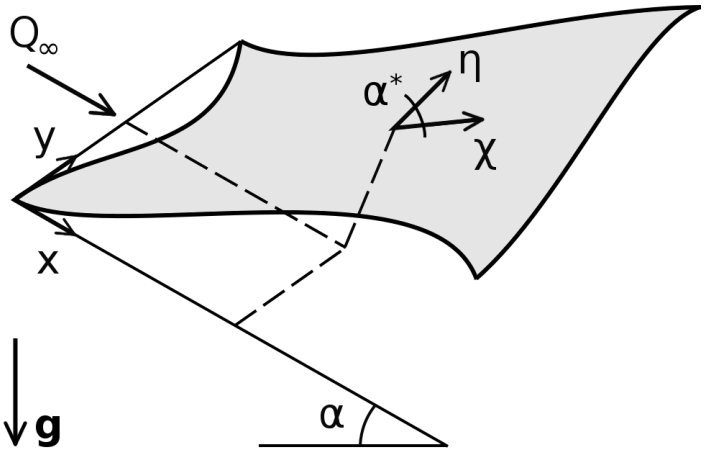

Figure 4.5: Problem definition: inclined reference plane Oxy, substrate surface and local coordinates χ, η.

The FVM solver is modified in order to solve the new governing equations describing the evolution of a thin liquid layer over a curved substrate, characterized by equilibrium contact angle up to 90°. Defining the local coordinates χ and η according to figures 4.1 and 4.5 and the normal outward versor $\hat{\boldsymbol{n}}_{\boldsymbol{I}}$ according to figure 4.3, the governing equations, Eqs. (4.9), (4.24), (4.25) and (4.26), were obtained.
Introducing the undisturbed film thickness h_∞ and velocity u_∞, which meaning will be explained in the next section, the following non-dimensional quantities can be defined:

$$\tilde{\chi} = \frac{\chi}{h_\infty},\ \tilde{\eta} = \frac{\eta}{h_\infty},\ \tilde{h} = \frac{h}{h_\infty},\ \tilde{\kappa}_m = h_\infty\,\kappa_m \tag{4.39}$$

$$\tilde{q} = \frac{q}{(\sigma\, h_\infty/\mu)},\ \tilde{s} = \frac{s}{(\sigma\, h_\infty/\mu)},\ \tilde{t} = \frac{t}{(\mu\, h_\infty/\sigma)} \tag{4.40}$$

$$\tilde{p} = \frac{p}{(\sigma/h_\infty)},\ \tilde{\Pi} = \frac{\Pi}{(\sigma/h_\infty)},\ \tilde{\boldsymbol{\tau}}_{\boldsymbol{g}} = \frac{\boldsymbol{\tau}_{\boldsymbol{g}}}{(\mu\, u_\infty/h_\infty)} \tag{4.41}$$

$$\mathrm{Bo} = \frac{\rho\, g\, h_\infty}{\sigma},\ \mathrm{Ca} = \frac{\mu\, u_\infty}{\sigma} \tag{4.42}$$

Thus, the governing equations can be rearranged in a non-dimensional form,

$$\frac{\partial \tilde{h}}{\partial \tilde{t}} + \frac{\cos\alpha_\eta}{\sin\alpha^*}\frac{\partial}{\partial\tilde{\chi}}\left(\tilde{q}\,\frac{\sin\alpha^*}{\cos\alpha_\eta}\right) + \frac{\cos\alpha_\chi}{\sin\alpha^*}\frac{\partial}{\partial\tilde{\eta}}\left(\tilde{s}\,\frac{\sin\alpha^*}{\cos\alpha_\chi}\right) = 0 \tag{4.43}$$

$$\tilde{q} = \frac{\mathrm{Bo}\,\tilde{h}^3}{3}\hat{\boldsymbol{g}}\cdot\hat{\boldsymbol{t}}_{\boldsymbol{\chi}} + \frac{\mathrm{Ca}\,\tilde{\tau}_\chi\,\tilde{h}^2}{2} - \left[\frac{\cos\alpha_\eta}{\sin\alpha^*}\frac{\partial}{\partial\tilde{\chi}}\left(\tilde{p}\,\frac{\sin\alpha^*}{\cos\alpha_\eta}\right) + \frac{\tilde{p}}{\sin\alpha^*}\frac{\partial\alpha^*}{\partial\tilde{\eta}}\right]\frac{\tilde{h}^3}{3} \tag{4.44}$$

$$\tilde{s} = \frac{\mathrm{Bo}\,\tilde{h}^3}{3}\hat{\boldsymbol{g}}\cdot\hat{\boldsymbol{t}}_{\boldsymbol{\eta}} + \frac{\mathrm{Ca}\,\tilde{\tau}_\eta\,\tilde{h}^2}{2} - \left[\frac{\cos\alpha_\chi}{\sin\alpha^*}\frac{\partial}{\partial\tilde{\eta}}\left(\tilde{p}\,\frac{\sin\alpha^*}{\cos\alpha_\chi}\right) + \frac{\tilde{p}}{\sin\alpha^*}\frac{\partial\alpha^*}{\partial\tilde{\chi}}\right]\frac{\tilde{h}^3}{3} \tag{4.45}$$

$$\tilde{p} = -\mathrm{Bo}\,\tilde{h}\,\hat{\boldsymbol{g}}\cdot\hat{\boldsymbol{n}}_{\boldsymbol{s}} - 2\,(\tilde{\kappa}_m + \tilde{\kappa}_s) - \tilde{\Pi} \tag{4.46}$$

the mean curvature $\tilde{\kappa}_m$ of the free-surface being computed as:

$$2\,\tilde{\kappa}_m = \frac{1}{\tilde{r}_\chi}\,\hat{\boldsymbol{n}}_{\boldsymbol{\chi}}\cdot\hat{\boldsymbol{n}}_{\boldsymbol{I}} + \frac{1}{\tilde{r}_\eta}\,\hat{\boldsymbol{n}}_{\boldsymbol{\eta}}\cdot\hat{\boldsymbol{n}}_{\boldsymbol{I}} \tag{4.47}$$

$$\frac{1}{\tilde{r}_\chi} = \frac{\frac{\partial^2\tilde{h}}{\partial\tilde{\chi}^2}}{\left[1+\left(\frac{\partial\tilde{h}}{\partial\tilde{\chi}}\right)^2\right]^{3/2}},\ \frac{1}{\tilde{r}_\eta} = \frac{\frac{\partial^2\tilde{h}}{\partial\tilde{\eta}^2}}{\left[1+\left(\frac{\partial\tilde{h}}{\partial\tilde{\eta}}\right)^2\right]^{3/2}} \tag{4.48}$$

A structured, orthogonal grid composed by $n_i \times n_j$ elements of variable size defines the reference Oxy plane of dimensions $L_x \times L_y$, the gravity versor $\hat{\boldsymbol{g}}$ depending on the reference plane inclination with respect of the horizontal. The i,j-th element of the curved substrate, with $i \in [1, n_i]$ and $j \in [1, n_j]$, is defined by four neighbour nodes, as shown in figure 4.6, the k-th node being identified by its corresponding height $z_k = z(x_k, y_k)$ across normal outward direction of the reference inclined plane Oxy. It derives that the curved substrate is discretized by means of a structured, but non-orthogonal grid (α^* being the angle between the local coordinates χ and η), with the properties at

each element centroid being univocally connected to the corresponding nodes value through a linear interpolation:

$$x_i = \sum_{k=1}^{4} \frac{x_{n_k}}{4},\; y_j = \sum_{k=1}^{4} \frac{y_{n_k}}{4},\; z_{i,j} = \sum_{k=1}^{4} \frac{z_{n_k}}{4} \tag{4.49}$$

Such an approach allows to adapt the FVM code, developed in `FORTRAN` for solving the simpler case of a film flowing over an inclined plate. Thus, the 2D mathematical approach is kept and the ADI method described in chapter 3.2 is still applied thanks to the structured nature of the computational grid, leading to limited computational costs compared to fully 3D simulations of two-phase flow.

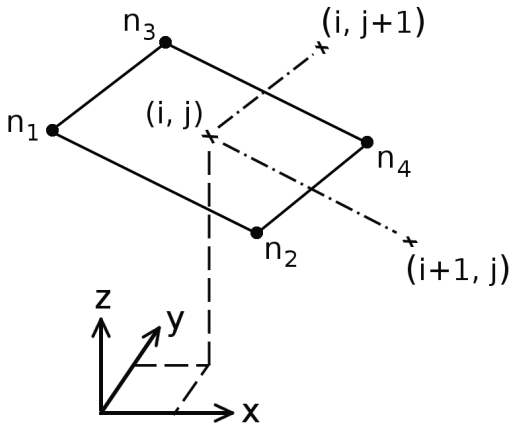

Figure 4.6: Structured computational grid: nodes n_k, $k = 1, 2, 3, 4$, defining the i, j-th control surface element.

The fluxes q and s defining $\boldsymbol{Q} = (q, s)$ are still discretized by means of a first order upwind scheme and decomposed into two contributions defining the positive and negative film propagation. Referring to χ direction only, the non-dimensional flux $\tilde{q}^{+}$ through the $i + \frac{1}{2}, j$-th face of the i, j-th element of the computational grid is implemented as,

$$\begin{aligned} \tilde{q}^{+}_{i,j} = & \frac{\mathrm{Bo}\,\tilde{h}^3_{i,j}}{3}\,\hat{\boldsymbol{g}}\cdot\hat{\boldsymbol{t}}_{\boldsymbol{\chi}\,i,j} + \frac{\mathrm{Ca}\,\tilde{\tau}_{\chi\,i,j}\,\tilde{h}^2_{i,j}}{2} - \frac{\tilde{p}_{i,j}}{\sin\alpha^*_{i,j}}\left.\frac{\partial\alpha^*}{\partial\tilde{\eta}}\right|_{i,j}\frac{\tilde{h}^3_{i,j}}{3} \\ & - \left[\left.\frac{\cos\alpha_\eta}{\sin\alpha^*}\right|_{i+\frac{1}{2},j}\frac{\partial}{\partial\tilde{\chi}}\left(\tilde{p}\,\frac{\sin\alpha^*}{\cos\alpha_\eta}\right)\right|_{i+\frac{1}{2},j}\right]\frac{\tilde{h}^3_{i,j}}{3} \end{aligned} \tag{4.50}$$

where:

- the pseudo-pressure gradient at the $i + \frac{1}{2}, j$-th element face is evaluated as,

$$\left.\frac{\partial}{\partial\tilde{\chi}}\left(\tilde{p}\,\frac{\sin\alpha^*}{\cos\alpha_\eta}\right)\right|_{i+\frac{1}{2},j} \simeq \frac{\tilde{p}_{i+1,j}\left.\frac{\sin\alpha^*}{\cos\alpha_\eta}\right|_{i+1,j} - \tilde{p}_{i,j}\left.\frac{\sin\alpha^*}{\cos\alpha_\eta}\right|_{i,j}}{\Delta\tilde{\chi}_{i+\frac{1}{2},j}} \tag{4.51}$$

with α^* and α_η being evaluated at the centroids of i,j-th and $i+1,j$-th elements using the corresponding values at the nodes defining each element (as it will be soon explained), the non-dimensional spatial discretization step $\Delta\tilde{\chi}_{i+\frac{1}{2},j}$ being equal to:

$$\Delta\tilde{\chi}_{i+\frac{1}{2},j} = \sqrt{\left(\tilde{x}_{i+1} - \tilde{x}_i\right)^2 + \left(\tilde{z}_{i+1,j} - \tilde{z}_{i,j}\right)^2} \tag{4.52}$$

- the free-surface inclination $\alpha_{\eta_{i+\frac{1}{2},j}}$ is computed from the known substrate height z at the two nodes defining the $i+\frac{1}{2},j$-th element face according to figure 4.6:

$$\alpha_{\eta_{i+\frac{1}{2},j}} = \arctan\left(\frac{z_{n_4} - z_{n_2}}{y_{n_4} - y_{n_2}}\right) \tag{4.53}$$

- the angle ${\alpha^*}_{i+\frac{1}{2},j}$ between χ and η directions is evaluated through the values of z at the nodes defining the $i+\frac{1}{2}$-th element face and at the $i\pm1,j$-th element centroids:

$$\alpha_{\chi_{i+\frac{1}{2},j}} = \arctan\left(\frac{z_{i+1,j} - z_{i,j}}{x_{i+1} - x_i}\right) \tag{4.54}$$

$${\alpha^*}_{i+\frac{1}{2},j} = \arccos\sqrt{1 - \sin^2\alpha_{\chi_{i+\frac{1}{2},j}}\,\sin^2\alpha_{\eta_{i+\frac{1}{2},j}}} \tag{4.55}$$

- the multiplying prefactors $\tilde{h}^2$ and $\tilde{h}^3$, the gravity driving force along χ direction $\hat{\boldsymbol{g}}\cdot\hat{\boldsymbol{t}}_{\boldsymbol{\chi}}$ and the shear of the external gas flow $\tilde{\tau}_\chi$, which are needed from Eq. (4.50) for film flux calculation, are evaluated at the element centroid, according to upwinding, as well as the novel pressure force arising from the substrate curvature effect:

$$\frac{\tilde{p}}{\sin\alpha^*}\,\frac{\partial\alpha^*}{\partial\tilde{\eta}} \tag{4.56}$$

Thus, the expressions of the fluxes $\tilde{q}^+_{i,j}$ and $\tilde{q}^-_{i,j}$ allows to treat the pseudo-pressure gradient with a centered scheme. It derives that the second order derivative of the pressure field,

$$\frac{\partial}{\partial\tilde{\chi}}\left[\frac{\partial}{\partial\tilde{\chi}}\left(\tilde{p}\,\frac{\sin\alpha^*}{\cos\alpha_\eta}\right)\,\frac{\tilde{h}^3}{3}\right] \tag{4.57}$$

resulting from the governing equations, Eqs. (4.43) and (4.44), is still treated with a second order centered scheme, keeping unchanged the numerical scheme developed for the simpler case of film flowing over an inclined plate.
The net fluxes crossing the i,j-th element faces are still given by Eqs. (3.12) and (3.13). Using finite volume notation, the face integral of the fluxes through the element boundaries is given by,

$$\begin{aligned}\frac{1}{\Delta\tilde{S}_{i,j}}\int_{\Omega_{i,j}}\tilde{\boldsymbol{Q}}\cdot\hat{\boldsymbol{n}}\,d\Omega = &\frac{\tilde{q}_{i+\frac{1}{2},j}\left[\Delta\tilde{\eta}\,\sin\alpha^*\right]_{i+\frac{1}{2},j} - \tilde{q}_{i-\frac{1}{2},j}\left[\Delta\tilde{\eta}\,\sin\alpha^*\right]_{i-\frac{1}{2},j}}{\Delta\tilde{S}_{i,j}}\\ &- \frac{\tilde{s}_{i,j+\frac{1}{2}}\left[\Delta\tilde{\chi}\,\sin\alpha^*\right]_{i,j+\frac{1}{2}} - \tilde{s}_{i,j-\frac{1}{2}}\left[\Delta\tilde{\chi}\,\sin\alpha^*\right]_{i,j-\frac{1}{2}}}{\Delta\tilde{S}_{i,j}}\end{aligned} \tag{4.58}$$

where:

- the dimensions of the element faces $\Delta\chi_{i,j\pm\frac{1}{2}}$, $\Delta\eta_{i\pm\frac{1}{2},j}$ are computed from the substrate height at the nodes of the i,j-th element,

$$\Delta\tilde{\chi}_{i,j-\frac{1}{2}} = \sqrt{(\tilde{z}_{n_2} - \tilde{z}_{n_1})^2 + (\tilde{x}_{n_2} - \tilde{x}_{n_1})^2} \tag{4.59}$$

$$\Delta\tilde{\chi}_{i,j+\frac{1}{2}} = \sqrt{(\tilde{z}_{n_4} - \tilde{z}_{n_3})^2 + (\tilde{x}_{n_4} - \tilde{x}_{n_3})^2} \tag{4.60}$$

$$\Delta\tilde{\eta}_{i-\frac{1}{2},j} = \sqrt{(\tilde{z}_{n_3} - \tilde{z}_{n_1})^2 + (\tilde{y}_{n_3} - \tilde{y}_{n_1})^2} \tag{4.61}$$

$$\Delta\tilde{\eta}_{i+\frac{1}{2},j} = \sqrt{(\tilde{z}_{n_4} - \tilde{z}_{n_2})^2 + (\tilde{y}_{n_4} - \tilde{y}_{n-2})^2} \tag{4.62}$$

  with n_k, $\forall\, k = 1,\ 2,\ 3,\ 4$, being defined in figure 4.6.

- the substrate element surface $\Delta S_{i,j}$ is given by:

$$\Delta\tilde{S}_{i,j} = \frac{\Delta\tilde{x}_i}{\cos\alpha_{\chi\,i,j}}\,\frac{\Delta\tilde{y}_j}{\cos\alpha_{\eta\,i,j}}\,\sin\alpha^*_{i,j} \tag{4.63}$$

- the angles ${\alpha^*}_{i,j}$ and $\alpha_{\chi,\eta\,i,j}$ are always computed from the known substrate height z at the nodes defining each element of the computational grid according to figure 4.6, ensuring a sufficient accuracy:

$$\alpha_{\chi i,j} = \arctan\left(\frac{1}{2}\,\frac{z_{n_2} - z_{n_1}}{x_{n_2} - x_{n_1}} + \frac{1}{2}\,\frac{z_{n_4} - z_{n_3}}{x_{n_4} - x_{n_3}}\right) \tag{4.64}$$

$$\alpha_{\eta i,j} = \arctan\left(\frac{1}{2}\,\frac{z_{n_3} - z_{n_1}}{y_{n_3} - y_{n_1}} + \frac{1}{2}\,\frac{z_{n_4} - z_{n_2}}{y_{n_4} - y_{n_2}}\right) \tag{4.65}$$

$${\alpha^*}_{i,j} = \arccos\sqrt{1 - \sin^2\alpha_{\chi i,j}\,\sin^2\alpha_{\eta i,j}} \tag{4.66}$$

Attention must be paid on the implementation of the capillary pressure, Eqs. (4.47) and (4.48). The expression of $1/\tilde{r}_\chi$ depending on $\frac{\partial^2\tilde{h}}{\partial\tilde{\chi}^2}$ and $\frac{\partial\tilde{h}}{\partial\tilde{\chi}}$, the following second order centered scheme was implemented for the partial derivatives of h needed for computation of the mean curvature κ_m,

$$\left.\frac{\partial^2\tilde{h}}{\partial\tilde{\chi}^2}\right|_{i,j} \simeq a_{i,j,1}\,\tilde{h}_{i-1,j} + a_{i,j,2}\,\tilde{h}_{i,j} + a_{i,j,3}\,\tilde{h}_{i+1,j} \tag{4.67}$$

$$\left.\frac{\partial\tilde{h}}{\partial\tilde{\chi}}\right|_{i,j} \simeq b_{i,j,1}\,\tilde{h}_{i-1,j} + b_{i,j,2}\,\tilde{h}_{i,j} + b_{i,j,3}\,\tilde{h}_{i+1,j} \tag{4.68}$$

with the coefficients $a_{i,j,1-3}$ being defined as,

$$a_{i,j,1} = 2\,\left[\Delta\tilde{\chi}_{i-\frac{1}{2},j}\left(\Delta\tilde{\chi}_{i-\frac{1}{2},j} + \Delta\tilde{\chi}_{i+\frac{1}{2},j}\right)\right]^{-1} \tag{4.69}$$

$$a_{i,j,2} = -2\,\left[\Delta\tilde{\chi}_{i-\frac{1}{2},j}\,\Delta\tilde{\chi}_{i+\frac{1}{2},j}\right]^{-1} \tag{4.70}$$

$$a_{i,j,3} = 2\,\left[\Delta\tilde{\chi}_{i+\frac{1}{2},j}\left(\Delta\tilde{\chi}_{i-\frac{1}{2},j} + \Delta\tilde{\chi}_{i+\frac{1}{2},j}\right)\right]^{-1} \tag{4.71}$$

and the coefficients $b_{i,j,1-3}$ being defined as:

$$b_{i,j,1} = -\frac{\Delta\tilde{\chi}_{i+\frac{1}{2},j}}{\Delta\tilde{\chi}_{i-\frac{1}{2},j}} \left(\Delta\tilde{\chi}_{i-\frac{1}{j},j} + \Delta\tilde{\chi}_{i+\frac{1}{2},j}\right)^{-1} \tag{4.72}$$

$$b_{i,j,2} = \frac{\Delta\tilde{\chi}_{i+\frac{1}{2},j} - \Delta\tilde{\chi}_{i-\frac{1}{2},j}}{\Delta\tilde{\chi}_{i-\frac{1}{2},j}\,\Delta\tilde{\chi}_{i+\frac{1}{2},j}} \tag{4.73}$$

$$b_{i,j,3} = \frac{\Delta\tilde{\chi}_{i-\frac{1}{2},j}}{\Delta\tilde{\chi}_{i+\frac{1}{2},j}} \left(\Delta\tilde{\chi}_{i-\frac{1}{2},j} + \Delta\tilde{\chi}_{i+\frac{1}{2},j}\right)^{-1} \tag{4.74}$$

The spatial discretization steps $\Delta\tilde{\chi}_{i\pm\frac{1}{2},j}$ are computed as:

$$\Delta\tilde{\chi}_{i\pm\frac{1}{2},j} = \sqrt{\left(\tilde{x}_{\left(i\pm\frac{1}{2}\right)+\frac{1}{2}} - \tilde{x}_{\left(i\pm\frac{1}{2}\right)-\frac{1}{2}}\right)^2 + \left(\tilde{z}_{\left(i\pm\frac{1}{2}\right)+\frac{1}{2},j} - \tilde{z}_{\left(i\pm\frac{1}{2}\right)-\frac{1}{2},j}\right)^2} \tag{4.75}$$

The ADI factorization of chapter 3.2 is adapted for marching in time: at each time step, the sparse, nonlinear algebraic system, that would be obtained implementing implicit Euler together with the proposed spatial discretization, Eqs. (4.50), (4.51), (4.58), (4.67) and (4.68), is reduced to two pentadiagonal algebraic systems, which are linearized and solved with Gauss method. To do this, the film flux $\tilde{\boldsymbol{Q}}$, which is defined by the fluxes $\tilde{q}$ and $\tilde{s}$ along χ and η directions, is decomposed into two contributions,

$$\tilde{\boldsymbol{Q}} = \tilde{\boldsymbol{F}} + \frac{\tilde{h}^3}{3} \left\{ \begin{array}{l} \dfrac{\cos\alpha_\eta}{\sin\alpha^*} \dfrac{\partial}{\partial\tilde{\chi}} \left(\dfrac{\hat{\boldsymbol{n}}_{\boldsymbol{\eta}} \cdot \hat{\boldsymbol{n}}_{\boldsymbol{I}}}{\tilde{r}_\eta} \dfrac{\sin\alpha^*}{\cos\alpha_\eta} \right) + \dfrac{\hat{\boldsymbol{n}}_{\boldsymbol{\eta}} \cdot \hat{\boldsymbol{n}}_{\boldsymbol{I}}}{\tilde{r}_\eta} \dfrac{\frac{\partial\alpha^*}{\partial\tilde{\eta}}}{\sin\alpha^*} \\ \dfrac{\cos\alpha_\chi}{\sin\alpha^*} \dfrac{\partial}{\partial\tilde{\eta}} \left(\dfrac{\hat{\boldsymbol{n}}_{\boldsymbol{\chi}} \cdot \hat{\boldsymbol{n}}_{\boldsymbol{I}}}{\tilde{r}_\chi} \dfrac{\sin\alpha^*}{\cos\alpha_\chi} \right) + \dfrac{\hat{\boldsymbol{n}}_{\boldsymbol{\chi}} \cdot \hat{\boldsymbol{n}}_{\boldsymbol{I}}}{\tilde{r}_\chi} \dfrac{\frac{\partial\alpha^*}{\partial\tilde{\chi}}}{\sin\alpha^*} \end{array} \right\} \tag{4.76}$$

$\tilde{r}_{\chi,\eta}$ being defined by Eq. (4.48).
The contribution of $\tilde{\boldsymbol{F}}$ is treated implicitly, while the mixed derivatives of the film thickness $\tilde{h}$ arising from

$$\left\{ \begin{array}{l} \dfrac{\partial}{\partial\tilde{\chi}} \left[\dfrac{\sin\alpha^*}{\cos\alpha_\eta} \left(\tilde{\boldsymbol{Q}} - \tilde{\boldsymbol{F}}\right) \cdot \hat{\boldsymbol{t}}_{\boldsymbol{\chi}} \right] \\ \dfrac{\partial}{\partial\tilde{\eta}} \left[\dfrac{\sin\alpha^*}{\cos\alpha_\chi} \left(\tilde{\boldsymbol{Q}} - \tilde{\boldsymbol{F}}\right) \cdot \hat{\boldsymbol{t}}_{\boldsymbol{\eta}} \right] \end{array} \right\} \tag{4.77}$$

are treated explicitly, according to the numerical scheme of chapter 3.2.
The multiplying factors $\hat{\boldsymbol{n}}_{\boldsymbol{\chi},\boldsymbol{\eta}} \cdot \hat{\boldsymbol{n}}_{\boldsymbol{I}}$, which allow to reduce the calculated radii of curvature $\tilde{r}_{\chi,\eta}$ to the free-surface outward normal direction, are computed following the procedure of Eq. (4.34). It is important to point out that $\hat{\boldsymbol{n}}_{\boldsymbol{\chi},\boldsymbol{\eta}} \cdot \hat{\boldsymbol{n}}_{\boldsymbol{I}}$ are treated explicitly when linearizing $\tilde{\boldsymbol{F}}$. However, the numerical stability of the solution is not affected since the magnitude of such terms is limited compared to the reference curvature $1/h_\infty$,

$$0 \leq \hat{\boldsymbol{n}}_{\boldsymbol{\chi},\boldsymbol{\eta}} \cdot \hat{\boldsymbol{n}}_{\boldsymbol{I}} \leq 1 \tag{4.78}$$

and the higher order derivatives of $\tilde{h}$ are still treated implicitly.
In fact, a gain of 10^6 the Neumann limit is reached for the time step, when the spatial discretization step is about the precursor film thickness δ. The allowed time step leading to convergence of the solution only decreases when the applied equilibrium contact angle approaches 90°, as it can be expected. However, equilibrium contact angles up to 60° are investigated in the present study, time steps close to 10^6 the Neumann limit being still reached.

4.5 Boundary and initial conditions

The inlet section is always defined at the boundary of the curved domain corresponding to $x = 0$ in the reference Oxy plane, where the curved substrate $z(x, y)$ is defined on. The undisturbed film flux per unit length $Q_\infty = u_\infty\, h_\infty$ is supposed to enter the domain through the inlet section, giving the following non-dimensional boundary condition to be implemented:

$$\tilde{\boldsymbol{Q}}_{\boldsymbol{in}} \cdot \hat{\boldsymbol{n}} = \tilde{Q}_\infty \tag{4.79}$$

$$\tilde{p}_0 = \mathrm{Bo}\, \cos\alpha + \tilde{\Pi}_\infty \tag{4.80}$$

$$\tilde{h}_0 = 1 \tag{4.81}$$

The undisturbed film is defined with respect to the reference Oxy plane, as explained in figure 4.5, which inclination α is univocally given by the gravity versor as:

$$\alpha = \arcsin\left[\, \hat{\boldsymbol{g}} \cdot (1,\, 0,\, 0) \,\right] \tag{4.82}$$

Thus, for a given Q_∞ the undisturbed film thickness and velocity can be calculated through Nusselt theory.
At the outlet section, which corresponds to $x = L_x$ (bottom of the reference Oxy plane), zero flux entering the domain, zero pressure gradient and mirroring of the film height distribution are imposed:

$$\tilde{\boldsymbol{Q}}_{\boldsymbol{in}} \cdot \hat{\boldsymbol{n}} = 0 \tag{4.83}$$

$$\nabla\tilde{p} \cdot \hat{\boldsymbol{n}} = \frac{\partial\tilde{p}}{\partial\tilde{\chi}} = 0 \tag{4.84}$$

$$\nabla\tilde{h} \cdot \hat{\boldsymbol{n}} = \frac{\partial\tilde{h}}{\partial\tilde{\chi}} = 0 \tag{4.85}$$

At the lateral boundaries ($y = 0,\, L_y$), symmetry conditions are imposed:

$$\tilde{\boldsymbol{Q}} \cdot \hat{\boldsymbol{n}} = 0 \tag{4.86}$$

$$\nabla\tilde{h} \cdot \hat{\boldsymbol{n}} = \frac{\partial\tilde{h}}{\partial\tilde{\eta}} = 0 \tag{4.87}$$

The same initial conditions of chapter 3.3 can be imposed:

- computational domain initially dry (covered by the precursor film δ);
- computational domain covered by the undisturbed film thickness h_∞.

4.6 Validation

Both the model used for computing the capillary pressure, Eq. (4.47), and the novel governing equations describing the evolution of a thin liquid layer over a 3D curved substrate, Eqs. (4.43), (4.44) and (4.45), are validated for a selected test case.
A computational domain describing a 3D hole standing on a flat plane is generated. A certain amount of liquid is forced to enter the domain, which is initially dry. Thus, the liquid is expected to deposit at the bottom of the hole driven by gravity, leading to a stationary free-surface, which shape is described by the well-known Young-Laplace equation, Eq. (2.18). Moreover, the volume of liquid entering the computational domain must be equal to the volume inside the hole at the end of the simulation if the numerical scheme is correctly implemented.

$\rho\,(\mathrm{kg/m^3})$	$\mu\,(\mathrm{Pa\,s})$	$\sigma\,(\mathrm{N/m})$	(n,m)	δ/h_∞	$\theta_e\,(\mathrm{deg})$
981.31	0.03642	0.03480	$(3,2)$	0.025	$0-60$

Table 4.1: Properties of the simulated liquid, 1−methylepiperazine, at $T = 25°\mathrm{C}$ and $p = 1\,\mathrm{atm}$ and imposed parameters defining disjoining pressure model

The simulated liquid is 1−methylepiperazine, which properties are listed in table 4.1. The choice of such a liquid is not casual, since it is a high viscosity liquid (as usual for engineering problems involving lubrication approximation) and it is used as a solvent in the CO_2 absorption process through structured packing.
Eq. (2.21) is still used for modelling disjoining pressure Π, with the coefficient B being defined as:

$$B = f\,\frac{(n-1)(m-1)}{n-m}\,\frac{\sigma}{\delta}\,(1-\cos\theta_e) \tag{4.88}$$

The correction factor f, which was introduced in [15], is still modeled via Eq. (2.29). Both the precursor film thickness and the exponents (n,m) must be imposed for applying disjoining pressure model. In particular, $\delta/h_\infty \in [0.025]$ and $(n,m) = (3,2)$ were imposed. Equilibrium contact angles up to $60°$ are simulated, in order to investigate the effect of surface wettability. The substrate geometry being given, each computation is identified by the gravity versor $\hat{\boldsymbol{g}}$, the shear $\boldsymbol{\tau_g} = (\tau_\chi, \tau_\eta)$ applied by the external gas flow, the imposed film flux Q_∞ entering the domain through the inlet section and the equilibrium contact angle θ_e. The following test case is chosen for such a validation:

- The reference plane Oxy is horizontal, leading to $\hat{\boldsymbol{g}} = (0,0,-1)$. Zero-shear is imposed at the free-surface, thus $\tau_\chi = 0\,\mathrm{N/m^2}$ and $\tau_\eta = 0\,\mathrm{N/m^2}$ over the whole domain.

- Since we are interested in forcing a certain amount of volume to enter the computational domain, the imposed film flux per unit length Q_∞ does not influence the stationary solution.

- It is not possible to identify the undisturbed film thickness and velocity for a thin layer of liquid over an horizontal plate with zero shear at the free-surface. Thus, the undisturbed film thickness, needed to define the precursor film δ, equals the capillary length, $h_\infty = \sqrt{\sigma/(\rho\, g)}$, which is chosen as scaling length of the problem.

- The hole, which defines the shape of the solid substrate, is described by the following relation,

$$z(x,y) = -\frac{H}{4}\left[1-\cos\left(2\,\pi\,\frac{x}{L_x}\right)\right]\left[1-\cos\left(2\,\pi\,\frac{y}{L_y}\right)\right] \tag{4.89}$$

  H being the hole depth and $L_{x,y}$ being the reference plane dimensions.

- The imposed liquid volume entering the domain is fixed to the 25% of the volume of the hole:

$$V_{in} = 0.25\int_0^{L_x}\int_0^{L_y} |z(x,y)|\; dx\, dy \tag{4.90}$$

  After V_{in} is injected in the domain, the film flux entering through the inlet section $x = 0$ is set to zero. The simulation ends when the stationary condition is reached.

L_x (cm)	L_y (cm)	H (mm)	l_c (mm)	V_{in} (cm^3)
2	2	3.5	1.997	0.0875

Table 4.2: Simulated test case: hole dimension, capillary length, liquid volume entering the domain.

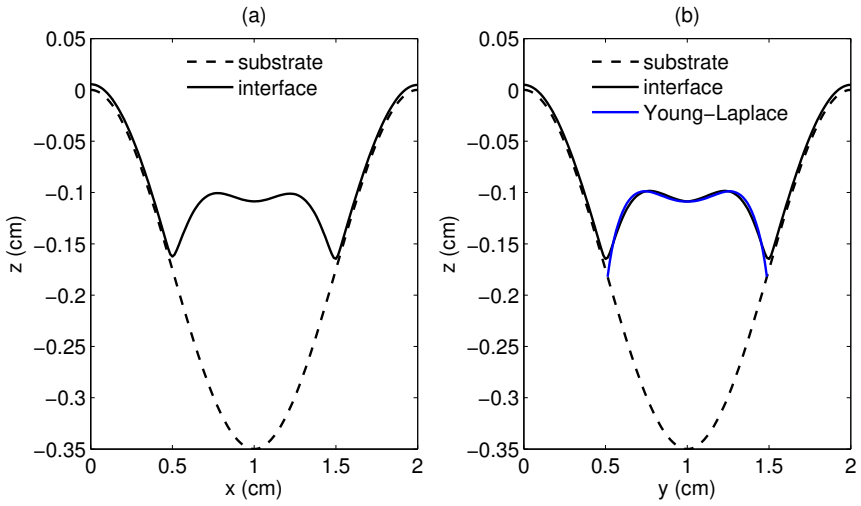

Figure 4.7: Section $y = L_y/2$ of the stationary free-surface profile (a). Section $x = L_x/2$ of the free-surface profile vs Young-Laplace equation (b). $\theta_e = 45°$.

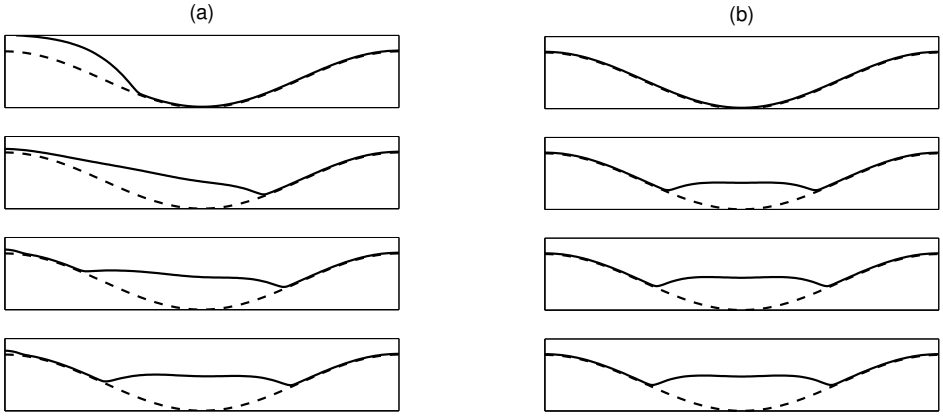

Figure 4.8: Sections $y = L_y/2$ (a) and $x = L_x/2$ (b) of free-surface profile (continuous line) and substrate surface (dashed line) at different times: $t =$ 0.08, 0.27, 0.46, 0.65 s. $\theta_e = 45°$.

The computational domain dimensions, the capillary length of the simulated liquid and the liquid volume forced inside the hole are listed in table 4.2. The curved substrate is discretized via a structured grid with elements of variable size, ensuring a sufficiently small spatial discretization step over the whole domain:

$$\Delta\chi_{i,j},\ \Delta\eta_{i,j} \leq 0.075\, h_\infty \,\forall\, i,j \tag{4.91}$$

The final volume of liquid contained in the physical domain is computed as:

$$\int_S (h-\delta)\ dS = \int_0^{L_x}\int_0^{L_y} (h-\delta)\ \frac{\sin\alpha^*}{\cos\alpha_\chi\ \cos\alpha_\eta}\, dx\, dy \tag{4.92}$$

Note that the volume given by the precursor film thickness covering the domain at $t = 0$ is removed, in order to compare the volume computed through Eq. (4.92) with V_{in}, which is forced to enter the domain.
The stationary free-surface profile is cut across its symmetry section $x = L_x/2$ and the resulting profile compared with the one coming from the solution of Young-Laplace equation,

$$p = -\sigma\, \frac{\frac{\partial^2 z_I}{\partial y^2}}{\left[1+\left(\frac{\partial z_I}{\partial y}\right)^2\right]^{3/2}} + \rho\, g\, \frac{(z_I - z)}{1+\left(\frac{\partial z}{\partial y}\right)^2} \tag{4.93}$$

z_I denoting the free-surface height with respect to the horizontal.
Eq. (4.93) is solved numerically, imposing the following boundary conditions,

$$z_I\big|_{y_c} = z \tag{4.94}$$

y_c defining the contact line.
To do this, a `FORTRAN` solver was developed. The contact line is located where the stationary liquid distribution, which is computed solving numerically the

governing equations, Eqs. (4.43), (4.44), (4.45) and (4.46), triggers the precursor film thickness. Thus, two points standing on the curved substrate can be obtained cutting the contact line at $x = L_x/2$: these two points represent the domain boundaries y_c, needed for applying the boundary conditions given by Eq. (4.94). The so-defined boundary value problem, Eqs. (4.93) and (4.94), is thus solved, discretizing the capillary pressure via a second order centered scheme. The resulting algebraic system is linearized and solved with an iterative method, the first guess being the liquid profile computed from the stationary liquid layer distribution. The coupling between the solver of Eq. (4.93) and the computed stationary liquid distribution on the computational grid defining the 3D substrate surface is ensured cutting the computational grid at $x = L_x/2$ and using the obtained array to define both the 1D domain, which Eq. (4.93) is solved on, and the first guess of the solution.
Figures 4.7(a) and 4.7(b) show the two symmetry sections of the stationary solution. As expected, the liquid converges to the bottom of the hole and arranges in a symmetric manner, according to the substrate geometry. In figure 4.7(b) the computed profile is also compared with the one obtained solving Young-Laplace equation, Eq. (4.93), revealing almost a perfect matching. The volume of the stationary liquid distribution inside the domain is also computed through Eq. (4.92) and compared with the imposed V_{in}: an error within 0.01% is observed, thus the volume is reasonably conserved.
The evolution of the spreading drop is shown in figures 4.8(a) and 4.8(b), which plot some *snapshots* of the sectioned free-surface solution at different times: the liquid, which is forced to enter the computational domain through section $x = 0$, slowly goes inside the hole, until the stationary symmetrical shape is reached.

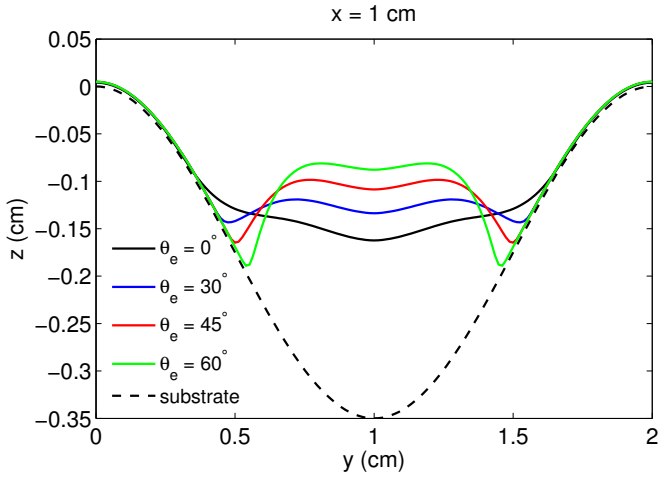

Figure 4.9: Section $x = L_x/2$ of the stationary liquid layer distributions, obtained imposing four different surface wettabilities, the equilibrium contact angle ranging in $\theta_e \in [0°, 60°]$; test case given by table 4.2.

Figure 4.9 shows the effect of surface wettability. The stationary liquid layer distributions deriving from the simulation of four different values of the equilibrium contact angle θ_e are sectioned along $x = L_x/2$. The test case is again

described by table 4.2. The higher the imposed equilibrium contact angle, the narrower the stationary drop at the bottom of the 3D curved substrate.
Equilibrium contact angles up to 60° are simulated in figure 4.9. This is also an important goal, since such an high value of the contact angle had never been simulated under lubrication approximation before, due to the small slope approximation. However, a proper validation in terms of modelling the surface wettability will be given in the next chapter, where the capability of the proposed model of describing surface wettability according to the well known Tanner-Hoffman-Voinov formula will be tested.

4.7 Film past an obstacle

After the solver is validated, a new test case is considered, looking for new information about wetting dynamics of a general curved substrate. In particular, a film flowing over an inclined plate driven by gravity is considered. In order to perturb the 1D film flow, a general curved substrate is defined within the plate. Thus, the effect of substrate shape and wettability are investigated, implementing obstacles of variable size and running simulations for different values of the equilibrium contact angle.
The substrate geometry $z(x, y)$ is defined using the following equation,

$$z(x,y) = \frac{H}{4}\left[1-\cos\left(2\,\pi\,\frac{k_x\,x}{L_x}\right)\right]\left[1-\cos\left(2\,\pi\,\frac{k_y\,y}{L_y}\right)\right] \tag{4.95}$$

H being the obstacle height and $k_{x,y}$ being the number of obstacles contained in the computational domain along x and y directions.
Simulations are run implementing the computational grid through Eq. (4.95). The simulated liquid is again 1−methylepiperazine, see properties in table 4.1. The disjoining exponents (n, m) are still fixed to $(3, 2)$, while a precursor film thickness δ equal to $0.05\,h_\infty$ is chosen, since it represents a good compromise between computational costs and accuracy of contact line dynamics modelling. The boundary conditions described in chapter 4.5 are applied. Thus, the film flow enters the domain through the section $x = 0$, where the undisturbed film flow Q_∞ is applied. Thanks to the symmetrical configuration of the problem, only half of the domain is simulated (thus $y \in [0, L_y/2]$). Symmetry conditions are imposed at the lateral boundaries $y = 0, L_y/2$, meaning that an array of obstacles with spacing L_y across y direction is simulated. The dry initial condition is imposed, thus the domain is initially covered by the precursor film only.
First, the test case identified by T1 in table 4.3 is considered. Two simulations are run changing the surface wettability only. The substrate defining the computational domain, which is described by Eq. (4.95), is also shown in figure 4.10(a).
In figure 4.11(b) the stationary liquid layer distribution resulting from the simulation of the lower surface wettability case, $\theta_e = 30°$ imposed, is shown. Figure 4.11(b) should be compared with the substrate morphology, figure 4.11(a),

Test case	L_x (cm)	L_y (cm)	α (deg)	τ_g (N/m)	H (cm)	k_x	k_y
T1	3	2	60	0	1	2	1
T2	3	3	60	0	0.8	1	1
T3	3	3	60	0	0.4	1	1

Table 4.3: Computational domain dimensions $L_x \times L_y$, inclination of the reference plane with respect to the horizontal α, shear applied by the external gas flow $\tau_g = |\boldsymbol{\tau_g}|$, obstacle size H and number of obstacles $k_{x,y}$ for the investigated test cases, T1, T2 and T3.

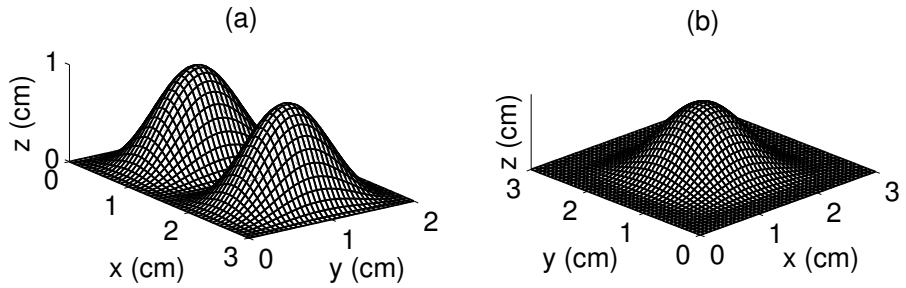

Figure 4.10: Simulated 3D curved substrate: test case T1 (a); test cases T2 and T3 (b). The reference Oxy plane is inclined at an angle $\alpha = 60°$ to the horizontal.

in order to understand the behavior of the liquid on and around the two obstacles. In fact, the liquid tries to surround the first obstacle, but it can only flow around, due to the large dimension of the obstacle itself. Thus, the portion of substrate in-between the two obstacles keeps dry due to the high value of the imposed contact angle, $\theta_e = 30°$.

The same simulation was run for a different value of the substrate wettability. In particular, zero equilibrium contact angle was imposed. Figure 4.11(d) shows that the imposed θ_e has a great impact on the wetting dynamics, since the liquid is also able to cover the region between the two obstacles for sufficiently high surface wettability. In fact the substrate wetted area A_{WET} increases for increasing surface wettability, $\theta_e \downarrow$. Also, the liquid front is almost able to overpass the first obstacle. This is clear looking at the stationary contact line in figure 4.11(c), which is much closer to reach the top of the first obstacle.

An interesting comparison between the two simulations in terms of wetting dynamics can be done sectioning the two stationary solutions, figures 4.11(b) and 4.11(d), at $y = 1\,\text{cm}$ (corresponding to the symmetry line of the curved substrate geometry) and plotting the resulting free-surface profiles, as shown in figures 4.12(a) and 4.12(b) respectively. In fact, the different ways that the liquid-air interface approaches the contact line clearly suggest different substrate wettabilities, according to the imposed equilibrium contact angles, with an higher free-surface slope close to the contact line appearing in figure 4.12(a), which is referred to the higher value $\theta_e = 30°$.

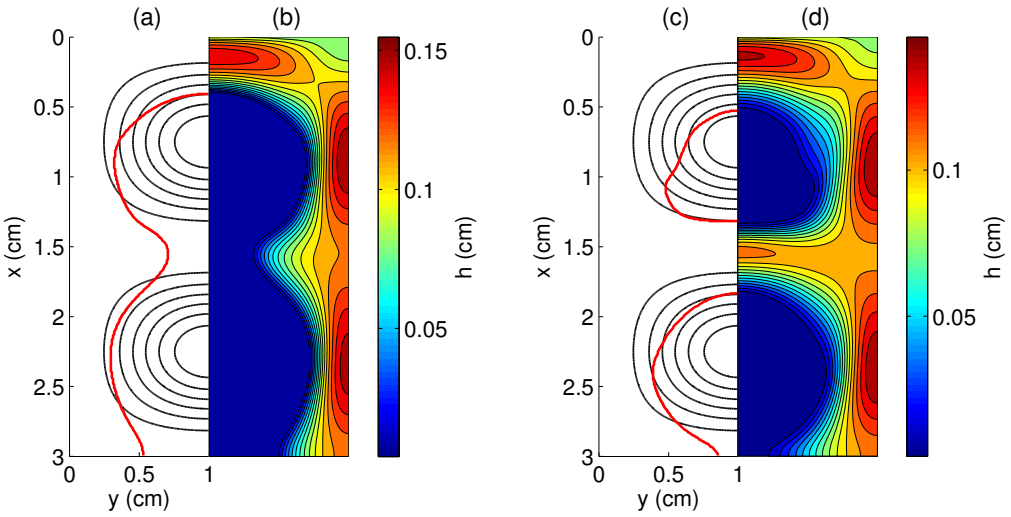

Figure 4.11: Test case T1. Substrate morphology (black isolines referred to $z = 0.14, 0.29, 0.43, 0.57, 0.71, 0.86\,\text{cm}$) and stationary contact line (red line) defining the dry-patch: $\theta_e = 30°$ (a), $\theta_e = 0°$ (c); stationary film distribution over the curved substrate: $\theta_e = 30°$ (b), $\theta_e = 0°$ (d). $Q_\infty = 0.5\,\text{cm}^2/\text{s}$.

Further simulations are run considering the test setup identified by T2 and T3 in table 4.3, which only differs from each other in the obstacle size, with the aim of investigating the influence of the surface wettability, the undisturbed film flow and the obstacle dimension on the wetting dynamics. The bumped geometry of the computational domain is shown in figure 4.10(b). The simulated liquid is still 1−methylepiperazine, which properties are listed in table 4.3. The imposed film flow per unit length entering the domain is ranged in $Q_\infty \in [0.25, 1.5]\,\text{cm}^2/\text{s}$, leading to Reynolds number $\text{Re} = \rho Q_\infty/\mu \leq 4.04$, according to lubrication approximation validity, while the equilibrium contact angle is ranged in $\theta_e \in [15°, 45°]$. The results are given in terms of total wetted area A_{WET} of the substrate. The computation of A_{WET} is quite simple: since it is defined as the portion of substrate surface covered with a thin layer of liquid higher than the precursor film thickness, the i, j-th grid element, which surface $\Delta S_{i,j}$ is given by Eq. (4.63), is wetted if $h_{i,j} > \delta$. It is useful to normalize the wetted area with respect to the substrate area, i.e. the total area of the computational domain.

Figures 4.13(a) and 4.13(b) clearly show the influence of both the surface wettability and the film flux on the computed wetted area. The results are referred to the stationary liquid layer distribution. As expected, higher substrate wettability leads to higher wetted area. The same consideration can be done for the imposed film flux, its influence being more important in the test case T3, i.e. smaller obstacle. Also, the effect of the obstacle size is investigated, since the test cases T2 and T3 only differs in the obstacle size. In fact, for given values of Q_∞ and θ_e, the normalized wetted area A_{WET}/A_{SUB} is always higher for the smaller obstacle, test case T3, as it can be easily understood comparing figures 4.13(a) and 4.13(b). As a final remark, if the test case T3 is considered

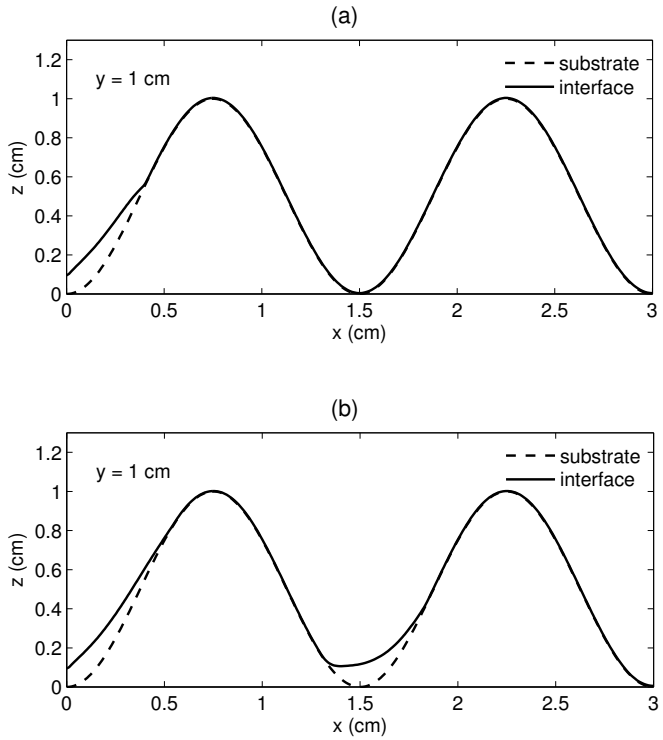

Figure 4.12: Test case T1: section $y = 1\,\text{cm}$ (corresponding to symmetry line $y = L_y/2$) of the two stationary liquid layer distributions over the substrate for two different surface wettabilities: $\theta_e = 30°$ (a); $\theta_e = 0°$ (b). $Q_\infty = 0.5\,\text{cm}^2/\text{s}$.

the obstacle is completely overpassed when $\theta_e = 15°$ and $Q_\infty = 1.5\,\text{cm/s}$, leading to a fully wetted domain. Such a results is not reached when the obstacle height equals 0.8 cm: however, the full wetting condition can be reached for high values of the Reynolds number, Re >> 1, but the lubrication approximation is not valid when the liquid motion is also driven by inertia.
Finding a threshold, which defines the conditions leading to the full wetting of a given curved substrate, is crucial for a number of engineering applications. For example, when a drop spreads on the hydrophilic surface of a lens, as much wetted area as possible should be ensured in order to hold an uniform wetting layer and thus the lens working conditions as well. The wetting of a curved substrate is also involved in in-flight icing phenomenon, where the liquid layer evolution influences the predicted ice accretion process. Even decoupling the air flow solution from the film solution, it is obviously computationally expensive to simulate the film evolution over the whole domain, i.e. the aircraft surface, due to the different length scales, but still useful information can be obtained.
Figure 4.14(a) and 4.14(b) show the contact line evolution over the solid substrate and the stationary liquid layer distribution for the test case T3, $Q_\infty = 0.5\,\text{cm}^2$ and $\theta_e = 30°$. Note that the contact line overcomes the top of the obstacle, but the domain is not fully wetted since a small dry-patch still appears, the film flow rate being lower than the critical one. Moreover, looking

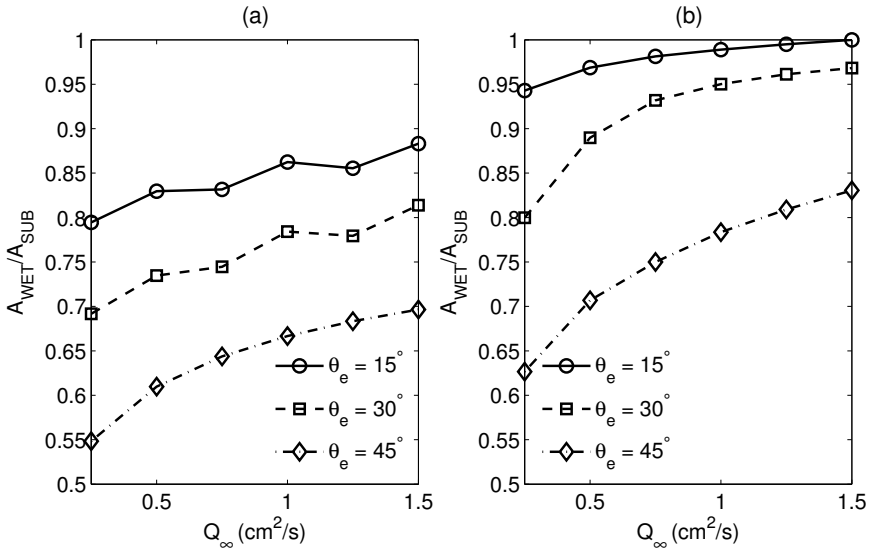

Figure 4.13: Normalized wetted area A_{WET} of the stationary solution as a function of imposed film flow rate Q_∞ and equilibrium contact angle θ_e: test case T2 (a); test case T3 (b).

at the wetting history, i.e. the contact line evolution in time shown in figure 4.14(a), it can be noticed that the obstacle induces the formation of a growing finger which drains the film fluid. This liquid bulk is thus driven by gravity. After it reaches the bottom of the domain, the contact line motion is mainly driven by capillary forces, the contact angle mainly influencing the wetting dynamics. Results from numerical simulations suggest that imposing higher values of θ_e (while keeping constant both α and Q_∞) leads to: bigger draining finger; slower contact line motion after the liquid finger spreads through the outlet section; lower wetted area.
In figure 4.14(c) the stationary free-surface profile is sectioned along its symmetry line $y = L_y/2$, confirming that the liquid front overpass the highest point of the hill, but it has not enough energy to wet the whole domain.

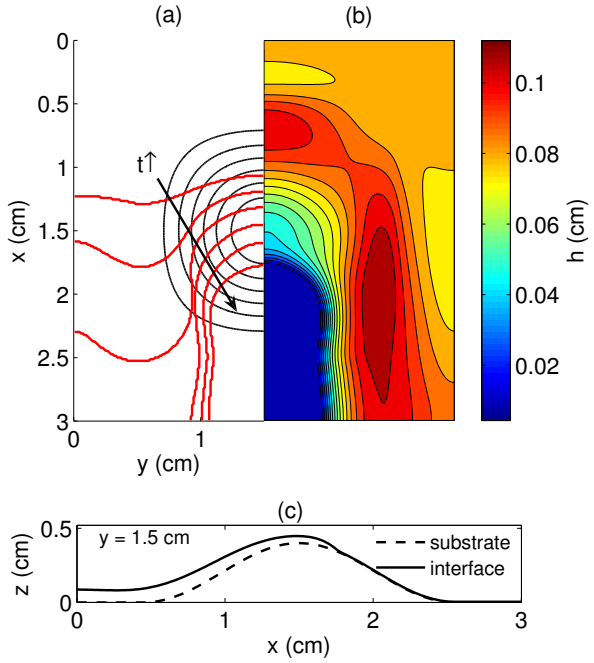

Figure 4.14: Test case T3: substrate morphology (black isolines referred to $z = 0.06, 0.11, 0.17, 0.23, 0.29, 0.34\,\text{cm}$) and contact lines (red lines) at different times, $t = 0.20,\ 0.26,\ 0.35,\ 0.52,\ 0.83,\ 1.3\,\text{s}$ (a); stationary film distribution over the curved substrate (b); section $y = 1.5\,\text{cm}$ of the stationary liquid layer distribution (c). $Q_\infty = 0.5\,\text{cm}^2/\text{s}$, $\theta_e = 30°$.

Chapter 5

Absorption and distillation processes

5.1 Overview

In gas absorption process one or more species (solutes) are transferred from a gas mixture to a liquid solvent without any change in chemical properties of the involved species. The inverse process of removing the solute from the liquid solvent is called stripping or desorption. Absorption, stripping and distillation operations are carried out in vertical, cylindrical columns or towers within proper devices, which provide the contacting between gas and liquid flowing countercurrently and guarantee an increase of liquid-gas interfacial surface, through which mass transfer takes place. These columns are classified depending on the corresponding devices gaining liquid-gas contacting:

- *Plate columns.* Cross-flow plates, figure 5.1(a), use a liquid downcomer in order to ensure the desired transfer efficiency; new designs are provided with perforations for dispersing gas into liquid on the plate. Counterflow plates are characterized by openings (simple round perforations of $3 - 13\,\text{mm}$ diameter) through which both liquid and gas flow in a pulsating fashion.

- *Packed columns.* These columns may be filled with randomly oriented packing material, figure 5.1(b), or structured packing, figures 5.1(c) and 5.1(d), the latter being characterized by corrugated layers, put in contact and carefully positioned one close to each other; liquid-gas interface area and gas flow pressure drop across the absorber play a crucial role in the optimization process, since they univocally define the effective area for mass transfer and the energy consumption.

The column design is usually carried out via a step by step procedure, that requires the designer to determine: (a) the best solvent; (b) the best gas velocity through gas absorber; (c) the height of the column; (d) operating pressure and temperature; (e) mechanical design of the components, including flow distributers and type of packing/inserts.

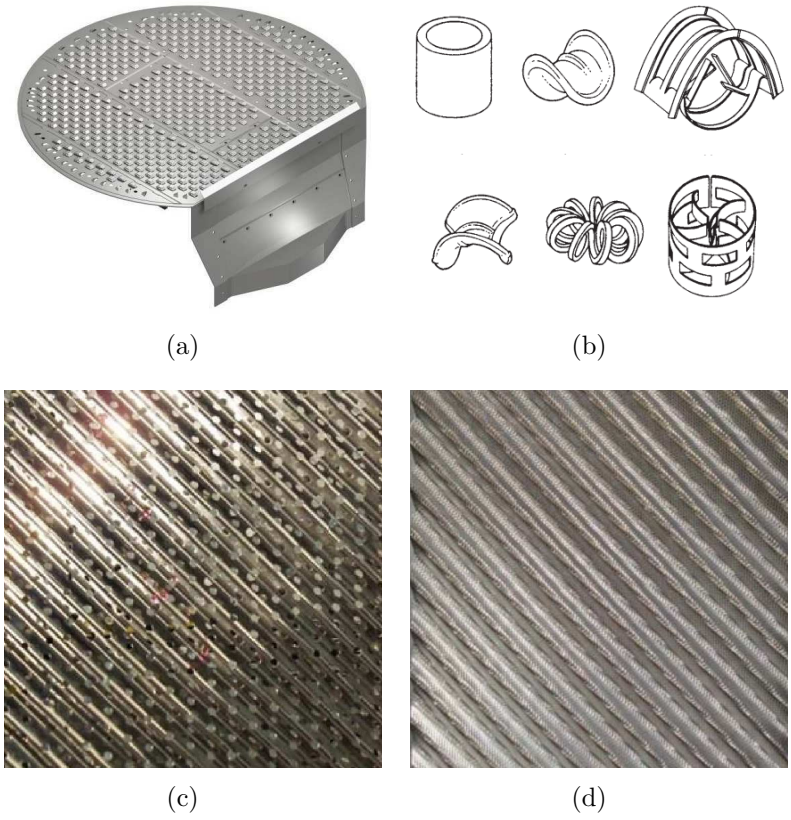

(a) (b)

(c) (d)

Figure 5.1: Sieve plate (a). Random packing (b). Smooth, perforated packing (c). Embossed, unperforated packing (d).

A great effort in the understanding of mass transfer phenomenon, occurring when the solute migrates from gas to liquid, was put by Whitman, who introduced in 1923 the well known two-film model [32]. Assuming that two stagnant surface films, through which the solute concentration varies between the values at gas bulk and at liquid bulk, persist at the liquid-gas interface, the Fick's law can be written as,

$$N_s = D_l \frac{c_{l,I} - c_l}{\delta_l} = D_g \frac{p_g - p_{g,I}}{\delta_g} \tag{5.1}$$

where:

- N_s $(\text{moles}\,\text{m}^{-2}\,\text{s}^{-1})$ is the molar flow rate per unit interface area of solute migrating from gas to liquid;
- c_l and $c_{l,I}$ are the concentrations $\left(\text{moles}\,\text{l}^{-1}\right)$ of solute inside liquid solvent at liquid bulk and at liquid-gas interface respectively;
- p_g and $p_{g,I}$ are the partial pressures of solute inside gas mixture at gas bulk and at interface, that can be reconduced to the corresponding solute concentrations through Henry's law, $p_g = k_H\, c_g$.
- $\delta_{l,g}$ and $D_{l,g}$ are the stagnant film thicknesses and the diffusion coefficients respectively.

Two-film theory allows the designer to construct the equilibrium curve at given operating pressure and temperature, each point of such a curve representing the equilibrium concentrations at liquid-gas interface of solute in liquid solvent and in gas mixture. Finding reliable equilibrium data, which is one of the most time-consuming task, is a crucial step for absorption/stripping column sizing. Figures 5.2(a) and 5.2(b) show the regions of operating lines for both gas absorption and stripping for a given equilibrium curve, the coordinates X and Y being defined as:

$$X = \frac{\text{moles of solute}}{\text{moles of } \textit{pure} \text{ solvent}} \tag{5.2}$$

$$Y = \frac{\text{moles of solute}}{\text{moles of } \textit{pure} \text{ gas}} \tag{5.3}$$

The slope of the operating line univocally defines the required ratio N_L/N_G between liquid phase molar velocity and gas molar velocity (moles $\mathrm{m}^{-2}\,\mathrm{s}^{-1}$), which the absorption/stripping column must be designed for, and allows to determine the number of theoretical stages (plate columns) or transfer units (packed towers).

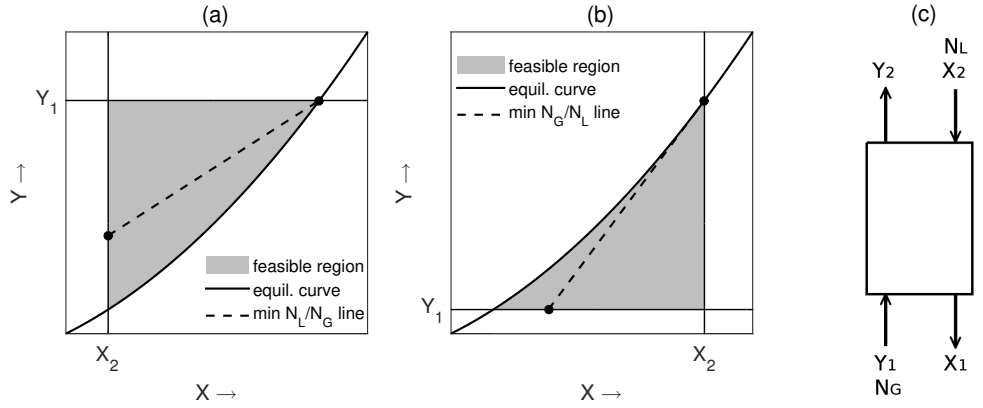

Figure 5.2: Design diagrams for: absorption (a); stripping (b). Molar fluxes entering and exiting the absorption/stripping column through sections 1 and 2 (c).

5.2 Structured packing

Structured packed columns have been widely used in distillation and absorption processes since the 1980s, since the additional mass transfer due to the increase in the interfacial area, induced by the spreading liquid over the packing surface, leads to higher efficiency. As an example, the post-combustion carbon dioxide capture is based on chemical absorption via the reaction with a solvent inside a packed column, where the absorption is carried out with the gas CO_2 flowing up, while the liquid solvent flows down through the packing surface composing the packed column. Even if the structured packing is

well established, the local flow behavior inside the packing, that greatly affects their efficiency, is not fully understood. Since the geometrical characteristics of the packing surface influence the flow behavior, the optimization of the corrugated sheets of packing becomes crucial. There are three ways to optimize the packing features:

- Introducing perforations, figure 5.1(c).
- Varying the surface of the corrugated sheet with grooved, lanced, textured, smoothened surface; an example of textured surface is shown in figure 5.1(d).
- Changing the elementary geometry, which is given by: corrugation angle ϕ, base W and height H, see figure 5.3. The ratio W/H ranges from $2:1$ to $4:1$.

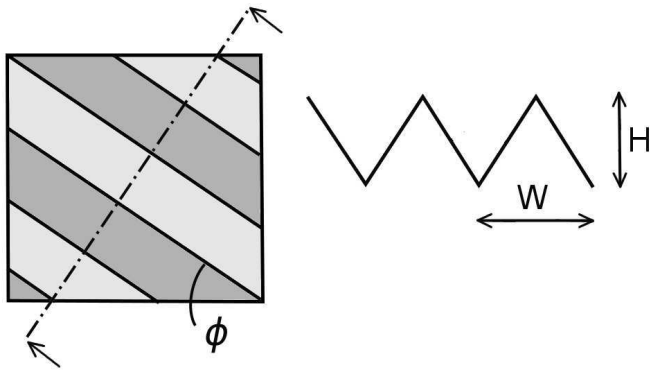

Figure 5.3: Elementary geometry of the corrugated sheet of packing.

Both numerical and experimental literature are available, but it is clearly difficult to look inside the packed columns, making the numerical approach much more suitable. However, a packed column may have diameter of 10 m, while the characteristic dimension of structured packing is of the order of 20 cm and the film height may be less than a millimeter. Thus a fully 3D approach is typically limited to the investigation of a single facet of the problem: most analysis, in fact, are focused on the hydrodynamic behavior of a liquid along plane surfaces. In particular, Hoffmann et al. [33] validated the Volume Of Fluid (VOF) method in the case of a film flowing down an inclined plate with walls at the lateral boundaries, constructing a two fluid model (gas-liquid) and comparing numerical results with experimental evidences. Singh et al. presented a number of numerical results in [12], where the authors considered the same test case of [33] and adopted a fully 3D approach (VOF) as well, looking for the influence of solvent properties and flow rate. There are other literature works involving absorption and distillation through structured packing [5, 34, 35], which focus on numerical simulation of a falling film driven by gravity and shear using VOF. Even the case of more than one liquid phase

(plus the gas phase) involved, as it happens in distillation of heterogeneous azeotropic mixtures, is numerically investigated in [34, 35].
Here a different approach is followed. In order to reduce the computational effort for the simulation of the film dynamics, we consider the 2D lubrication equation, which is solved numerically by means of the Finite Volume Method (FVM) solver developed in `FORTRAN`. The idea is to look for an efficient, yet accurate model that could be coupled with a full CFD of the core flow, in order to investigate simultaneously both the large scales of the device (the full packed column, or the full wing or nacelle for a in-flight icing problem) and the smaller scale of the film. The implementation of the capillary pressure according to Eqs. (4.31), (4.32) and (4.33) allows to investigate equilibrium contact angle up to 60°, thus making it suitable for the application to absorption/distillation through structured packing.

5.3 Problem setup

The dynamics of a gravity driven film flowing down an inclined plate are investigated, being the simplest configuration for better understanding the hydrodynamics through structured packing, [12]. Thus, the governing lubrication equations obtained in chapter 4 reduce to Eq. (2.52), which is again proposed,

$$\frac{\partial h}{\partial t} = -\nabla \cdot \left(-\frac{\nabla p}{3\,\mu}\, h^3 + \frac{\boldsymbol{\tau_g}}{2\,\mu}\, h^2 \right) \tag{5.4}$$

the pressure being given by,

$$p = \rho\, g\, (h\, \cos\alpha - x\, \sin\alpha) - 2\,\sigma\,\kappa_m - \Pi \tag{5.5}$$

where x is the downhill direction of the plate, α the plate inclination to the horizontal and $\boldsymbol{\tau_g}$ the shear applied at the free-surface by the external gas flow. The case of gravity driven film ($\boldsymbol{\tau_g} = \mathbf{0}$) is investigated.
Since high contact angles must be investigated, the procedure described in chapter 4.3 is used for modelling the mean curvature κ_m of the free-surface. Thus, Eq. (4.33) reduces to,

$$2\,\kappa_m = \frac{1}{r_x}\left[\frac{1+\left(\frac{\partial h}{\partial x}\right)^2}{1+\left(\frac{\partial h}{\partial x}\right)^2+\left(\frac{\partial h}{\partial y}\right)^2}\right]^{1/2} + \frac{1}{r_y}\left[\frac{1+\left(\frac{\partial h}{\partial y}\right)^2}{1+\left(\frac{\partial h}{\partial x}\right)^2+\left(\frac{\partial h}{\partial y}\right)^2}\right]^{1/2} \tag{5.6}$$

with $r_{x,y}$ being given by the Young-Laplace equation:

$$\frac{1}{r_x} = \frac{\frac{\partial^2 h}{\partial x^2}}{\left[1+\left(\frac{\partial h}{\partial x}\right)^2\right]^{3/2}},\ \frac{1}{r_y} = \frac{\frac{\partial^2 h}{\partial y^2}}{\left[1+\left(\frac{\partial h}{\partial y}\right)^2\right]^{3/2}} \tag{5.7}$$

Along the upper boundary of the domain, $x = 0$, an inlet section of length $L_{in} \in [0, L_y]$ is defined, where the entering film flux is settled to the undisturbed

one, $\boldsymbol{Q_{in}} \cdot \hat{\boldsymbol{n}} = u_\infty \, h_\infty$, and the pressure p_∞ is imposed; outside the inlet section, the entering flux is equal to zero as well as the pressure. Two different sets of boundary condition on the lateral boundaries $y = 0,\ L_y$ can be used: symmetry boundary condition for the simulation of a plate of indefinite extension along y direction, or wall boundary condition for the simulation of a domain bounded by solid end-walls at $y = 0,\ L_y$. The following conditions must be implemented for imposing the wall boundary condition:

- zero liquid flux crossing the wall, $\boldsymbol{Q} \cdot \hat{\boldsymbol{n}} = 0$;
- free-surface inclination equal to equilibrium contact angle θ_e.

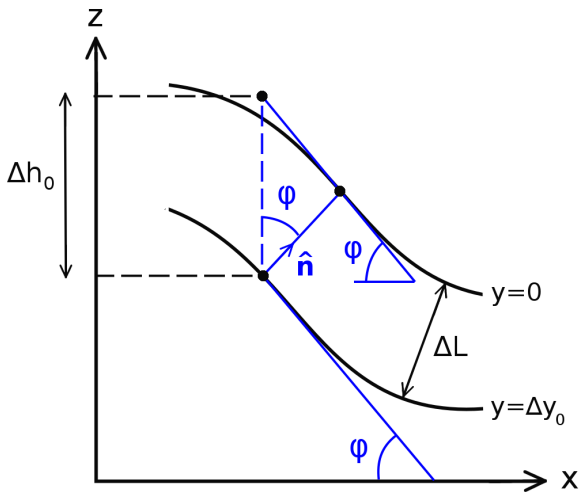

Figure 5.4: Geometrical layout leading to wall boundary condition: cutting the free-surface profile at $y = 0$ and $y = \Delta y_0$, two isolines (black, curved lines) with spacing ΔL are obtained.

The equation to be respected for imposing a given contact angle at the wall can be obtained looking at the geometrical layout of figure 5.4. If the equilibrium contact angle is imposed, the distance ΔL between the isolines $y = 0$ and $y = \Delta y_0$ must keep constant:

$$\Delta L = \frac{\Delta y_0}{\tan \theta_e} \tag{5.8}$$

Assuming that the isolines $y = 0$ and $y = \Delta y_0$ are close enough to ensure a common normal direction $\hat{\boldsymbol{n}}$ gives:

$$\Delta h_0 = \frac{\Delta L}{\cos \varphi} \tag{5.9}$$

φ being the contact line inclination at the wall:

$$\varphi = \arctan\left(\frac{\partial h}{\partial x}\right) \tag{5.10}$$

Combining Eqs. (5.8), (5.9) and (5.10), it derives that:

$$\left.\frac{\partial h}{\partial y}\right|_0 = -\frac{\sqrt{1+\left(\frac{\partial h}{\partial x}\right)^2}}{\tan\theta_e}, \quad \left.\frac{\partial h}{\partial y}\right|_{L_y} = +\frac{\sqrt{1+\left(\frac{\partial h}{\partial x}\right)^2}}{\tan\theta_e} \tag{5.11}$$

Eq. (5.11) is implemented for imposing contact angle at the lateral boundaries, with $\frac{\partial h}{\partial x}$ calculated by means of a second order centered scheme, using the available values of h in the grid elements next to the domain boundary.
The dry initial condition, i.e. film height equal to the precursor film thickness $h = \delta$ over the whole domain, is used for the current simulations, in order to focus on the wetting dynamics.

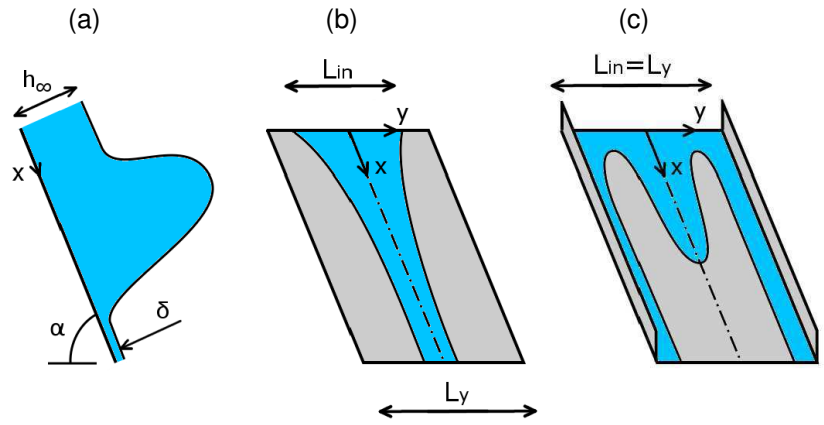

Figure 5.5: Investigated setup: 1D film down an inclined plate (a); confined inlet section L_{in} at $x = 0$ (b); plate bounded by lateral walls (c)

Three different setups are investigated:

- The code is tested in the case of a 1D film flowing down an inclined plate, see figure 5.5(a), in order to verify the capability of the disjoining pressure coupled with the novel capillary pressure model, Eqs. (5.6) and (5.7), to simulate equilibrium contact angle up to 60°.
- The rivulet build-up problem is shown in figure 5.5(b): the liquid enters the domain through a confined inlet section $L_{in} < L_y$ at the top of the plate and arranges as a stable rivulet. The results are compared with both analytical and literature numerical evidences, in terms of stable rivulet profile and plate wetted area.
- According to previous literature works [12, 33–35], the wetting dynamics in structured packing are investigated considering an inclined plate bounded by lateral walls with liquid entering through the inlet section $x = 0$, as shown in figure 5.5(c).

The physical properties and the corresponding Kapitza numbers of the simulated liquids, which are used as solvent in CO_2 absorption through structured packing [12], are listed in table 5.1.

Liquid	$\rho\,(\mathrm{kg/cm^3})$	$\mu\,(\mathrm{Pa\,s})$	$\sigma\,(\mathrm{N/m})$	Ka
$0.31x$ MPZ	981.31	0.03642	0.03480	14.8
$0.41x$ MPZ	962.20	0.02348	0.03589	24.6
$0.51x$ MPZ	946.41	0.01336	0.03437	49.7

Table 5.1: Physical properties of 1−methylepiperazione at $T = 25°\mathrm{C}$ and $p = 1\,\mathrm{atm}$.

5.4 Results and discussion

First of all, the disjoining pressure model, Eqs. (2.21), (2.28) and (2.29), is validated for a 1D film flowing down an inclined plate. Note that it was already done, but in case of capillary pressure modeled via small slope approximation. The same validation is proposed, but higher values of the equilibrium contact angle are tested. Simulations are run imposing: plate inclination equal to $\alpha = 60°$; equilibrium contact angle in the range $\theta_e \in [30°, 60°]$; precursor film thickness $\delta = 0.05\,h_\infty$; spatial discretization step equal to $\Delta x = 0.05\,h_\infty$. The simulated liquid is 1−methylepiperazine $0.31x$ MPZ, which physical properties are listed in table 5.1.

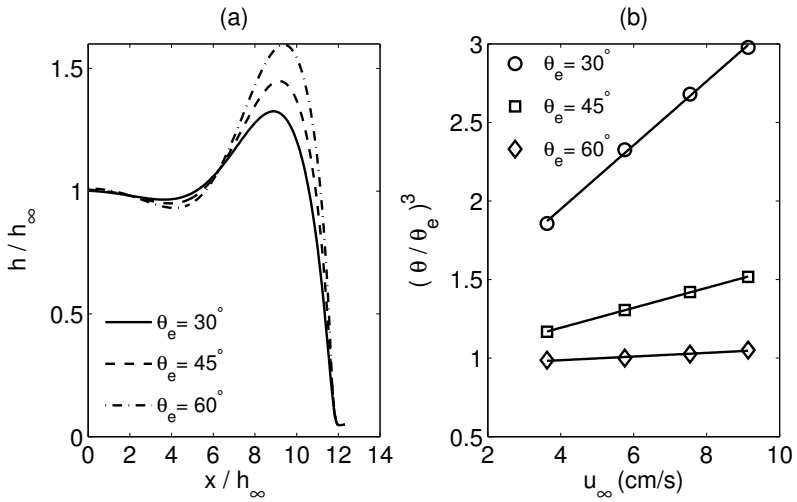

Figure 5.6: 1D gravity driven film: capillary ridge shape for different equilibrium contact angles θ_e, $Q_{in} = 1\,\mathrm{cm^2/s}$ (a); dynamic contact angle θ vs undisturbed film velocity u_∞ and imposed equilibrium contact angle θ_e: numerical results (symbols) and Eq.(5.12) (lines) (b).

Figure 5.6(a) shows the shape of the capillary ridge, which is self-similar in time and typically appears close to the moving contact line: according to literature [15], higher values of the imposed equilibrium contact angle lead to higher ridge dimensions. In figure 5.6(b) the dynamic contact angle is computed for different film flow rates and fitted using the Tanner-Hoffman-Voinov formula [15, 23]:

$$\theta^3 = {\theta_e}^3 \left(1 + C\,\frac{\mu\,u_\infty}{\sigma}\right) \tag{5.12}$$

where C is the fitting parameter.
Note that the undisturbed film velocity is considered instead of contact line velocity as in Eq. (2.30): u_∞ and u_c being strictly connected, Eqs. (5.12) and (2.30) are equivalent. According to the validation procedure found in [15], it can be stated that surface wettability and contact line dynamics are correctly modeled using disjoining pressure and assuming a thin precursor film, since Eq. (5.12) well describes the behavior of the dynamic contact angle θ as a function of the undisturbed film velocity u_∞. Moreover, equilibrium contact angle up to $\theta_e = 60°$ had not been investigated (and thus validated) before using disjoining pressure and lubrication theory.
The solver code is then tested with numerical results found in literature, involving rivulets build up. The test case of Singh et al. [12] is chosen for the simulations: $6 \times 5\,\mathrm{cm}^2$ plate, inclined with an angle $\alpha = 60°$ to the horizontal; film flux per unit length $Q_{in} = 1\,\mathrm{cm}^2/\mathrm{s}$ entering through a confined inlet section $L_{in} = 2\,\mathrm{cm}$ at the top of the plate, $\dot{V}_{in} = Q_{in}\,L_{in} = 2\,\mathrm{cm}^3/\mathrm{s}$; $1-$methylepiperazine $0.31x$ MPZ liquid simulated (see properties in table 5.1). It is important to point out that the chosen liquid is used as solvent in packed columns for carbon capture [12]. Thus, this further validation serves to demonstrate that the developed solver is able to predict the liquid layer evolution in test cases that involve absorption/distillation process.
Thanks to the symmetrical configuration of the problem, only half of the plate is simulated, with symmetry condition imposed at the lateral boundaries $y = 0,\ L_y$, i.e. an array of parallel rivulets with $2\,L_y$ spacing is simulated. Inlet section is implemented as described in section 5.3. The precursor film thickness is set to $\delta = 0.025\,h_\infty$. A grid dependence analysis suggested to impose spatial discretization step, which is kept uniform over the computational domain for the rivulet build up simulations, of about $0.075 - 0.1\,h_\infty$, depending on the imposed equilibrium contact angle, which is varied in the range $\theta_e \in [20°,\ 60°]$.

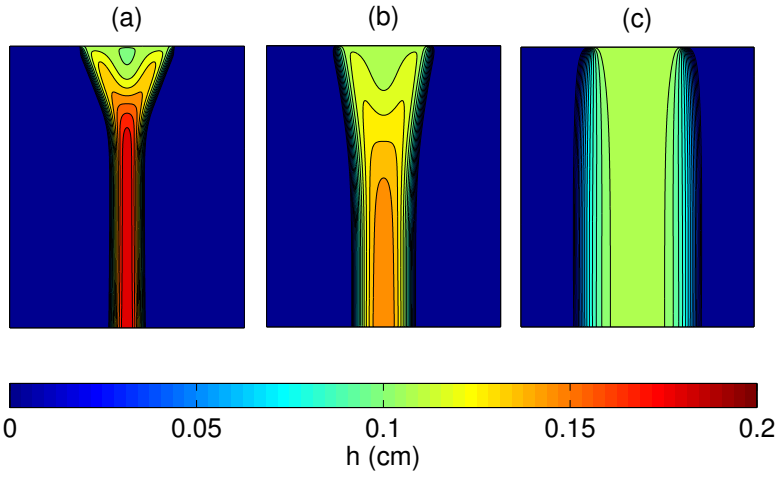

Figure 5.7: Stationary rivulet distribution over the inclined plate for: $\theta_e = 60°$ (a), $\theta_e = 40°$ (b), $\theta_e = 20°$ (c). $\alpha = 60°$, $\dot{V}_{in} = 2\,\mathrm{cm}^3/\mathrm{s}$.

Figure 5.7, which shows how the stationary liquid layer distribution changes with the surface wettability, clearly proves that the higher the imposed equilibrium contact angles, the narrower the shape of the rivulet, according to the numerical results of Singh et al. [12].

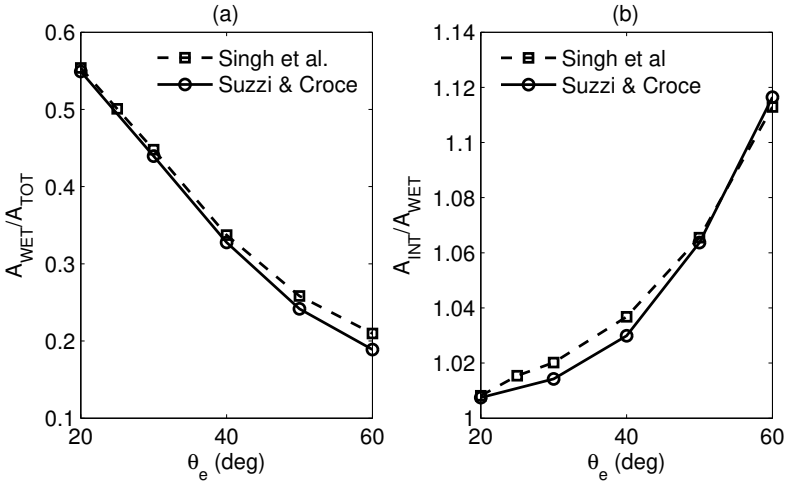

Figure 5.8: Normalized wetted area of the rivulet as a function of the equilibrium contact angle (a). Normalized interface area of the rivulet as a function of the equilibrium contact angle (b). $\alpha = 60°$, $\dot{V}_{in} = 2\,\mathrm{cm}^3/\mathrm{s}$.

A proper validation is possible computing the wetted area A_{WET}, which is defined as the portion of plate covered by a layer of liquid with height higher than the precursor film one, and the interface area A_{INT}, which is the area of the liquid-gas free-surface in the wetted region. In figures 5.8(a) and 5.8(b) the resulting trends of A_{WET} and A_{INT} as a function of θ_e are compared with the numerical results of Singh et al. [12], obtained by means of a fully 3D model: the correspondence is satisfactory for all the investigated values of θ_e.
According to [17], the liquid pressure of a stable rivulet flowing over an inclined plate is independent of the plate downhill direction x, thus the rivulet profile can be calculated solving the following initial value problem,

$$p = \rho\, g\, h\, \cos\alpha - \sigma\, \frac{\partial^2 h}{\partial y^2} \left[1 + \left(\frac{\partial h}{\partial y}\right)^2\right]^{-3/2} = \text{const} \tag{5.13}$$

$$h|_{y_0} = 0,\ \left.\frac{\partial h}{\partial y}\right|_{y_0} = \tan\theta_e \tag{5.14}$$

which can be reduced to:

$$\frac{\partial h}{\partial y} = \sqrt{\left(-\cos\theta_e + \frac{1}{2}\frac{\rho\, g\, h^2}{\sigma}\cos\alpha - \frac{p\, h}{\sigma}\right)^{-2} - 1} \tag{5.15}$$

$$h|_{y_0} = 0 \tag{5.16}$$

The solution of Eq. (5.13) together with the initial conditions is iterated: the value of the rivulet pressure p is updated at each iteration, until the liquid flow rate, which can be calculated integrating the film flux per unit length

$$Q = \frac{\rho\, g\, h^3\, \sin\alpha}{3\,\mu} \tag{5.17}$$

across the rivulet length, equals the imposed one $\dot{V}_{in} = Q_{in}\, L_{in}$.
The resulting profile is then compared with the numerical one, obtained cutting the stationary liquid layer distribution at $x = L_x$. The validation for $\theta_e = 60°$ and $\theta_e = 50°$ are shown in figures 5.9(a) and 5.9(b) respectively, which show almost a perfect correspondence between numerical results and Eq. (5.13). The first step for understanding the hydrodynamics of absorption/distillation

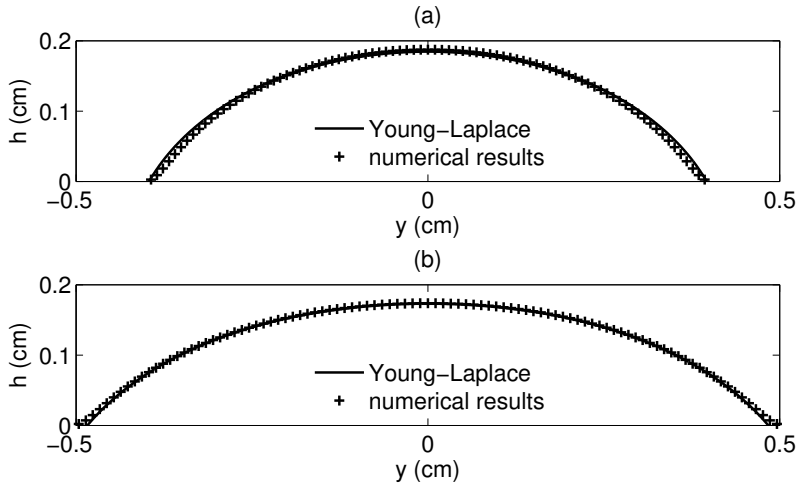

Figure 5.9: Comparison between rivulet profiles from solution of Eq. (5.13) and numerical simulation of rivulet build up: $\theta_e = 60°$ (a); $\theta_e = 50°$ (b). $\alpha = 60°$, $\dot{V}_{in} = 2\,\mathrm{cm}^3/\mathrm{s}$.

processes through structured packing is the analysis of the wetting dynamics of an inclined plate covered by a thin liquid layer. As explained in [12], the wetting phenomenon is dictated by several parameters, making crucial to focus on identifying proper non-dimensional numbers. The effect of solvent properties is analyzed through Kapitza number,

$$\mathrm{Ka} = \frac{{l_c}^2}{{l_v}^2} = \sigma \left(\frac{\rho}{\mu^4\, g}\right)^{1/3} \tag{5.18}$$

l_c and l_v being the capillary length and the viscosity length:

$$l_c = \left(\frac{\sigma}{\rho\, g}\right)^{1/2},\; l_v = \left(\frac{\mu^2}{\rho^2\, g}\right)^{1/3} \tag{5.19}$$

Kapitza number represents the relative importance of capillary and viscous forces in driving interface motion: for a low Kapitza number liquid, $\mathrm{Ka} \sim \mathcal{O}(1)$,

viscosity and surface tension play an equal role; a liquid has a high Kapitza number when Ka $\sim \mathcal{O}(10^2 - 10^3)$. High Kapitza number liquids can not be simulated adopting lubrication approximation, since surface tension forces are mainly balanced by liquid inertia rather than viscous forces.
The flow characteristics are studied in terms of Weber number,

$$\mathrm{We} = \frac{\rho\, {u_\infty}^2\, h_\infty}{\sigma} \tag{5.20}$$

which represents the ratio between liquid inertia and surface tension force. The effect of surface wettability is obviously given by the equilibrium contact angle θ_e. The wetted area A_{WET}, which is here normalized to the plate area A_{TOT}, is used for describing the wetting process, since it is the parameter to be optimized when designing the corrugated sheets composing the packed column.

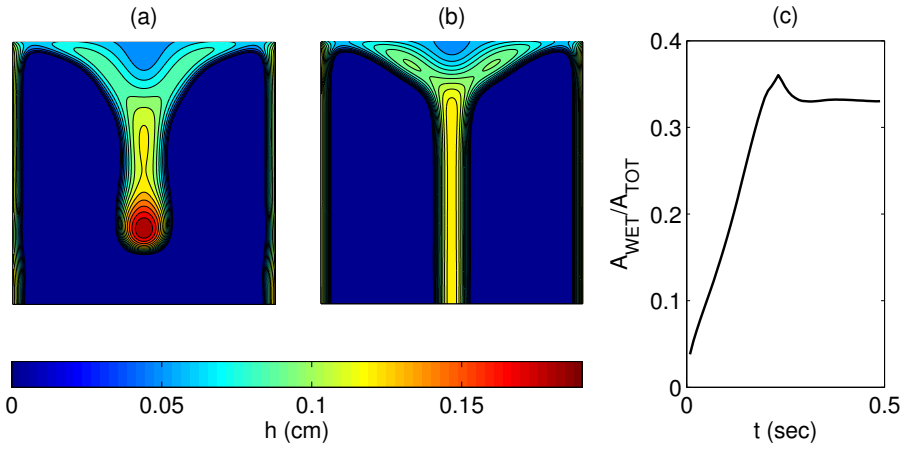

Figure 5.10: Liquid layer distribution over the inclined plate at $t = 0.19\,\mathrm{s}$ (a) and stationary distribution, $t = 0.49\,\mathrm{s}$ (b). Normalized wetted area as a function of time (c). $\theta_e = 60°$, Ka $= 49.7$, We $= 0.0736$.

Similarly to the approach of Singh et al. [12] and Hoffmann [33], an inclined plate is considered: the lateral boundaries are treated as walls, which implementation is explained in section 5.3; the whole top boundary of the plate represents the inlet section; the case of gravity driven flow is considered. The effects of θ_e, Ka and We on wetting dynamics are investigated, with equilibrium contact angle and Weber number up to 60° and 0.25 respectively. The Reynolds number is limited to Re ≤ 5.58, according to lubrication theory validity. The liquids listed in table 5.1 are simulated. The choice of these liquids is not casual, since they are used as solvent in CO_2 capture through packed column [12]. A $3 \times 3\,\mathrm{cm}^2$ plate, inclined at an angle $\alpha = 60°$ to the horizontal, is considered, but only half of the plate is simulated, thanks to the symmetry of the problem. The imposed precursor film thickness is equal to $\delta = 0.025\, h_\infty$. The spatial discretization step is not uniform over the computational domain, since a finer grid is required close to the wall for a better description of the liquid behavior, especially when low contact angles are imposed, leading to

higher slopes.
Figures 5.10(a) and 5.10(b), which refer to the same simulation, show the distribution of liquid $1-$methylepiperazine $0.51x$ MPZ over the plate at two different times. It can be noticed that the lateral walls capture some liquid due to capillary effect, perturbing the undisturbed flow. If the inlet flow rate is too low, this phenomenon leads to the growth of dry-patches on the plate, with the liquid forming two rivulets close to the walls and one rivulet in between. Similar results were obtained experimentally by Hoffman [33] and numerically by Singh et al. [12]. In figure 5.10(c) the plate wetted area is shown as a function of time. The wetting process can be clearly divided into two regimes: first the liquid bulk, driven by gravity, spreads in downhill direction; after the bulk reaches the outlet section, the contact line dynamics are mainly driven by the capillary force and thus influenced by the surface wettability.

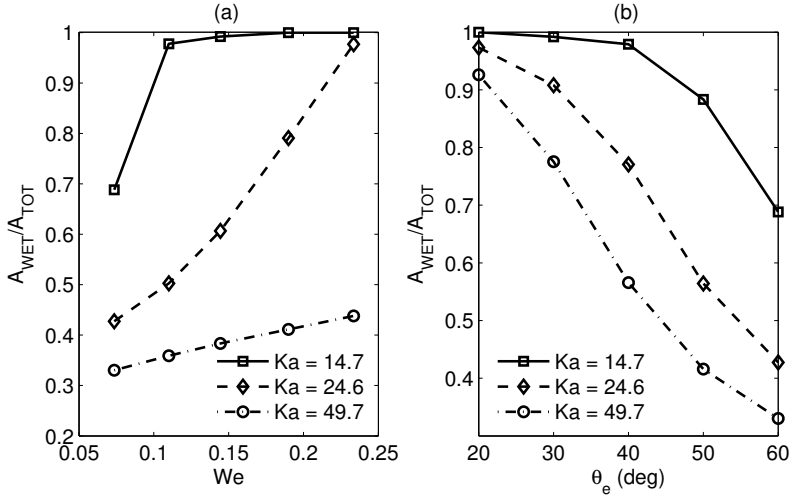

Figure 5.11: Normalized wetted area at the stationary liquid distribution as a function of Weber number, $\theta_e = 60°$ (a); as a function of equilibrium contact angle, We $= 0.0736$ (b). Fluids listed in table 5.1 are simulated, plate inclination is fixed to $\alpha = 60°$.

The dependence of the plate wetted area on Weber number, Kapitza number and equilibrium contact angle is shown in figures 5.11(a) and 5.11(b). Results refer to the stationary solution of Eqs. (5.4) and (5.5). In particular, figure 5.11(a) suggests that the effect of fluid inertia, i.e. of We, on wetting process grows with the Kapitza number, since the whole coverage of the plate, $A_{WET}/A_{TOT} = 1$, is reached for higher values of the Weber number. Thus, liquid spreading over the inclined plate is mainly driven by viscous, surface tension and gravity forces only for low Ka. Figure 5.11(a) also gives some information about the critical flow rate, defined as the minimum flow rate leading to whole coverage of the plate: the critical value of Weber number (which defines univocally the critical flow rate) can be traced as a function of the Kapitza number of the liquid. The definition of the critical flow rate is crucial, since it defines the most suitable condition (maximum wetted area) for absorption process through structured packing. The surface wettability

also has a great impact on wetting process, as shown in figure 5.11(b): higher values of the equilibrium contact angle lead to lower stationary wetted area, with low changes in contact angle leading to significantly differences in liquid behavior. Similar results were obtained from the rivulet build up simulations, figure 5.8(a).

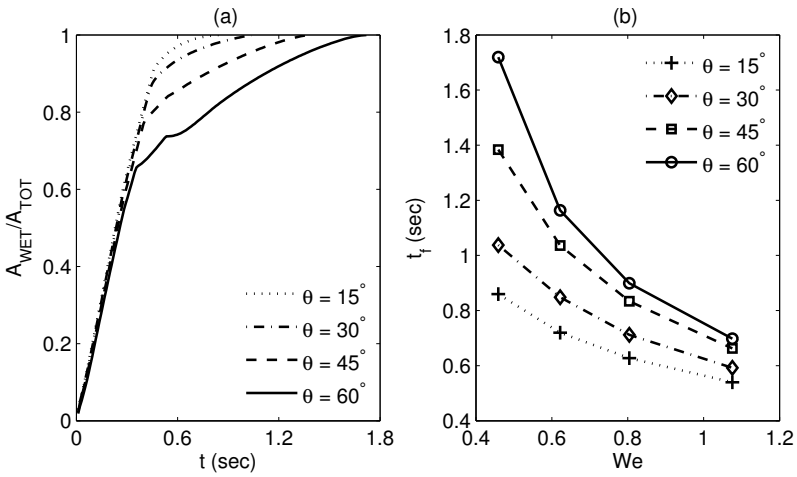

Figure 5.12: Wetted area as a function of time for different values of θ_e, We = 0.459, Ka = 14.7 (a). Time to reach $A_{WET} = L_x\, L_y$ as a function of We and θ_e, Ka = 14.7 (b). $6 \times 5\,\mathrm{cm}^2$ plate.

The influence of both Weber number and substrate wettability on the time t_f, needed to wet the whole domain, is investigated. In particular, the transient of the plate wetted area is plotted in figure 5.12(a) for different values of θ_e, keeping We and Ka fixed. Lowering the contact angle, the time required to wet the plate after the main rivulet, induced by the walls drawing effect, reaches the bottom of the plate decreases, meaning that the liquid front becomes more and more flat due to the higher substrate wettability. The time to reach full wetting condition is plotted in figure 5.12(b) as a function of We and θ_e. Higher Weber number corresponding to higher undisturbed film velocity u_∞, it is obvious that t_f increases lowering We. The effect of the surface wettability agrees with figure 5.12(a): $t_f \uparrow$ if $\theta_e \downarrow$.
Figure 5.13 is referred to the evolution in time of the liquid layer in case of We = 0.46 and $\theta_e = 60°$, the results in terms of plate wetted area versus time being also shown for the same test case in figure 5.12(a) (continuous line). In particular, it can be observed in figure 5.13 that two fingers fast drains down the plate, while only one finger was observed in the test case of figures 5.10(a) and 5.10(b); after the two fingers reach the bottom of the plate, the contact line motion moves slowly, mainly driven by capillary forces.
Finally, it is important to point out that the computational cost of the presented simulations is limited, thanks to the implemented ADI method, which allows to reach time step Δt up to 10^6 the explicit one. As an example, Singh et al. [12] conducted VOF simulations on a similar setup, running on 128 cores in parallel with 144 h required for a single simulation, while in the present work

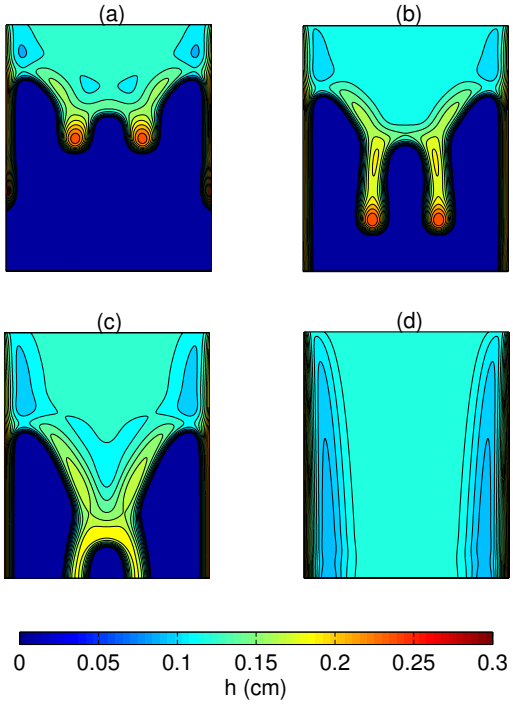

Figure 5.13: Liquid layer distribution over the inclined plate at different times: $t = 0.2\,\text{sec}$ (a); $t = 0.3\,\text{sec}$ (b); $t = 0.5\,\text{sec}$ (c); $t = 1.7\,\text{sec}$ (d). We $= 0.46$, Ka $= 14.7$, $\theta_e = 60°$, $6 \times 5\,\text{cm}^2$ plate.

simulation time is 4 times lower using a single core. The required simulation time is also summarized in table 5.2.

Literature work	Simulation time (h)	Number of cores
Singh. et al [12]	$24 - 144$	128
Current work	≤ 36	1

Table 5.2: Simulation time corresponding to the setup of figure 5.8.

5.5 Film over a corrugated layer of packing

Only the configuration given by an inclined plate bounded by lateral walls has been presented as a structured packing look-like configuration until now. In fact, it is the most investigated configuration in the available literature involving simulation of absorption/distillation process through structured packing [12, 33–35]. However, the evolution of a liquid film over a $132 \times 88\,\text{mm}^2$ corrugated sheet of packing was investigated through VOF method in [5], but parallelized simulations in supercomputers were needed in order to investigate only a few test cases. Thus, it was not possible to ensure sufficient information for a proper optimization of the packing geometry.
Thanks to the gain in computational costs that can be achieved using the cur-

rent 2D solver, it was possible to investigate the evolution of the thin film of liquid solvent over a packing layer. Eqs. (4.9), (4.24), (4.25) and (4.26), which were obtained for the general case of a film over a 3D curved substrate, are solved over the computational domain described by the packing layer.

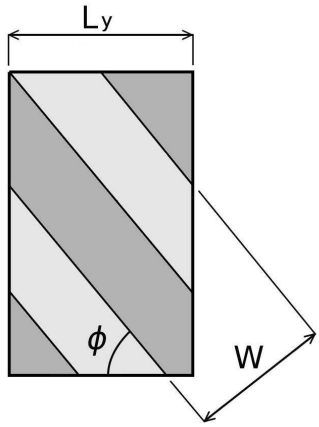

Figure 5.14: Portion of packing geometry (front view).

A further gain in terms of computational costs can be reached via the implementation of proper boundary conditions. In fact, imposing symmetry condition at the lateral boundaries $y = 0$, L_y (see figure 5.14) means that the liquid can not enter/exit the computational domain through $y = 0$, L_y. Thus, if you simulate just a portion of packing geometry in the core of the packed column, such a boundary condition leads to non-physical results close to the lateral boundaries (through which liquid must be free to flow), meaning that a larger portion of packing geometry must be simulated for gaining useful information in a narrow region of the domain. Moreover, it is reasonable to assume that the liquid behavior over the physical domain is periodic, since the packing geometry is periodic as well. Thus, periodic condition at the lateral boundaries $y = 0$, L_y must be implemented in the FVM solver,

$$\begin{cases} h_{i,1} = h_{i,n_j} \\ h_{i,2} = h_{i,n_j-1} \end{cases} \tag{5.21}$$

with $i \in [1,\, n_i]$, $j \in [1, n_j]$ denoting the i,j-th grid element (i corresponding to x reference direction, j corresponding to y reference direction).
A proper choice of the dimension L_y is sufficient to ensure that the imposed periodic boundary conditions through $y = 0$, L_y have a physical meaning,

$$L_y = k\,\frac{W}{\sin\phi} \tag{5.22}$$

with $k \in \mathbb{N}$ and W being the corrugation width, which defines the periodicity of the packing geometry according to figure 5.14. In fact, imposing L_y through Eq. (5.22), a periodic geometry of the solid substrate $z(x, y)$, which is

implemented on the computational domain, can be obtained as well, leading to:

$$\begin{cases} z_{i,1} = z_{i,n_j} \\ z_{i,2} = z_{i,n_j-1} \end{cases} \tag{5.23}$$

Adopting such an approach, the numerical investigation of the liquid behavior on a small portion of packing geometry gives information about the hydrodynamics over the whole packing layer.
On the other side, the implementation of periodic boundary conditions at $y = 0$, L_y makes impossible to reconduce to a pentadiagonal system when *splitting* along y with the current ADI approximate factorization, which allows to decompose the sparse algebraic system to be solved at each time step in two simpler systems. However, thanks to its structure, the linearized algebraic system $(n_i n_j) \times (n_i n_j)$ obtained from y-split can be divided in n_i blocks $n_j \times n_j$, which structure is almost pentadiagonal. Solving independently each block by means of a proper algorithm, the required computational cost does not increase considerably in comparison with the pentadiagonal case.
The investigated test cases are shown in table 5.3, as well as the simulated liquids, that are both involved in absorption/distillation processes, [5, 12]; the shear stress applied by the external gas flow is set to zero, thus $\boldsymbol{\tau_g} = \mathbf{0}$. The packing geometry is shown in figure 5.15. Test case T1 is chosen in order to replicate the computation of [5].

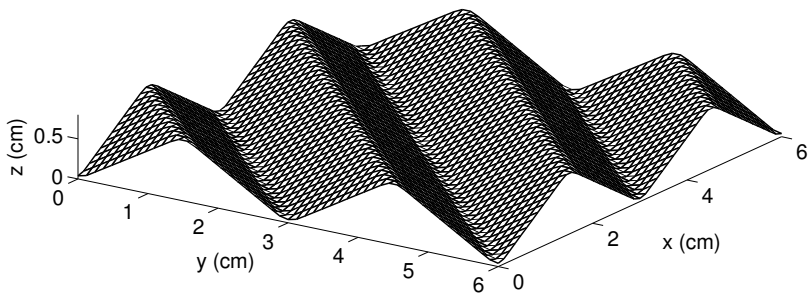

Figure 5.15: Simulated geometry of the packing layer: corrugation angle $\phi = 45°$; base width $W = 2.1\,\text{cm}$ and corrugation height $H = 0.7\,\text{cm}$, leading to $W/H = 3$ for test cases T1, T2 and T3. A joint radius equal to $r = 3\,\text{mm}$ is imposed in order to smoothen the sharp geometry of the packing layer.

Figure 5.16(a) shows the stationary liquid distribution over the corrugated sheet of packing deriving from simulation of test case T1. A confined inlet section is imposed, since it is not possible to replicate exactly the numerical setup of [5] (liquid injected from above) using the current 2D model. Comparing the liquid distribution and the substrate geometry, it can be noticed that the crimp angle ϕ, which defines the packing geometry according to figure 5.3, encourages the spreading of the confined rivulet entering the domain: in fact, the liquid clearly drains driven by gravity.

Test case	Liquid	$L_x \times L_y(\mathrm{cm}^2)$	$\alpha(\mathrm{deg})$	$\dot{V}_{in}(\mathrm{cm}^3/\mathrm{s})$	$L_{in}(\mathrm{cm})$
T1	silicon-oil	6×6	90	4	0.3
T2	$0.31\,x$MPZ	4.5×3	15	0.33	L_y
T3	$0.31\,x$MPZ	4.5×3	90	0.33	L_y

Liquid	$\rho\,(\mathrm{kg/m}^3)$	$\mu\,(\mathrm{Pa\,s})$	$\sigma\,(\mathrm{N/m})$	$\theta_e\,(\mathrm{deg})$
silicon-oil (DC5)	915.0	0.0046	0.0185	7
$0.31x$ MPZ	981.31	0.03642	0.0384	30

Table 5.3: Definition of the simulated test cases and liquids properties.

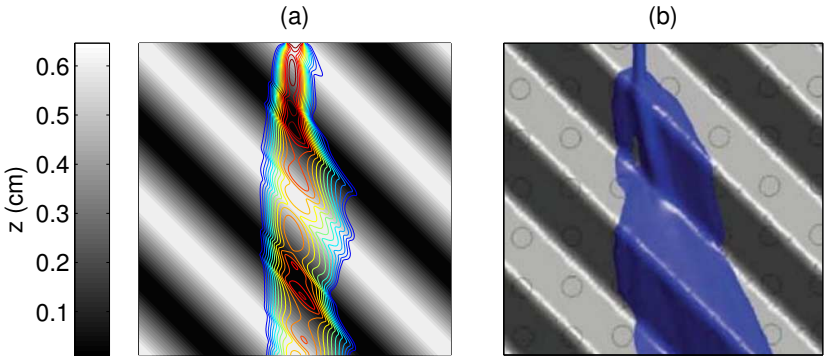

Figure 5.16: Predicted stationary film thickness distribution over the packing layer (a) vs snapshot of the solution from the fully 3D simulation of [5] (b). Test case T1.

A comparison between figure 5.16(a) and numerical result of [5], figure 5.16(b), reveals that there is not a perfect agreement, even if the tendency of the liquid to drain through the corrugations thanks to gravity is correctly catched. This is mainly due to:

- The liquid is here injected inside the physical domain in a different way from [5], leading to different boundary conditions.

- The inertia of the narrow rivulet at the inlet section is not negligible, leading to non-physical results near the injection point if lubrication theory is applied. In fact, the local Reynolds number of the entering liquid is:

$$\mathrm{Re} = \frac{\rho\,\dot{V}_{in}}{\mu\,L_{in}} = 248 >> 1 \tag{5.24}$$

- The simulated liquid is characterized by an high Kapitza number, Ka = 109.7, meaning that inertia rather than viscous dissipation is the main force opposing surface tension.

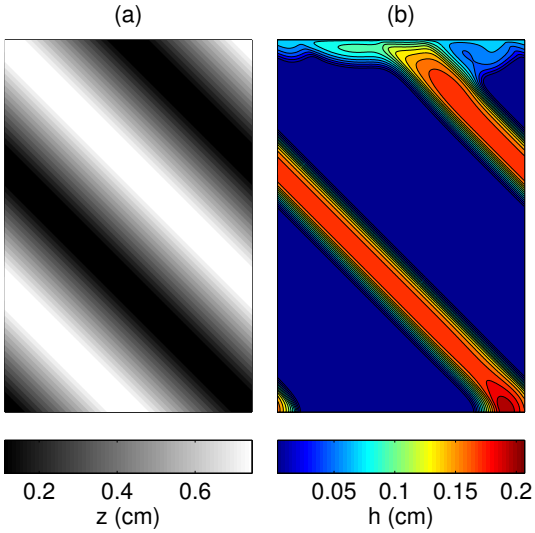

Figure 5.17: Periodic computational domain (a). Stationary liquid layer distribution (b). Test case T2.

Test case T2 is chosen with the aim of demonstrating the consistency of the imposed periodic boundary conditions. An uniform liquid flux per unit length is forced to enter the domain through $x = 0$, while the boundaries $y = 0$, L_y are treated with periodic boundary conditions. Figures 5.17(a) and 5.17(b) show the simulated domain and the stationary solution respectively. Looking at the stationary liquid distribution, figure 5.17(b), it can be observed that an array of rivulets flows through the lanes of the corrugated sheet of packing driven by gravity, as it can be expected. However, if symmetry boundary conditions were imposed, thus $\boldsymbol{Q} \cdot \hat{\boldsymbol{n}} = 0$ through $y = 0$ and $y = L_y$, it would be impossible to catch any rivulet entering or exiting through $y = 0$ or $y = L_y$, leading to non-physical results. Note that such a setup does not describe real problems involving absorption/distillation processes, since the corrugated sheets of packing are usually combined together in a vertical way (thus, $\alpha = 90°$, while $\alpha = 15°$ for test case T2). As above mentioned, the aim of this simulation was to prove that periodic boundary conditions are needed for a better analysis of the wetting phenomena over recurrent geometries.

The results of the simulation corresponding to test case T3 are presented in figures 5.18(b), 5.18(c) ans 5.18(d): the contour plots of the film thickness field over the computational domain can be compared with the corresponding packing layer geometry, figure 5.18(a), for a better understanding of the liquid behavior. The liquid is supposed to enter the domain, which is initially dry, through the inlet section $x = 0$ with an uniform flow rate per unit length Q_{in}, while periodic conditions are chosen for the lateral boundaries. The inlet section ($x = 0$) can be easily identified looking at figure 5.15. A longer portion of packing geometry is simulated along x direction (i.e. main flow direction), in order to reach fully developed flow before the liquid leaves the domain.
It can be noticed in figure 5.18(b) and 5.18(c) that two main rivulets form be-

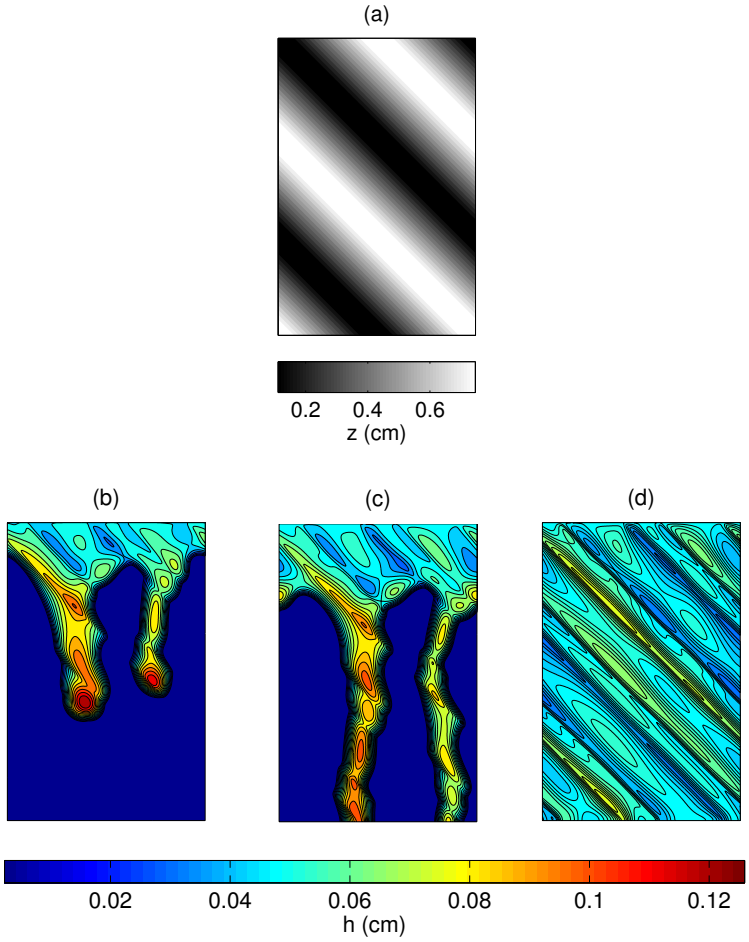

Figure 5.18: Geometry of the corrugated sheet of packing (a). Liquid layer distribution over the packing geometry at $t = 1\,\text{sec}$ (b). Liquid layer distribution at $t = 2\,\text{sec}$ (c). Stationary solution, $t = 7\,\text{sec}$ (d). Test case T2.

fore the packing geometry is fully wetted by the liquid film, figure 5.18(d). The liquid fingering is mainly caused by the corrugations, which induce instability. At the stationary condition, the computational domain is fully wetted, but a partial wetting may also occur depending on both imposed film flow rate Q_{in} and packing geometry. Both the corrugation height H and the corrugation angle ϕ are important, since they influence the way that the liquid flows over the corrugations, eventually ensuring a higher wetted area.
However, the main goal of the simulation T3 is that a real test case involving absorption/distillation process was successfully investigated. In fact the simulated liquid is used in CO_2 chemical absorption through structured packing [12] and the packing geometry is close to the configuration of [5]. The presented simulations were run on a single core, taking less than 36 h to reach stationary condition, despite a fine grid was chosen ($\Delta x \leq 0.2\,h_\infty$) ensuring good accuracy. Thus, a great reduction of computational costs is guaranteed by the 2D approach here used, without a considerable loss of information compared to a full 3D approach.

5.5.1 Parametric study

After verifying the capability of the model to describe the hydrodynamics of liquid films over the packing geometry, several simulations were run in order to investigate the influence of the flow characteristics, focusing on the effects of substrate wettability and Reynolds number. Two different packing geometries, that differ from each other in the corrugation angle ϕ, are investigated. The hydrodynamic behavior is described in terms of substrate wetted area A_{WET} and wetting speed, the wetted area being also the main parameter to be optimized when designing packing geometry.

Geometry	H (cm)	W (cm)	ϕ (deg)	α (deg)	$L_x \times L_y$ (cm^2)
G1	0.7	2.1	45	90	4.5×3
G2	0.7	2.1	30	90	4.5×4.2

Liquid	ρ (kg/m^3)	μ (Pa s)	σ (N/m)	Ka
0.31xMPZ	981.31	0.03642	0.0384	14.7

Table 5.4: Investigated packing geometries, G1 and G2, and simulated liquid, 1-methylepiperazione.

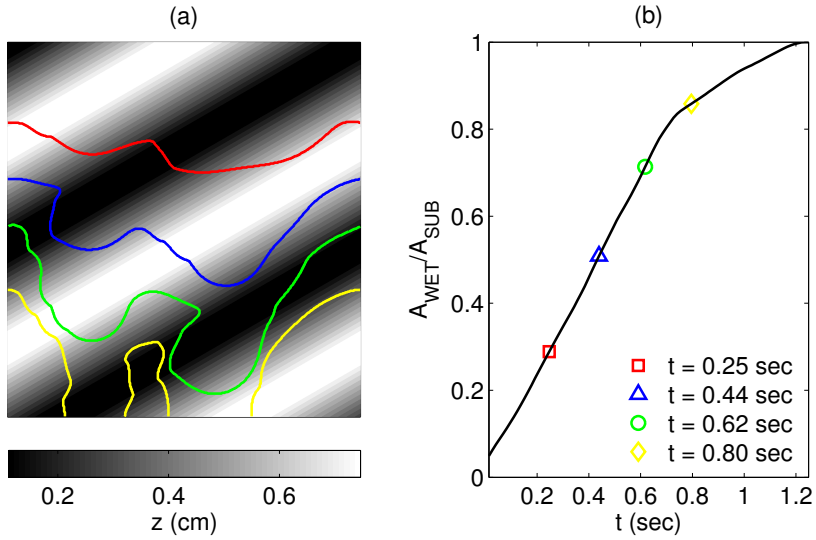

Figure 5.19: Contact line over the packing layer at $t = 0.25, 0.44, 0.62, 0.80$ (sec) (a). Normalized wetted area of the computational domain as a function of time, colored markers identifying the plotted contact lines (b). Re $= 1.35$, $\theta_e = 30°$, packing geometry G2.

Table 5.4 shows the investigated geometries G1 and G2 of the corrugated sheet of packing, the dimension L_y of the computational domain being imposed in order to ensure periodicity. The corrugated sheet main inclination α is fixed to 90°, according to [5]. Zero-shear applied by the external gas flow, $\boldsymbol{\tau_g} = \mathbf{0}$, is imposed. The simulated liquid, 1-methylepiperazione, is used as solvent in

CO_2 absorption through structured packing, [12].
The Reynolds number,

$$\mathrm{Re} = \frac{\rho\, Q_\infty}{\mu} \tag{5.25}$$

which is defined using the undisturbed film flow rate per unit length $Q_\infty = u_\infty\, h_\infty$, is here used for defining the flow characteristics instead of Weber number, as previously done according to [12]. Reynolds number being directly related to the imposed film flux, it better represents the operative conditions, which the packing geometry is designed for, and thus is a relevant parameter. The undisturbed film flow rate Q_∞ is forced to enter the domain through the top section of the packing layer, while periodic conditions are imposed at the lateral boundaries $y = 0,\, L_y$. The computational domain is initially dry. The spatial discretization step, which varies on the computational domain, is always kept lower than a certain value over the corresponding structured grid, in particular $\Delta x < 0.2\, h_\infty$ is imposed at each simulation. Such an accuracy together with the imposition of precursor film thickness $\delta = 0.05\, h_\infty$ and disjoining pressure exponents $(n, m) = (3, 2)$ guarantees grid independence for all the investigated configurations.
Figure 5.19(a), which is referred to pecking geometry G2, shows the evolution in time of the contact line over the corrugated packing layer. Even if a moderate value of the equilibrium contact angle is simulated, two rivulets appear due to finger instability, both driven by gravity, the liquid bulk alternatively accumulating and spreading over the corrugated geometry; the corrugation angle ϕ seems to play a crucial role in growth and evolution of such rivulets. The corresponding evolution in time of the substrate wetted area A_{WET} is plotted in figure 5.19(b), revealing that two different regimes can be identified: the wetted area first increases with a constant wetting rate; once the two rivulets reach the outlet section of the domain, the wetting speed rapidly decreases and the contact line motion is mainly driven by capillary forces, until the domain is fully wetted. The same behavior was observed in the previous section, where the liquid spreading over an inclined plate bounded by two lateral walls was simulated, see figure 5.10(c).
Obviously, higher contact angles would lead to a slower wetting process or eventually to a partial wetting of the packing layer. This can be understood looking at figures 5.20(a) and 5.20(b), referred to geometries G1 and G2 respectively, which plot the time t_f to reach the stationary condition as a function of the substrate wettability and the Reynolds number of the undisturbed film, the latter being univocally defined by the imposed liquid flow entering through the inlet section. As expected, the time needed to wet the computational domain increases for both decreasing surface wettability, $\theta_e \uparrow$, and film flow rate, $\mathrm{Re} \downarrow$. An exception, with a local maximum of t_f appearing, can be observed for both test cases G1 and G2 when the imposed equilibrium contact angle equals $\theta_e = 45°$. Defining Re_{CR} as the corresponding Reynolds number, it can be observed that: time t_f decreases for increasing Re if $\mathrm{Re} > \mathrm{Re}_{CR}$; time t_f decreases for decreasing Re if $\mathrm{Re} < \mathrm{Re}_{CR}$. The occurrence of the partial wetting condition for low Reynolds number (i.e. the domain is not fully wetted

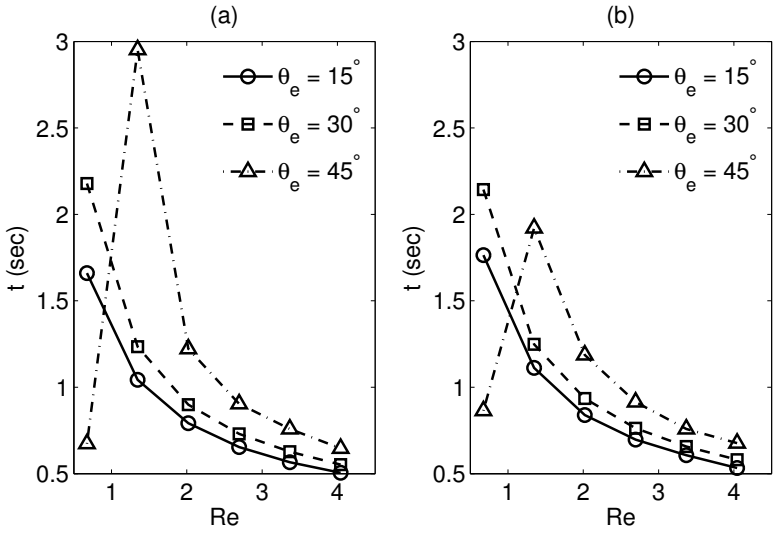

Figure 5.20: Time to reach stationary liquid layer distribution as a function of Reynolds number and substrate wettability: investigated geometry G1 (a); investigated geometry G2 (b).

by the stationary film distribution when $\mathrm{Re} < \mathrm{Re}_{CR}$), justifies such a decrease of the time needed to reach the stationary condition, as a comparison between figures 5.20(a), 5.20(b) and figure 5.21 clearly demonstrates.
On the other side, the influence of packing geometry on wetting dynamics can be also understood comparing the numerical results deriving from the investigated geometries G1 and G2. Figures 5.20(a) and 5.20(b) show almost the same qualitative and quantitative behavior for both G1 and G2, in terms of computed time to reach stationary condition.

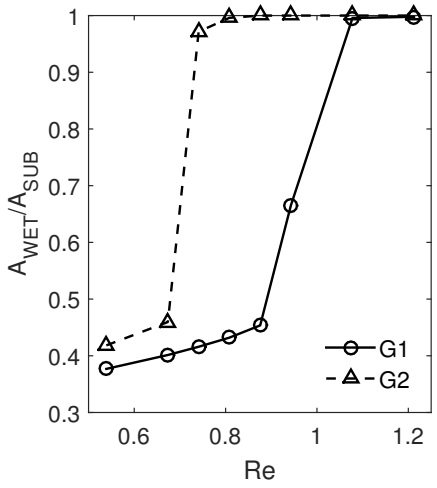

Figure 5.21: Stationary normalized wetted area of the simulated packing layer versus imposed Reynolds number. Geometries G1 and G2 investigated, $\theta_e = 45°$.

However, a more interesting comparison between G1 and G2 can be done

focusing on their influence on the stationary wetted area of the domain, which is plotted in figure 5.21 as a function of Re for a fixed substrate wettability for both the geometries. Referring to the normalized wetted area,

$$\tilde{A}_{WET} = \frac{A_{WET}}{A_{SUB}} \tag{5.26}$$

A_{SUB} being the total substrate area, allows to focus on the effect of packing geometry, independently from the dimensions of the computational domain. The critical Reynolds number defining the inception of partial wetting condition corresponds to the maximum of t_f (which is the time needed by the liquid to reach the stationary distribution), previously observed in both figures 5.20(a) and 5.20(b). It can be observed that: geometry G2, defined by a lower corrugation angle, $\phi = 30°$ instead of $\phi = 45°$, always leads to higher normalized wetted area for a fixed value of the imposed Re, thus a proper wetting of the packing layer is encouraged, apparently making G2 a more suitable configuration; the wetted area varies very sharply when Re approaches Re_{CR} for both G1 and G2.
However, in real structured packing, the packing layers are put together in touch, adding a new effect (flow perturbed by a solid obstacle with eventual mass exchange between two different layers or unexpected liquid accumulation), that is not taken into account in this work but can be properly modeled even with the current 2D approach. In chapter 3.4, for example, a non-wettable patch simulating an obstacle was introduced in order to perturb the undisturbed film flow: implementing a certain number of small non-wettable patches, where two layers are put in contact, may be a first step to simulate a real configuration.

Chapter 6

Conclusion

An implicit FVM solver was developed in `FORTRAN` in order to predict the evolution of a thin liquid layer, driven by gravity and shear of an external gas flow over a solid substrate, assuming lubrication theory. The small slope approximation was abandoned in favor of a new, more accurate formula, derived from Young-Laplace equation, for computing interface curvature when low surface wettabilities are involved. The new approximate model, which was first compared with the exact formula of [21] defining the mean curvature of a 3D surface, still allows to apply the ADI factorization of [13], resulting in a considerable reduction of computational costs. Thus, the full implementation of capillary pressure allowed to investigate higher equilibrium contact angles (traducing in lower substrate wettability), compared to the available literature involving numerical simulation of thin films under lubrication approximation. In fact, values up to 60° were investigated, leading to an increase of 3 times the commonly simulated contact angles. Even higher contact angles can be investigated, but it was observed that the growing numerical instability leads to an increase of the computational costs, the threshold 60° being identified as a great compromise. This obviously allows to simulate a wider range of physical configurations. For example, the analysis of CO_2 absorption process through structured packing may involve liquid solvent flowing over non-wettable surfaces, leading to equilibrium contact angle up to 70° [12]. Investigating such a setup would not be possible applying the small slope approximation within the lubrication theory. However, the mathematical limit of lubrication theory being $\theta_e \leq 90°$, liquid layer evolving on hydrophobic surfaces (i.e. $\theta_e > 90°$), which are involved in a number of engineering problems, can not be simulated. Even if water on steel and glass is still characterized by low equilibrium contact angles (with θ_e ranging in $70° - 80°$ for water-steel, as stated in [33]), many polymers with water flowing on their surface are characterized by a hydrophobic behavior and some materials with highly rough surfaces may exhibit water equilibrium contact angle up to 150° or even higher, leading to the definition of superhydrophobic surfaces.
The general case of a film flowing over a 3D curved substrate was also investigated successfully still applying lubrication theory, the definition of local coordinates on the substrate allowing to maintain the 2D mathematical approach.

Such a generalization represents the main goal, since real configurations often involve liquid spreading over bumped surfaces and thus they can not be studied simply considering a film flowing over an inclined plate.
The developed solver is first validated, forcing a fixed amount of liquid to enter into a cave and verifying that: the inlet volume is equal to the final volume inside the cave; the free-surface profile respect the well known Young-Laplace equation. Thus, a film flowing over and around multiple obstacles was investigated, focusing on the influence of obstacle dimension and surface wettability on wetting dynamics. Interesting evidences were obtained. In particular, it was found that the surface wettability has a great impact on the contact line dynamics and the way the liquid film distributes over the obstacles.
A further validation was reached testing the capability of the implemented capillary pressure model together with the disjoining pressure to correctly describe the wetting dynamics when equilibrium contact angles up to 60° are involved. Finally, the CO_2 absorption processes through structured packing was studied, focusing on the hydrodynamics in the packing geometry. First, a test case involving rivulet build-up (the simulated liquid being used as a solvent for CO_2 absorption) was investigated and compared with literature numerical evidences resulting from 3D VOF simulations. Then, the effect of solvent properties (Ka), flow characteristics (We) and substrate wettability (θ_e) on wetting dynamics were investigated in terms of plate wetted area, which is the parameter to optimize when designing the packing geometry. A simple configuration (inclined plate bounded by lateral walls) describing the packing was considered and several simulations were run varying Ka, We and θ_e, gaining some useful information. Then, a more complex geometry was considered and liquid rivulets flowing over a corrugated sheet of packing was successfully simulated, in order to demonstrate the flexibility of the implemented solver and its capability to properly solve a real test case occurring in absorption through packed column. Thanks to the packing geometry, periodic conditions through the lateral boundaries of the domain were implemented, allowing to understand the behavior of a flowing film over the whole corrugated sheet of packing just simulating a small element of packing, namely $4.5 \times 3\,\mathrm{cm}^2$.
Replicating the VOF simulations of [5, 12], similar results were obtained, finding that the 2D approach is still able to model wetting phenomena and contact line evolution without any loss of information. Moreover, a consistent improvement in terms of computational costs was observed, as clearly demonstrated by table 5.2.
A full analysis of the influence of changing the packing geometry on the wetted area allowing for CO_2 absorption process optimization is still pending, since only few configurations differing in corrugation angle were investigated and the effect of joining two neighbour packing layers should be also modeled. Moreover, the effect of shear stress applied by the exhaust CO_2 gas flow must be investigated. Since the solver already takes into account for the eventual shear stress applied at the free-surface, the coupling with a CFD of the core flow is possible: the shear to be imposed when solving the film distribution is given by the gas flow field, while the film velocity at the liquid-gas interface represents

the slip condition of the CFD problem.
It was not possible to simulate solvents having high Kapitza numbers, as done in [5, 12, 33, 34], since the full wetting condition for such liquids is reached for high values of the Reynolds number, which are not allowed by the lubrication approximation. This is due to the lower viscosity of the high Ka solvents, which induce liquid inertia to be the main action opposing the capillary force. However, lubrication theory can be still applied when inertial forces are not negligible, as explained in chapter 2.6. Thus, mass and momentum equations can be still integrated across the film thickness, retaining the liquid inertia and assuming the velocity profile. This means that the 2D approach is still valid, but three different equations must be solved in the unknowns film thickness h and film average velocity $\boldsymbol{u}$.
Finally, it is important to point out that the developed solver is suitable for other engineering applications: the implementation of a source term allows to simulate condensation in dehumidifier fin surface and can be even used for modeling the drop impinging in in-flight icing phenomena; the behavior of liquid films over hydrophilic curved surfaces is also becoming an interesting application that the current model can be applied to.

Bibliography

[1] B. Ponter, G. A. Davies, T. K. Ross, and P. G. Thornley. The influence of mass transfer on liquid film breakdown. *International Journal of Heat and Mass Transfer*, 10:349, 1967.

[2] T. Podgorski, J. M. Flesselles, and L. Limat. Dry arches within flowing films. *Physics of Fluids*, 11:845, 1999.

[3] M. Sellier. Modelling the wetting of a solid occlusion by a liquid film. *International Journal of Multiphase Flow*, 71:66, 2015.

[4] B. R. Duffy and H. K. Moffatt. A similarity solution for viscous source flow on a vertical plane. *European Journal of Applied Mathematics*, 8:37, 1997.

[5] K. Subramanian and G Wozny. Analysis of hydrodinamics of fluid flow on corrugated sheets of packing. *International Journal of Chemical Engineering*, 2012:13, 2012.

[6] G. Croce, E. De Candido, and P. D'Agaro. Numerical modelling of heat and mass transfer in finned dehumidifier. *Applied Thermal Engineering*, 29:1366, 2009.

[7] G. Croce, E. De Candido, W. G. Habashi, J. Munzar, M. Aube, G. S. Baruzzi, and C. Aliaga. Fensap-ice: Analytical model for spatial and temporal evolution of in-flight roughness. *Journal of Aircraft*, 47:1283, 2010.

[8] D. E. Hartley and W. Murgatroyd. Criteria for break-up of thin liquid layers flowing isothermally over solid surfaces. *International Journal of Heat and Mass Transfer*, 7:1003, 1964.

[9] S. D. R. Wilson. The stability of a dry patch on a wetted wall. *International Journal of Heat and Mass Transfer*, 17:1607, 1974.

[10] F. P. Bretherton. The motion of long bubbles in tube. *Journal of Fluid Mechanics*, 10:166, 1961.

[11] L. W. Schwartz and R. R. Eley. Simulation of droplet motion on low-energy and heterogeneous surfaces. *Journal of Colloid and Interface Science*, 202:173, 1998.

[12] R. K. Singh, J. E. Galvin, and X Sun. Three-dimensional simulation of rivulet and film flows over an inclined plate: effect of solvent properties and contact angle. *Chemical Engineering Science*, 142:244, 2016.

[13] T. P. Witelski and M. Bowen. Adi schemes for higher-order nonlinear diffusion equations. *Applied Numerical Mahtematics*, 45:331, 2003.

[14] J. A. Diez and L. Kondic. Computing three-dimensional thin film flows including contact lines. *Journal of Computational Physics*, 183:274, 2002.

[15] Y. Zhao and J. S. Marshall. Dynamics of driven liquid films on heterogeneous surfaces. *Journal of Fluid Mechanics*, 559:355, 2006.

[16] W. Nusselt. Die verbrennung und die vergasung der kohle auf dem rost. *International Journal of Heat and Mass Transfer*, 3:359, 1961.

[17] M. S. El-Genk and H. H. Saber. Minimum thickness of a flowing down liquid film on a vertical surface. *International Journal of Heat and Mass Transfer*, 44:2809, 2001.

[18] S. K. Wilson and B. R. Duffy. Unidirectional flow of a thin rivulet on a vertical substrate subject to a prescribed uniform shear stress at its free surface. *Physycs of Fluids*, 17:108105, 2005.

[19] E. Rio and L. Limat. Wetting hysteresis of a dry patch left inside a flowing film. *Physics of Fluids*, 18:032102, 2006.

[20] S. Manservisi and R. Scardovelli. *Termoidraulica dei flussi bifase*. Societá Editrice Esculapio, 2012.

[21] M. P. Do Carmo. *Differential Geometry of Curves and Surfaces*. Prentice-Hall, Inc., 1976.

[22] M. R. Mata and A. L. Bertozzi. A numerical scheme for particle-laden thin film flow in two dimensions. *Journal of Computational Physics*, 230:6334, 2011.

[23] T. D. Blake. The physics of moving wetting lines. *Journal of Colloid and Interface Science*, 299:1, 2006.

[24] J. B. Dupont and D. Legendre. Numerical simulation of static and sliding drop with contact angle hysteresis. *Journal of Computational Physics*, 229:2453, 2010.

[25] J. A. Diez, L. Kondic, and A. Bertozzi. Global models for moving contact lines. *Physical Review*, 63:011208, 2000.

[26] S. K. Wilson, B. R. Duffy, and S. H. Davis. On a slender dry patch in a liquid film draining under gravity down an inclined plane. *European Journal of Applied Mathematics*, 12:233, 2001.

[27] D. E. Weidner, L. W. Schwartz, and M. H. Eres. Role of surface tension gradients in correcting coating defects in corners. *Journal of Colloid and Interface Science*, 187:243, 1997.

[28] A. Oron, S. H. Davis, and S. G. Bankoff. Long-scale evolution of thin liquid films. *Reviews of Modern Physics*, 69:931, 1997.

[29] E. D. Hay, S. Hibberd, and H. Power. Inertial effects at moderate reynolds number in thin-film rimming flows driven by surface shear. *Physics of Fluids*, 25:102108, 2013.

[30] M. Magnini, A. Ferrari, and J. R. Thome. Undulations on the surface of elongated bubbles in confined gas-liquid flows. *Physical Review Fluids*, 2:084001, 2017.

[31] L. M. Pismen. Nonlocal diffuse interface theory of thin films and the moving contact line. *Physical Review E*, 64:021603, 2001.

[32] W. G. Whitman. The two-film theory of gas absorption. *International Journal of Heat and Mass Transfer*, 5:429, 1962.

[33] A. Hoffmann, I. Ausner, J. U. Repke, and G.Wozny. Fluid dynamics in multiphase distillation processes in packed towers. *Computers and Chemical Engineering*, 29:1433, 2005.

[34] J. U. Repke, I. Ausner, S. Paschke, A. Hoffmann, and G. Wozny. On the track to understanding three phases in one tower. *Chemical Engineering Research and Design*, 85:50, 2007.

[35] Y. Y. Xu, M. Zhao, S. Paschke, and G. Wozny. Detailed investigations of the countercurrent multiphase (gas-liquid and gas-liquid-liquid) flow behavior by three-dimensional computational fluid dynamics simulations. *Industrial and Engineering Chemistry Research*, 53:7797, 2014.

domani è sempre un poco ieri
non passan treni qua vicino
ma che vuoi
è una piccola città mi dico sempre
e domani me ne vado via

l'arte si fa più lontana
questi locali fanno schifo
e in questa noia che mi stordisce
io dimentico

passerà anche questo tempo
così avaro e così stanco
per ora non so dove altro andare...

Vinicio